METAL-ASSISTED CHEMICAL ETCHING OF SEMICONDUCTOR NANOSTRUCTURES FOR ELECTRONIC APPLICATIONS

BY

JEONG DONG KIM

DISSERTATION

Submitted in partial fulfillment of the requirements
for the degree of Doctor of Philosophy in Electrical and Computer Engineering
in the Graduate College of the
University of Illinois at Urbana-Champaign, 2017

Urbana, Illinois

Doctoral Committee:

Professor Xiuling Li, Chair
Professor James J. Coleman
Professor J. Gary Eden
Professor Joseph W. Lyding
Assistant Professor SungWoo Nam

ABSTRACT

Metal-assisted Chemical Etching (MacEtch) is a robust and versatile top-down etching process which has the capability of overcoming the limits of conventional wet and dry etching. The advantage of producing anisotropic high aspect ratio micro- and nanostructures with the absence of ion induced surface damage has attracted tremendous attention in device applications such as light emitting diodes, solar cells, biosensors, supercapacitors, thermo-electrics, and 2.5 D and 3D transistors.

The detailed research on MacEtch has been accomplished by many researchers since its discovery by Li and Bohn in 2000. This includes MacEtch using different types of substrates (Si, GaAs, InP, GaP, GaN), metal catalysts (Au, Ag, Pt), substrate doping concentration, porosity and so on. Although there has been huge progress over the years, there are still obstacles which limit the application of MacEtch in commercial industries. First, there is still no experimental demonstration in the literature describing the simultaneous influence of carrier generation and mass transport in MacEtch. Second, noble metals used as the catalysts in MacEtch are not compatible with complementary metal-oxide-semiconductor (CMOS) technology due to the deep-level traps.

In this dissertation, sub-micron scale highly ordered crystalline silicon (c-Si) via array is demonstrated by MacEtch. The systematic study of etch rate as functions of catalyst diameter, pitch, and spacing experimentally demonstrates the simultaneous influence of carrier generation and mass transport in MacEtch. Next, sub-micron scale polycrystalline silicon (Poly-Si) via using a novel method called self-anchored catalyst (SAC) MacEtch is presented. The catalysts delamination and detour resulted by the inconsistent etching originated from polycrystalline grains and grain boundaries are minimized by physically anchoring the catalyst with the nanowires

formed through the porous catalyst array. This SAC-MacEtch is also demonstrated in the large scale though c-Si via array and GaAs via array. Next, the first demonstration of CMOS-compatible titanium nitride (TiN) assisted chemical etching is presented. The conventional liquid phase and the vapor phase MacEtch are demonstrated to characterize the inverse MacEtch, and the modified vapor phase MacEtch is introduced to make the transition from inverse to forward MacEtch by enhancing the mass transport of etchant and byproducts. The length of the nanowire array produced by the mesh patterned TiN is characterized as the function of mesh dimension, etching temperature, and TiN thickness to analyze the etching characteristics. Next, GaP MacEtch with the Au catalyst using HF and H_2O_2 is presented. Inverse and forward Macetch are controlled by enhancing or limiting the MT.

To my parents Sang Tae Kim and Kyung Ae Park

ACKNOWLEDGMENTS

First of all, I would like to express my sincere gratitude to my advisor Professor Xiuling Li for giving me an opportunity to work with her. She always inspired me with passion and dedication for research. I was able to knock on her office door anytime to ask for advice when I had a new idea or result. She trusted and believed in my potential and supported me with kindness and patience.

I would like to thank my former advisor Professor James Coleman for his support and guidance. I was very fortunate to learn not only the scientific thinking process but also innumerous life lessons from him.

I would like to thank Professor Oliver Chen for helping me during my PhD. He always helped me when I experienced difficult times. I will never forget his support and friendship.

I would like to thank Professor J. Gary Eden, Professor Joseph W. Lyding and Professor SungWoo Nam for serving on my doctoral committee and contributing invaluable advice on my thesis research.

I would like to thank former and current group members: Chen Zhang, Karthik Balasundaram, Kelson Chabak, Kevin Bassett, Kyooho Jung, Moyang Li, Munho Kim, Ryan Dowdy, Parsian Mohseni, Paul Froeter, Seung Hyun Kim, Wen Huang, Wonsik Choi, Xiang Zhao, Xin Miao and Yi Song for the collaboration and their friendship.

I would like to thank the former and current MNTL staffs: Aaron Wilken, Clay Childers, Edmond Chow, Ken Tarman, Mike Hansen, Richard Malloch, Yaguang Lian for their hard work and dedication to maintain the MNTL cleanroom.

I would like to thank the financial support from the National Science Foundation (NSF), the International Institute for Carbon Neutral Energy Research (WPI-I2CNER), SanDisk and Silfex.

I would like to thank my uncle, aunt and cousins, Joon and Esther for their love and support. They always welcomed me and treated me like their son and brother. I was able to defeat my homesickness because of their love and support.

I would like to thank my brother Ho Dong Kim for his support. He is my big brother who always took care of the foolish and naïve side of me.

I would like to thank Min Ju Kang for her love and support. She was always there for me whenever I had difficult times.

Finally, I would like to thank my parents Sang Tae Kim and Kyung Ae Park for their support and caring. They have always respected my life changing decisions and supported me with their unconditional love. I am very blessed and thankful to have them as my parents.

TABLE OF CONTENTS

1. INTRODUCTION

In this chapter, the fundamental of Metal-assisted Chemical Etching (MacEtch) is discussed. The overview process of MacEtch, basic mechanisms of anodic and cathodic reactions, and carrier generation and mass transport theories are presented. Also, the state-of-the-art of sub-micron scale via array by MacEtch and complementary metal-oxide-semiconductor (CMOS) compatible MacEtch are discussed.

1.1 Metal-Assisted Chemical Etching Overview

MacEtch is a local electrochemical etching technique that can be used to produce the anisotropic high aspect ratio features using wet chemical etching solution. The typical silicon (Si) MacEtch process starts by depositng catalyst composed of noble metals (Au, Ag, Pt, etc.) on the substrate[1, 2]. The catalyst can be deposited or patterned into any arbitrary geometry such as mesh, dots, or trenches with a micro- or nano-scale dimension [3, 4]. Then, the substrate is immersed in the chemical solution of hydrofludic acid (HF) and hydrogen peroxide (H_2O_2) to selectively oxidize and etch the Si localized under the defined catalysts.

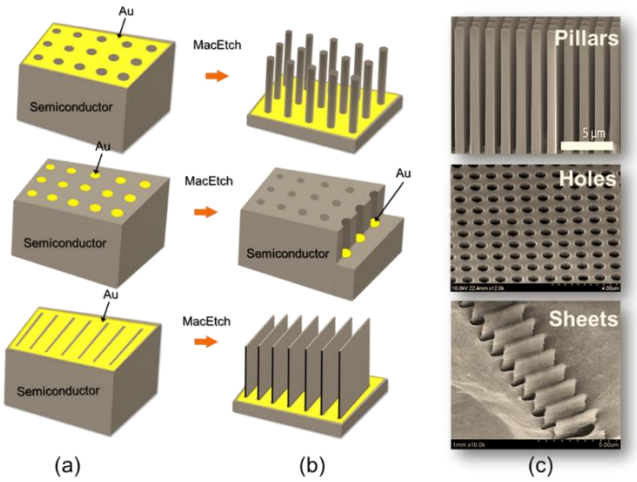

Figure 1.1: Schematics of the patterned mesh, dots, and trenches of Au catalysts (a) before MacEtch, (b) after MacEtch, and (c) SEM images of the etched patterns [1].

Figure 1.1 (a) shows the schematics of the mesh, discret dot array, and line patterned Au film deposited on the Si substrates. Figure 1.1 (b) shows the schematics of the high aspect ratio features produced by MacEtch. Figure 1.1 (c) shows the SEM images of the pillar, via, sheet arrays corresponding to the Figure 1.1 (b).

1.2 Cathode and Anode Reactions

MacEtch involves a pair of redox reactions: a cathodic and an anodic reaction [1, 2]. The cathodic reaction is defined as the reduction of the oxidant at the liquid/metal interface in presence of protonated hydrogen from the acidic solution. For the Si MacEtch using the mixture of HF and H_2O_2, this process be described as shown in equation (1.1).

$$H_2O_2 + 2H^+ \rightarrow 2H_2O + 2h^+ \quad (1.1)$$

The hydrogen (H_2) gas is produced during the cathode reaction and this can be described as shown in equation (1.2).

$$2H^+ \rightarrow H_2 + 2h^+ \quad (1.2)$$

The anodic reaction is defined as the hole injection and the Si removal. There are three different hypothesized anodic reactions that are direct dissolution of Si in the tetravelent state [1, 2, 5-7], direct dissolution of Si in the divalent state [2, 8], and formation and dissolution of the Si oxide [2, 9, 10]. It is generally accepted that the anodic reaction is the combinations of direct dissolution of Si in tetravelent and divalent states and this is described as

$$Si+6HF+4h^+ \rightarrow H2SiF6 +4H^+ \quad (1.3)$$

As the result, the overall redox reaction is described as

$$Si + H_2O_2 + 6HF \rightarrow 2H_2O + H_2SiF_6 + H_2 \quad (1.4)$$

1.3 Carrier Generation and Mass Transport Models

There are two hypothesized MacEtch mechanism models, carrier generation (CG) and mass transport (MT) that analytically describes the etch rate and etch profile [1, 11, 12]. The CG is defined as the generation, injection, and diffusion of the holes and the MT is defined as the transport of regents (HF, H_2O_2) and byproducts of Si dissolution (H_2, H_2O, H_2SiF_6).

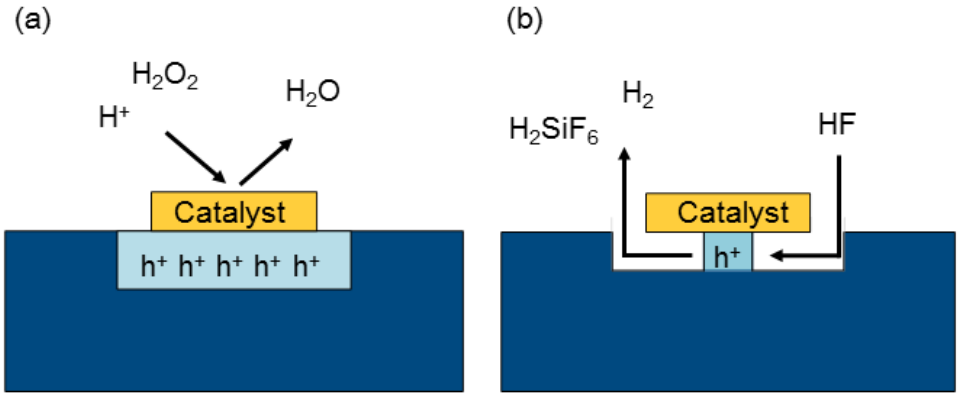

Figure 1.2: Cross-section schematics of the (a) carrier generation, (b) mass transport process in MacEtch.

Figure 1.2 (a) and (b) show the cross-section schematics of the CG and the MT mechanisms respectively. According to the CG model, the etch rate and the etch profile are governed by the hole injection rate and the diffusion of the holes in the Si under the catalyst. Chattopadhyay et al. suggested the hole injection mechanism of the Pt catalyst in an HF and H_2O_2 solution by comapring the energy levels of Si and the electrochemical potential of H_2O_2/H_2O, and qualitatatively described that the holes are injected deep into the valence band through the catalyst [13]. Peng et al. suggested the MacEtch mechanism of the Ag catalyst in HF by comparing the electrochemical potentials of $AuCl_4^-/Au$, $PtCl_6^{2-}/Pt$, Ag^+/Ag, Cu^{2+}/Cu, Fe^{3+}/Fe^{2+} and energy levels of the Si, and described that for Ag catalyst in HF, the hole injection occurred by reduction reaction in Ag nuclei [14].

The carrier generation is also influenced by the surface band bending of the Si at catalyst/substrate interface, and this results in different MacEtch behavior in various doping types of the Si substrates. Huang et al. suggested the localized galvanic etching in MacEtch using the calculation of Schottky barrier height and potential of valence band maximum [15]. Lai et al. experimentally and theoretically demonstrated the etching behavior in different doping concentration of p-type and n-type Si substrates [16]. They suggested in n-type silicon, the injected holes are trapped at the catalyst/silicon interface resulting the vertical sidewall while in p-type Si, injected holes are drifted away from the interface resulting in the tapered sidewall. Lianto et al. demonstrated the controlling of etching stability based on the excess hole concentration model by patterning arrays of micron stripes with varied catalyst dimensions and spacings, and etching at varied H_2O_2 concentrations [11]. They observed that the hole concentration under a stripe overlaps with the one under the neighboring stripes that produces the curved trenches by enhancing the etch rate at catalyst edges.

According to the MT model, the etch rate and etch profile are influenced by the transport of the regent (HF) and the byproducts of the dissolution (H_2SiF_6, H_2). This model assumes that the effective length which regent and byproducts diffuse decreases as the lateral dimension of the catalyst decreases, thus, the etch rate increases with decreasing catalyst dimension. On the other hand, for the large catalyst, the oxidized Si etch rate under the edge and the center of the catalyst varies due to the limited transport, thus, effective etch rate decreases with increasing catalyst dimension. Geyer et al. experimentally demonstrated the mass transport by varying the catalyst lateral dimension in continuous catalysts with micro-sized pore arrays and isolated nano stripe arrays [12]. Based on the decreasing etch rate with increasing stripe width, they suggested that the transport of the reactants and byproducts under the catalyst influences the etch rate and profile.

It is generally accepted that both carrier generation and mass transport affect MacEtch, and the etch rate and the etch profile are governed by the dominant transport process. However, as yet, there is no experimental evidence showing the coexistence of both transports, and how the etching condition can manipulate the dominance of either transport. It is important to understand the transport mechanisms in quantitative point of view since both mechanisms are required for etch rate estimation and etch stability control in any catalyst dimension.

1.4 State-of-the-Art Sub-Micron Scale Silicon Via Array by MacEtch and CMOS-Compatible MacEtch

1.4.1 State-of-the-Art Sub-Micron Scale Silicon Via Array by MacEtch

The process of fabricating high aspect ratio silicon via array using MacEtch is an important technique that can be applied in optoelectronics and 2.5/3D transistors. In optoelectronics, MacEtched via array can be used as the 2D photonic crystals and semiconductor metamaterials [4]. In 2.5/3D transistors, it can be used for 2.5/3D packages and integrated circuits [17]. Replacing the conventional reactive ion etching (RIE) process with MacEtch can minimize the unrepairable surface damages, scallops and defects that can significantly degrade the device performance. Furthermore, MacEtch can accommodate the formation of via array features with uniform diameters, whereas RIE is limited to the formation nanometer-scale features with tapered profiles.

However, MacEtch of via array using the sub-micron discrete catalyst array is still much more challenging compared to one using the large continuous catalyst. This is because the catalyst becomes more vulnerable and sensitive to any perturbations as the catalyst size decreases. There are external and internal perturbations which can affect the etch rate and etch stability. External perturbation can be defined as the agitation from the environmental sources such as temperature,

stage vibration, and light. Internal perturbation can be defined as the catalyst instability from the unbalanced carrier and mass transports.

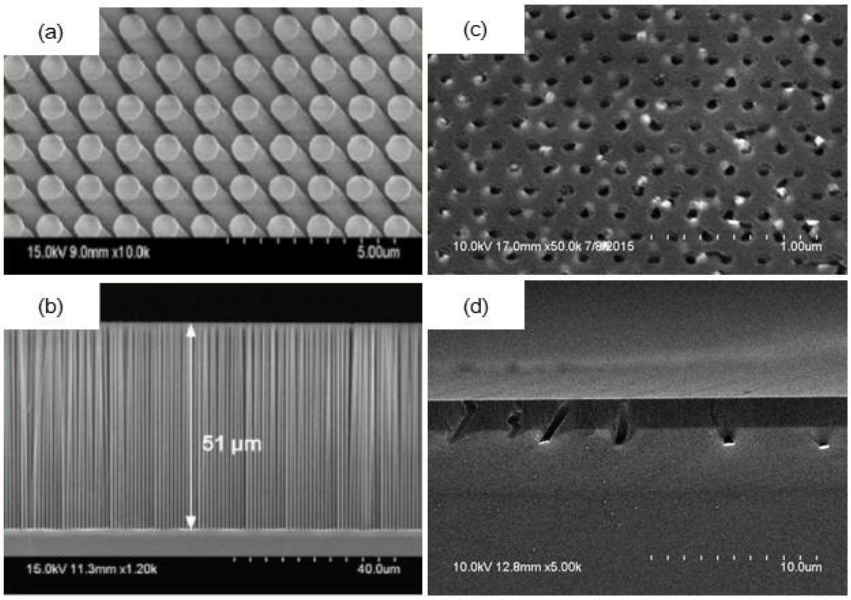

Figure 1.3: SEM image of the (a), (b) high aspect ratio nanowires MacEtched using the mesh patterned catalyst, and (c), (d) detoured via MacEtched using the discrete dot catalysts array [18].

Figure 1.3 (a) and (b) show the tilted top and cross-sectional SEM images of the high aspect ratio Si NWs MacEtched using the mesh patterned catalyst [18]. Figure 1.3 (c) and (d) show the tilted top and cross-sectional SEM images of the detoured via MacEtched using the discrete dot catalyst array. The carrier and the mass transports are critical in small discrete catalyst than in large continuous catalyst. For large catalyst, the carrier generation is sufficient that the etching is heavily governed by the mass transport, and this can be easily tuned by HF to oxidant concentration [12]. For small discrete catalyst, both uneven hole injection and uneven etch rate of the oxidized Si can detour the etching direction, thus, it is sensitive to both HF and oxidant concentrations.

MacEtch of via array using novel MacEtch techniques were reported. Li et al. demonstrated the micron scale TSV using the electric bias-attenuated MacEtch [8]. They used the external bias

across the Si substrate during the MacEtch to trap the holes only under the catalyst to minimize the sidewall chemical etching caused by hole diffusion. However, the sub-micron dimension via array by MacEtch is not included in this report. Balasundaram et al. reported the method of fabricating sub-micron scale via array on silicon-on-insulator using the magnetic field-guided MacEtch (h-MacEtch) [4].

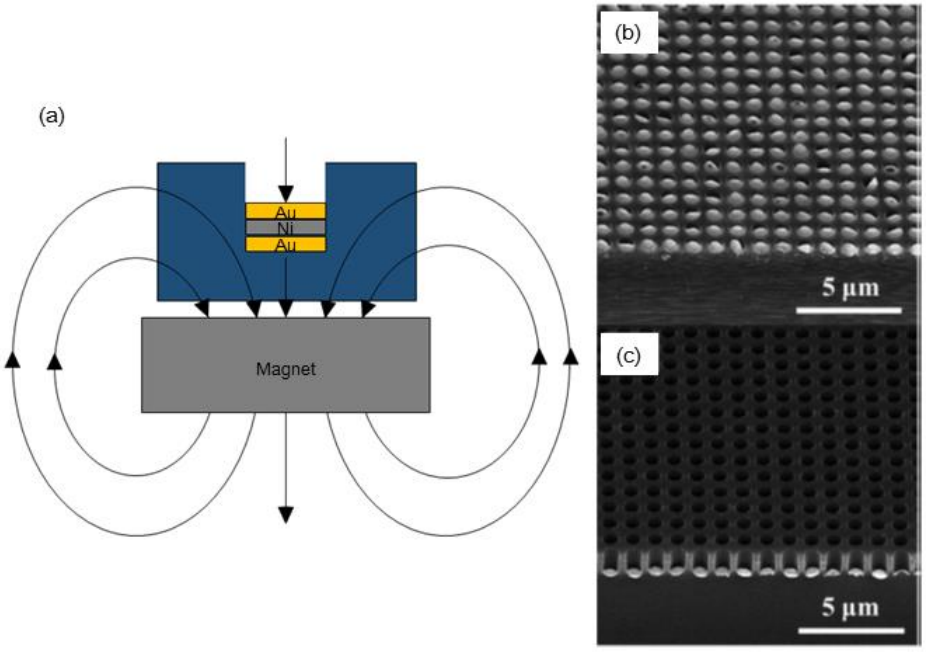

Figure 1.4: (a) Cross-section schematic of the magnetic induced MacEtch, (b) tilted cross-section SEM image of the 550 nm diameter and 1 µm pitch dot array MacEtched without magnetic field, (c) SEM image of the same dimension catalyst array MacEtched with magnetic field [4].

Figure 1.4 (a) shows the cross-sectional schematic of the h-MacEtch. They deposited the tri-layer metals of Au-Ni-Au, and used externally applied magnetic fields to force the Ni perpendicular to the substrate to minimize the catalyst detouring, and demonstrated the etch depth as function of a catalyst diameter from 900 nm to 400 nm at fixed pitch of 1 µm. Figure 1.4 (b) and (c) show the dot catalyst array of 550 nm diameter and 1 µm pitch MacEtched with/without the magnetic field respectively. However, there are some challenges of using h-MacEtch to achieve

a high aspect ratio via array in nanoscale discrete catalysts. As the catalyst diameter decreases, the volume of the Ni is reduced, thus, pull force from the magnetic field becomes too small for overcoming non-vertical etching paths. Also, exposed Ni in tri-layered catalysts gets etched by HF so that the etch time guided by h-field is limited for the small diameter catalysts.

1.4.2 State-of-the-Art CMOS-Compatible MacEtch

MacEtch using many different kinds of noble metals such as Au, Ag, Pt, Cu were reported [5, 15, 19, 20]. However, all the reported noble metal catalysts are not allowed in the CMOS process due to the deep level trap in Si substrate.

Table 1.1: Materials classification for CMOS process.

Level 0	Si, SiO, SiN
Level 1	Ge, Ga, As, In, P, AlO, GeSn, HfO, HfSiO, GaAs, InGaAs, InP, InAlAs
Level 2	Al, Ba, Dy, Gd, La, Lu, Mg, Ta, Ti, V, W, Zr, Sc,Sr, Nb, Mo, Yb, BaHfO, DyScO, GdScO, NbTaO, TaN, TiN, SrTiO, Silicides
Level 3	Cu, CuMn, Co, Ni, Zn, Ru, RuTa, RuTiN, Mn, Re, I
Level 4	Fe, Ir, Pd, Pt, Ag, IrO
Level 5	Au, Li, and any material for which no material assessment is available

Table 1.1 shows the lists of example materials classified in terms of allowed CMOS processing levels. Materials in Level 5 are not allowed in the CMOS fabrication. The materials in Level 4 are only limited for specific processing such as memory applications. The materials in

Level 3 are only allowed for back end of line (BEOL) processing. The materials in Levels 0, 1, and 2 are allowed for front end of line (FEOL) processing.

There are two conditions that the material must be satisfied in order to be used as the Si MacEtch catalyst. First, the catalyst has to be resistive to HF. If the catalyst gets etched by HF, high aspect ratio features cannot be fabricated with longer etching time. Second, the catalyst has to be capable of injecting holes by cathode reaction to produce the oxidized Si.

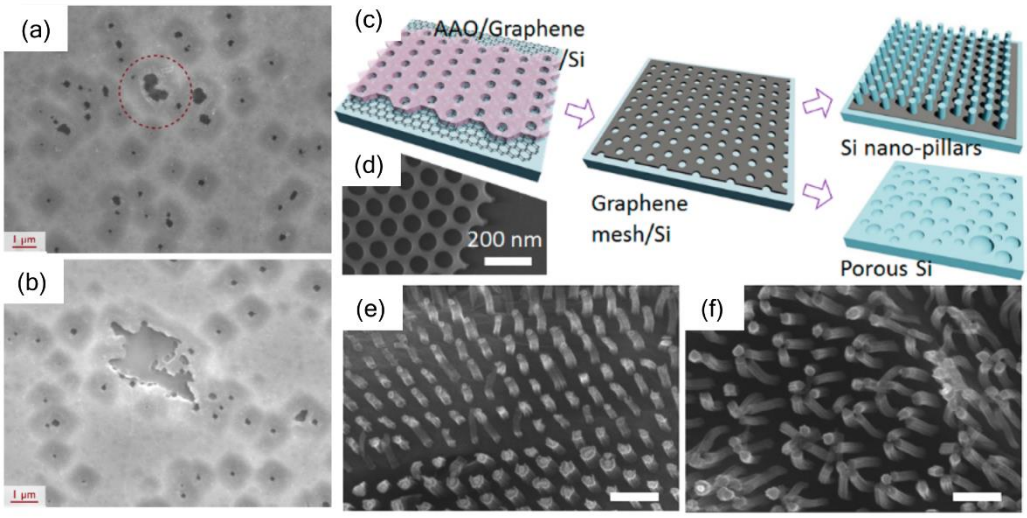

Figure 1.5: Both (a) and (b) show SEM images of porous Si MacEtched using tungsten nanoparticles, (c) shows the schematics of graphene-assisted chemical etching with the mesh patterned graphene using an anodic aluminum oxide (AAO) template, (d) shows SEM image of the AAO template, (e) and (f) show SEM images of Si nanowires formed after graphene-assisted chemical etching [6, 21].

Tungsten (W) MacEtch is reported by Hildreth et al. [6] in 2010. They MacEtched the W nanoparticles deposited on the Si substrate using HF and H_2O_2, and observed the formation of porous Si. Figure 1.5 (a) and (b) show the porous Si MacEtched using W nanoparticles. However, W is not resistive to HF, and MacEtch using patterned W catalysts are not reported.

Graphene-assisted chemical etching is reported by Kim et al. [21] in 2015. They patterned graphene using an anodic aluminum oxide (AAO) template as shown in Figure 1.5 (c) and (d) and formed NWs by etching in HF and H_2O_2 at 45 °C as shown in Figure 1.5 (e) and (f). However,

graphene-assisted chemical etching is limited for sub 100 nm diameter mesh patterns and the forward etching is only capable of using solution at high temperature due to the limited mass transport.

2. MACETCH OF SUB-MICRON SCALE CRYSTALLINE SILICON VIA ARRAY

In this chapter, fabrication of sub-micron scale closely packed crystalline Si via array by MacEtch is presented. The method of fabricating the vertical, uniform via array as well as catalyst delamination and detour resulted from the poor catalyst and substrate interface are discussed. Then, the vertical etch rate as the function of diameter, pitch and spacing of the discrete catalyst array at varied H_2O_2 concentration is systematically analyzed to realize the experimental demonstration of carrier generation (CG) and mass transport (MT) mechanisms in MacEtch. Based on the experimental etch rate data, empirical etch rate model is constructed to simulate the extreme etching conditions where the CG or MT is dominating. With the guidance of experimental and simulation data, Si via arrays with 320 nm diameter and 400 nm pitch with aspect ratio larger than 10 is fabricated by MacEtch.

2.1 Fabrication Process

The baron doped p-type (100) oriented single crystalline Si substrates with resistivity of 1 – 20 Ω-cm were used for every experiment. First, substrates were treated with the cleaning process; the organic containments were removed in 1:1:5 ammonium hydroxide (NH4OH):H_2O_2:DI water at 80 °C. The native oxide was etched in 1:10 buffer oxide etchant (BOE). The ionic contaminant was removed in 1:1 hydrogen chloride (HCL): DI water. The substrates were dried with N_2.

After the cleaning process, the samples were spin-coated with the electron beam (e-beam) resist of 950 k PMMA in 2% anisole at 2500 rpm for 30 s and baked at 200 °C for 2 min to deposit the 80 nm thickness resist. Next, the specified dot array patterns were exposed using the e-beam lithography with 10 kV beam voltage, 20 μm aperture and area exposure mode. The diameter of

the dot arrays was coarse-tuned with areal dose of 100 μC cm^{-2} and fine-tuned with local e-beam dosage.

After the exposure, samples were developed in 1:3 methyl isobutyl keton (MIBK):IPA for 2 min at room temperature and rinsed in IPA for 30 s. The PMMA residue and native oxide on the exposed patterns were cleaned in 1:1 HCL:DI water for 1 min and 1:10 BOE for 2 min, respectively.

Then, the 10 nm Au was deposited by e-beam evaporator. The Au film on the PMMA was lifted off in Remover PG (MicroChem Corp) for 30 min at 60 °C and rinsed with four cycles in IPA for 30 s.

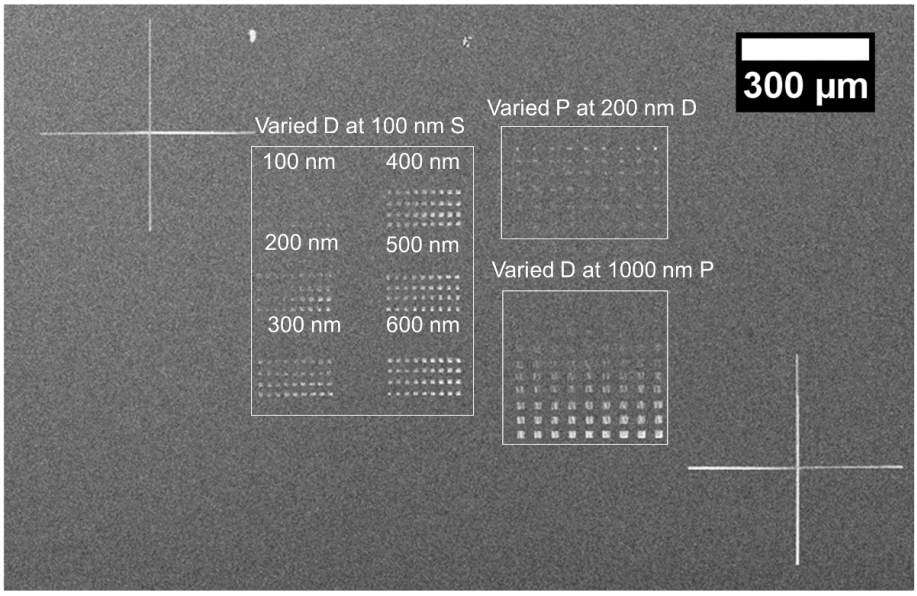

Figure 2.1: Top view of a low-magnification SEM image of the sample before MacEtch containing the arrays with varied diameter at 1000 nm pitch for diameter study, varied pitch at 200 nm diameter for pitch study and varied diameter at 100 nm spacing for spacing study.

Figure 2.1 shows the top view of a low-magnification SEM image of the sample after the Au liftoff. Each sample contains the arrays with varied diameter from 100 to 900 nm at fixed pitch of 1000 nm for a diameter study, varied pitch from 300 nm to 900 nm at fixed 200 nm diameter for a pitch study and varied diameter from 100 nm to 600 nm at fixed spacing of 100 nm for a

spacing study to make sure the all the catalyst arrays were etched in the same solution for the same time to minimize the offset.

The samples were MacEtched in the solution of 49% HF, 30% H_2O_2, IPA, and DI for 10 min. The HF to H_2O_2 ratio is defined as $\rho_{H_2O_2}$ which is described as

$$\rho_{H_2O_2} = \frac{H_2O_2[M]}{HF[M]+H_2O_2[M]} \tag{2.1}$$

where $H_2O_2[M]$ and $HF[M]$ indicate the molar concentrations of HF and H_2O_2, respectively. For the experiments, HF was fixed as 0.56 M and the H_2O_2 was varied with 0.13, 0.26, 0.39, 0.52 M such that the value of 0.19, 0.32, 0.41 and 0.48 $\rho_{H_2O_2}$ were used for extracting the vertical etch rate data.

After the MacEtch, the top view of etched via arrays were inspected with a Hitachi S-4800 SEM. When the top view SEM image showed uniform vertical etching without the catalyst delamination or detouring, the vertical etching depth was inspected with an FEI DB-235 dual-beam focused ion beam (FIB) system. For the FIB, Ga+ ion currents of 10 pA was used at 30 kV accelerating voltage for sample mitigation. First, a regular cross-section milling pattern was used to mill down to the bottom of the Au catalyst. Then, a cleaning cross-section milling pattern was used to mill the redeposited debris that resulted from the initial cross-section milling process.

2.2 Metal/Substrate Interface on Catalyst Delamination and Detouring

The MacEtch of catalyst specifically for sub-micron scale discrete catalyst is sensitive to the defects and the polymer residue between the catalyst and substrate interface. Any surface contamination can result in the catalyst delamination or liftoff during the etching process such that it is important to optimize the e-beam dosage, developing time and PMMA residue cleaning process according to the PMMA type and thickness.

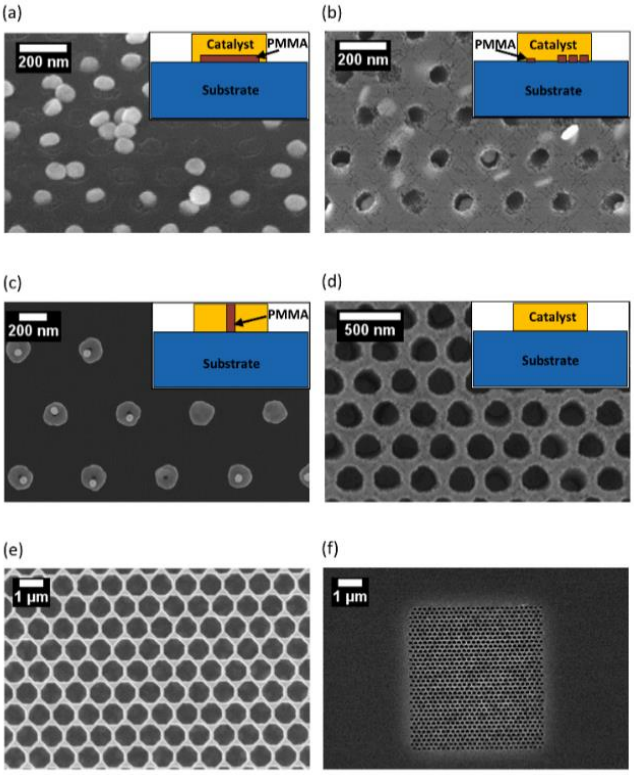

Figure 2.2: Top view SEM images of MacEtched catalyst arrays showing (a) catalyst delamination resulted by underexposed or underdeveloped patterns, (b) catalyst detour resulted by partially underexposed or partially developed patterns, (c) no vertical etching due to the formation of carbonized PMMA from the overexposed patterns, (d) uniform vertical MacEtch at optimized e-beam dosage and developing time, (e) uniform via array of 900 nm diameter with 1 µm pitch MacEtched at clean interface, (f) uniform via array of 100 nm diameter with 200 nm pitch MacEtched at clean interface. The subset images show the corresponding cross-sectional illustrations of the interface between catalyst and substrate.

Figure 2.2 (a) to (d) show the SEM images of the four different MacEtch results that are produced from the different PMMA exposure and developing time. Figure 2.2 (a) shows the top view SEM image of the MacEtched sample when the patterns are underexposed or underdeveloped. For the PMMA used in this experiment, this occurs when the e-beam dosage is smaller than 80 µC/cm^2 or when the PMMA developing time is less than 60 s. In this case, a thin layer of PMMA remains between the catalyst and the substrate, and it blocks the redox reaction during the MacEtch process; the Si localized under the catalyst cannot be oxidized and dissolved. During the MacEtch, PMMA film is etched by HF from edge to center under the Au catalyst which

results the catalyst to be delaminated. On the Si surface where the catalyst was originally placed, the ring-shaped trenches are observed. This is the result of the MacEtch on the catalyst edge during the process of the PMMA etching. Once the PMMA is completely dissolved, the surface tension and van der Waals forces between the catalyst and the substrate is overwhelmed by the fluid motion such that disks are no longer remain anchored. Figure 2.2 (b) shows an SEM image of a MacEtched sample when the patterns are partially exposed or partially developed. This occurs when the e-beam dosage is between 80 $\mu C/cm^2$ and 110 $\mu C/cm^2$ or when the PMMA developing time is less than 90 s. In this case, the clusters of PMMA residues remain between catalyst and substrate. The MacEtch only occurs on the clean interface while the PMMA residue serves as the anchor until it is completely dissolved. As the result, the catalyst detours to the direction where the PMMA residue remains. The direction of the catalyst detouring is non-uniform since the size and the location of the PMMA residues are inconsistent. Figure 2.2 (c) shows a SEM image of a MacEtched sample when the patterns are overexposed. This happens when the e-beam dosage is higher than 300 $\mu C/cm^2$. When the PMMA is overexposed, PMMA gets carbonized by polymer cross-liking such that it is not dissolvable in the developer [22]. After developing, in the center of exposed dot contains the pillar-like carbonized PMMA. During the MacEtch, this pillar anchors the catalyst such that the vertical etch rate slows down. The carbonized PMMA is also etched by HF and the Au deposited on the pillar is delaminated. The uniform vertical MacEtch can be achieved only when the interface between the catalyst and substrate is clean. Figure 2.2 (d) and (e) show SEM images of MacEtched samples with 100 nm and 600 nm diameter catalyst arrays at optimized e-beam exposure and developing time. Figure 2.2 (f) shows a low magnification SEM image of a MacEtched sample with a 100 nm diameter at a 200 nm pitch showing the uniform etching without the catalyst delamination or detouring.

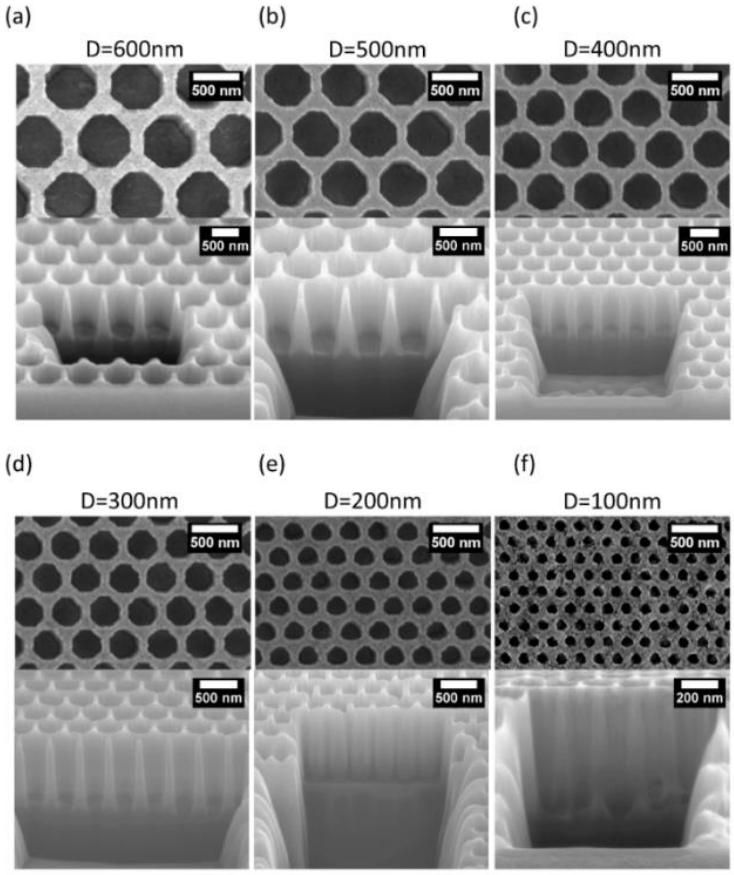

Figure 2.3: SEM images of MacEtched dot arrays in a solution of 20 ml HF, 30 ml H_2O_2, 16 ml DI, 16 ml IPA for 10 minutes with the dimension of (a) 600 nm diameter, (b) 500 nm diameter, (c) 400 nm diameter, (d) 300 nm diameter, (e) 200 nm diameter, and (f) 100 nm diameter at fixed spacing of 100 nm.

Figure 2.3 (a) to (f) shows sets of top and 52° tilted-view SEM images after cross-sectional FIB of via array samples with the diameters of 600 nm, 500 nm, 400 nm, 300 nm, 200 nm, and 100 nm at fixed spacing of 100 nm that are MacEtched in a solution of 0.41 $\rho_{H_2O_2}$ for 10 minutes. The tilted images show that the diameters of the vias decreases as the depth increases due to material redeposition during the ion milling. Notably, the lateral motion of catalysts, referred to as "detouring", is effectively quenched under these etching conditions. This is due to the consequence of both an optimized pattering procedure as well a balanced MT vs. CG regime, as further supported in the following discussion.

2.3 Diameter Dependence

Figure 2.4 to Figure 2.7 show top and 52 degree tilted SEM images of the via array with the diameter from 100 nm to 900 nm at fixed pitch of 1 μm that were MacEtched with 0.19, 0.32, 0.41, 0.48 $\rho_{H_2O_2}$.

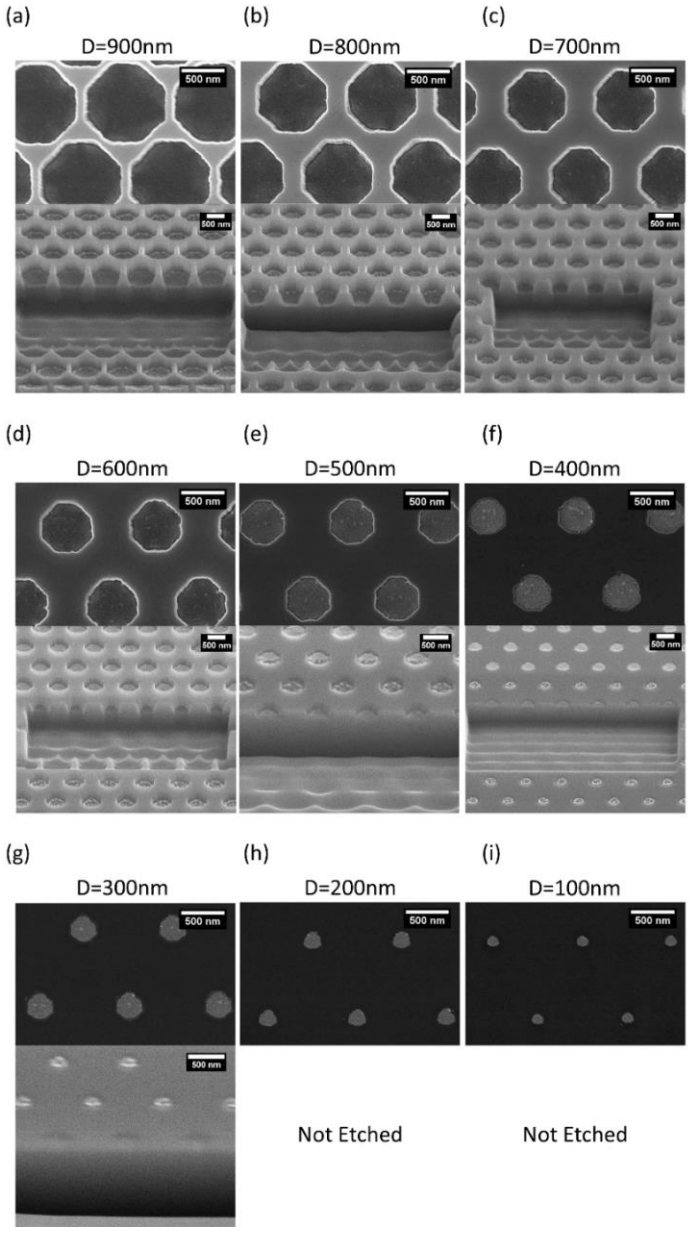

Figure 2.4: Top view (top) and 52 degree tilted view (bottom) SEM images of MacEtched dot arrays in a solution of 0.56 M HF, 0.13 M H_2O_2, 0.88 M DI, 0.21 M IPA ($\rho_{H_2O_2}$ = 0.19) for 10 minutes with the diameter of (a) 900 nm, (b) 800 nm, (c) 700 nm, (d) 600 nm, (e) 500 nm, (f) 400 nm, (g) 300 nm, (h) 200 nm, and (i) 100 nm at fixed pitch of 1 μm.

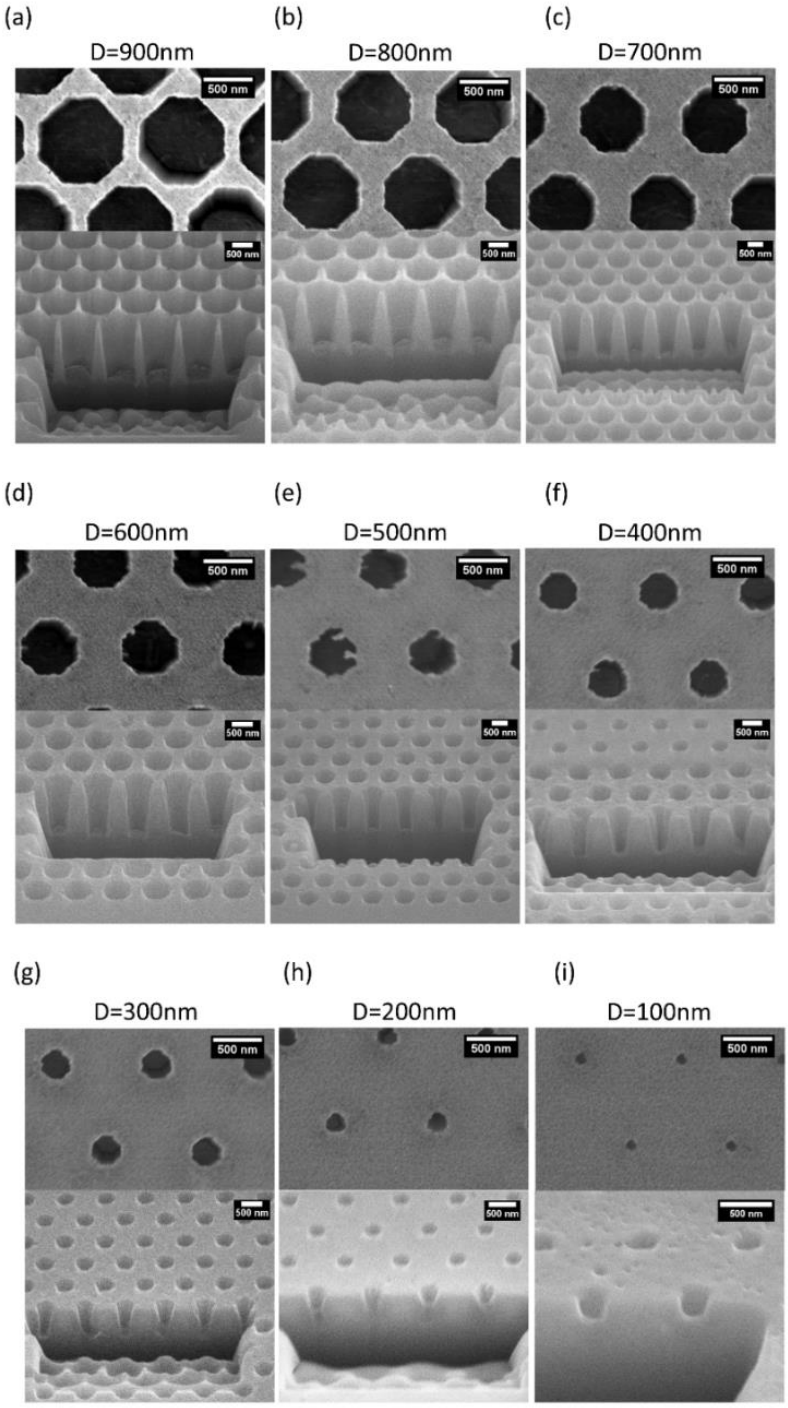

Figure 2.5: Top view (top) and 52 degree tilted view (bottom) SEM images of MacEtched dot arrays in a solution of 0.56 M HF, 0.26 M H_2O_2, 0.88 M DI, 0.21 M IPA ($\rho_{H_2O_2}$ = 0.32) for 15 minutes with the diameter of (a) 900 nm, (b) 800 nm, (c) 700 nm, (d) 600 nm, (e) 500 nm, (f) 400 nm, (g) 300 nm, (h) 200 nm, and (i) 100 nm at fixed pitch of 1 µm.

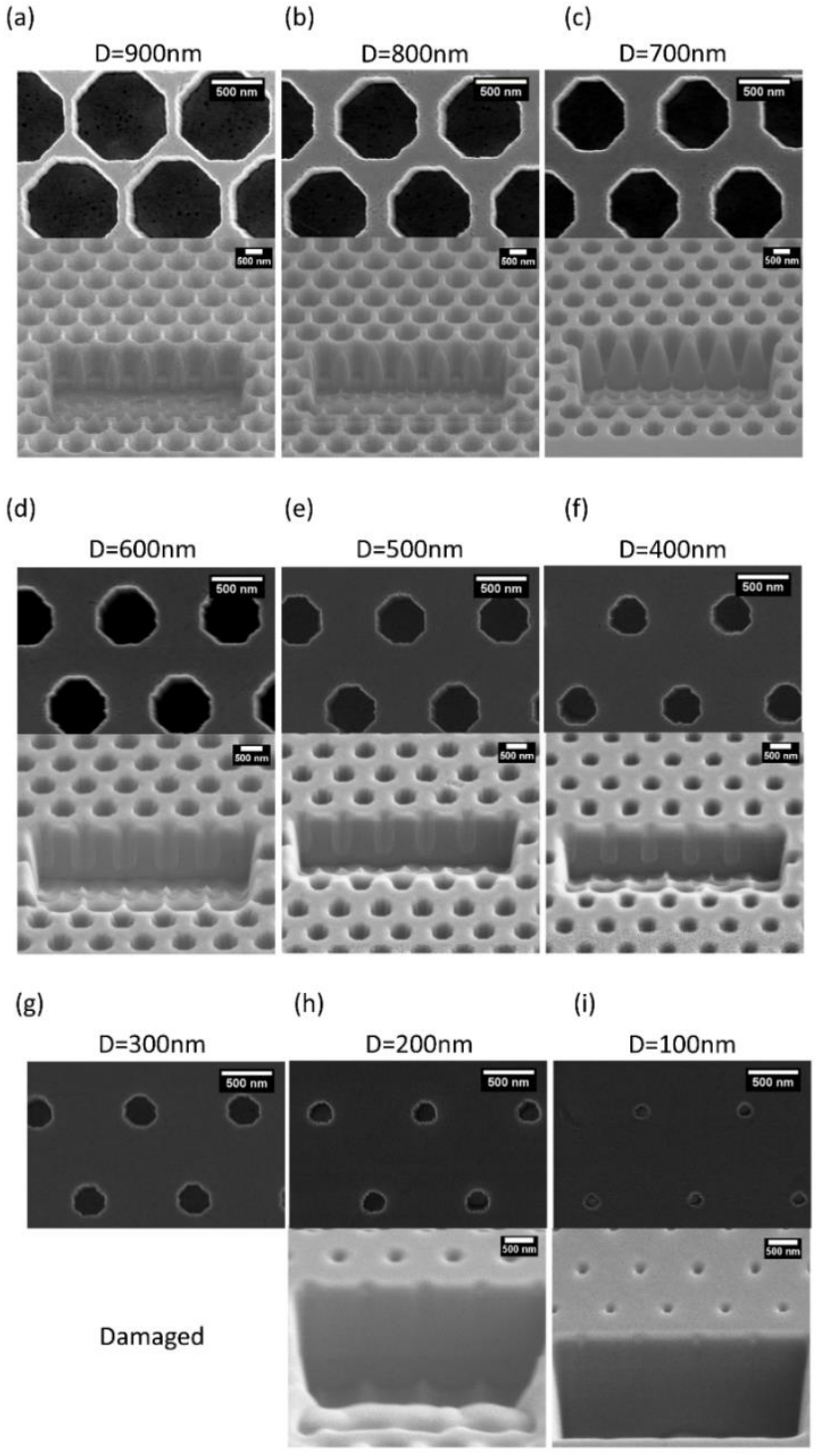

Figure 2.6: Top view (top) and 52 degree tilted view (bottom) SEM images of MacEtched dot arrays in a solution of 0.56 M HF, 0.39 M H_2O_2, 0.88 M DI, 0.21 M IPA ($\rho_{H_2O_2}$ = 0.41) for 10 minutes with the diameter of (a) 900 nm, (b) 800 nm, (c) 700 nm, (d) 600 nm, (e) 500 nm, (f) 400 nm, (g) 300 nm, (h) 200 nm, and (i) 100 nm at fixed pitch of 1 μm.

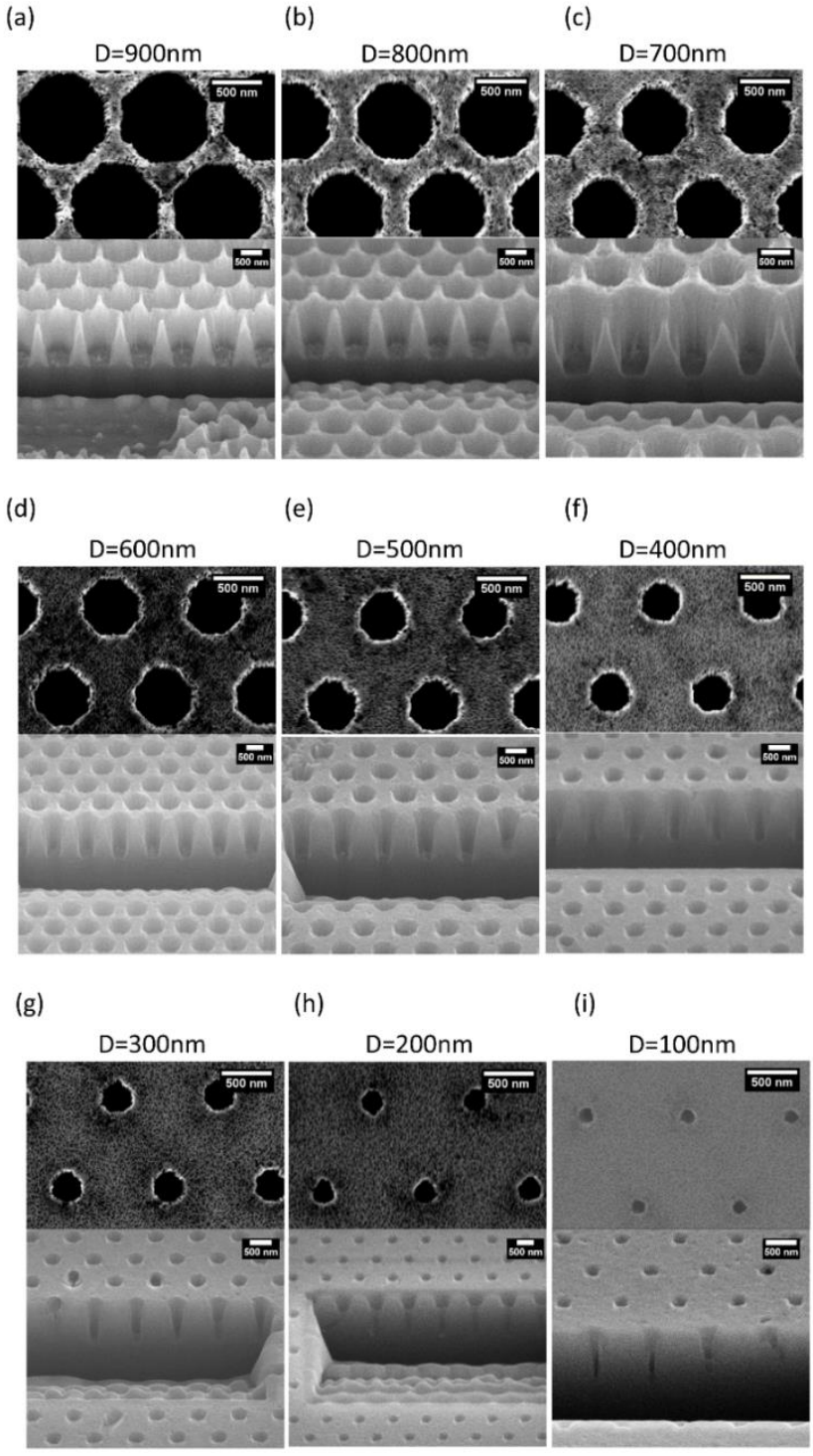

Figure 2.7: Top view (top) and 52 degree tilted view (bottom) SEM images of MacEtched dot arrays in a solution of 0.56 M HF, 0.52 M H_2O_2, 0.88 M DI, 0.21 M IPA ($\rho_{H_2O_2}$ = 0.48) for 10 minutes with the diameter of (a) 900 nm, (b) 800 nm, (c) 700 nm, (d) 600 nm, (e) 500 nm, (f) 400 nm, (g) 300 nm, (h) 200 nm, and (i) 100 nm at fixed pitch of 1 μm.

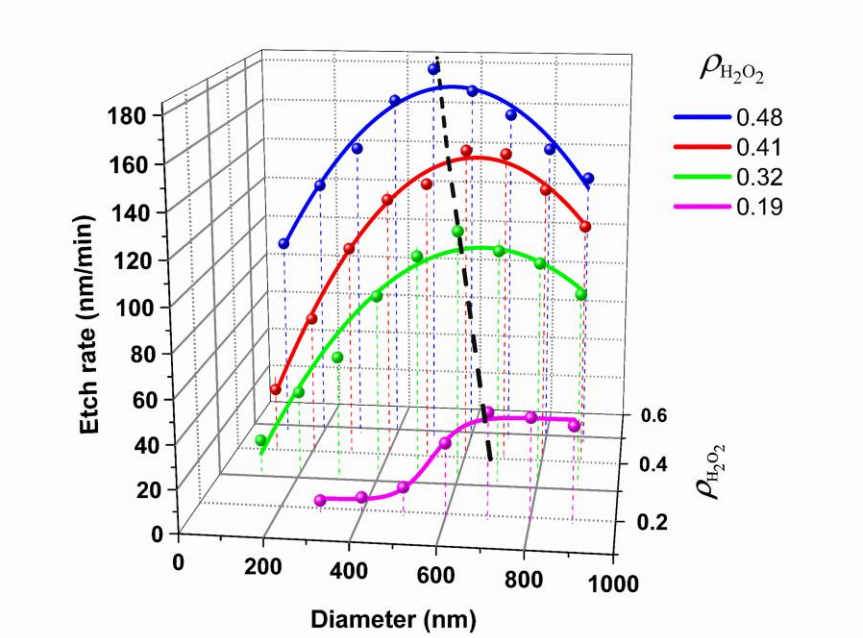

Figure 2.8: Vertical etch rate plotted as a function of diameter from 100 nm to 900 nm at fixed pitch of 1 μm that were MacEtched at $\rho_{H_2O_2}$ of 0.19, 0.32, 0.41 and 0.48.

Figure 2.8 shows the measured average vertical etch rate as a function of diameter from 100 nm to 900 nm at a fixed pitch of 1 μm that were MacEtched at $\rho_{H_2O_2}$ of 0.19, 0.32, 0.41 and 0.48. As can be seen, the etch rate trends in every conditions show inverted parabolic curves. For the 0.48 $\rho_{H_2O_2}$ the etch rate increases from 130 nm/min to 180 nm/min as the diameter decreases from 900 nm to 500 nm. The etch rate starts to decrease from 180 nm/min to 100 nm/min as the diameter decreases to 100 nm. The diameter where the etch rate is the highest is defined as the D_M (D_M = 500 nm for 0.48 $\rho_{H_2O_2}$). When the $\rho_{H_2O_2}$ decreases from 0.48 to 0.19, the etch rate in every diameter decreases, and more importantly, D_M is shifted from 500 nm to 700 nm.

The increase in vertical etch rate with decreasing diameter is due to the enhanced MT. As the catalyst diameter decreases, the effective volume of the oxidized Si formed under the catalyst also reduces. The vertical etching is enabled when the oxidized Si is completely etched and the catalyst is sunk down to the bottom of etched via. Thus, the vertical etch rate enhances with

decreasing diameter since it takes shorter time for HF to etch away the oxidized Si under the catalyst.

The decrease in vertical etch rate with decreasing diameter is due to the limited CG. When the catalyst diameter decreases, CG decreases due to the reduced catalyst volume.

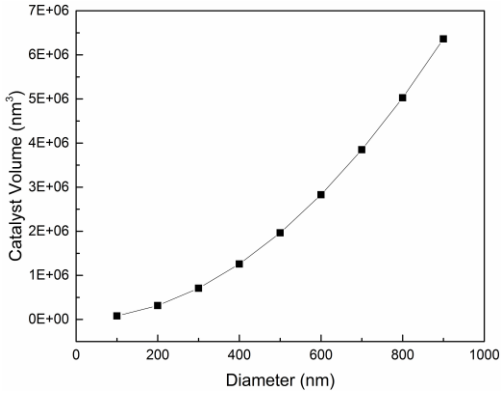

Figure 2.9: Catalyst volume as a function of diameter from 100 nm to 900 nm.

Figure 2.9 shows the calculated catalyst volume as the function of diameter from 100 nm to 900 nm at fixed thickness of 10 nm. The volume decreases by 79% as the diameter decreases from 900 nm to 100 nm. Because of less volume, a reduced number of holes are generated by the reduction reaction. It is important to note that the MT is simultaneously enhancing when the diameter decreases (increases the vertical etch rate). Thus, decrease in vertical etch rate below 500 nm diameter indicates that the etch rate decreased by the limited-CG is greater than the etch rate increased by enhanced-MT. The reduced etch rate in every diameter with decreasing H_2O_2 concentration is due to the reduced hole injection rate. D_M indicates the diameter where the CG and MT are maximized; the rate of hole injection to form the oxidized Si and the etch rate of the oxidized Si are both at maximum. The shifting of the D_M to a larger diameter with reduced $\rho_{H_2O_2}$ shows that the condition where the CG and MT maximum is changing; shifting to larger diameter indicates the etch rate of the oxidized Si becomes faster due to the higher concentration of HF.

2.4 Pitch Dependence

Figure 2.10 to Figure 2.12 show sets of top and 52 degree tilted SEM images of the via array with the varied pitch from 300 nm to 900 nm at fixed diameter of 200 nm that were MacEtched with 0.32, 0.41, 0.48 $\rho_{H_2O_2}$ respectively.

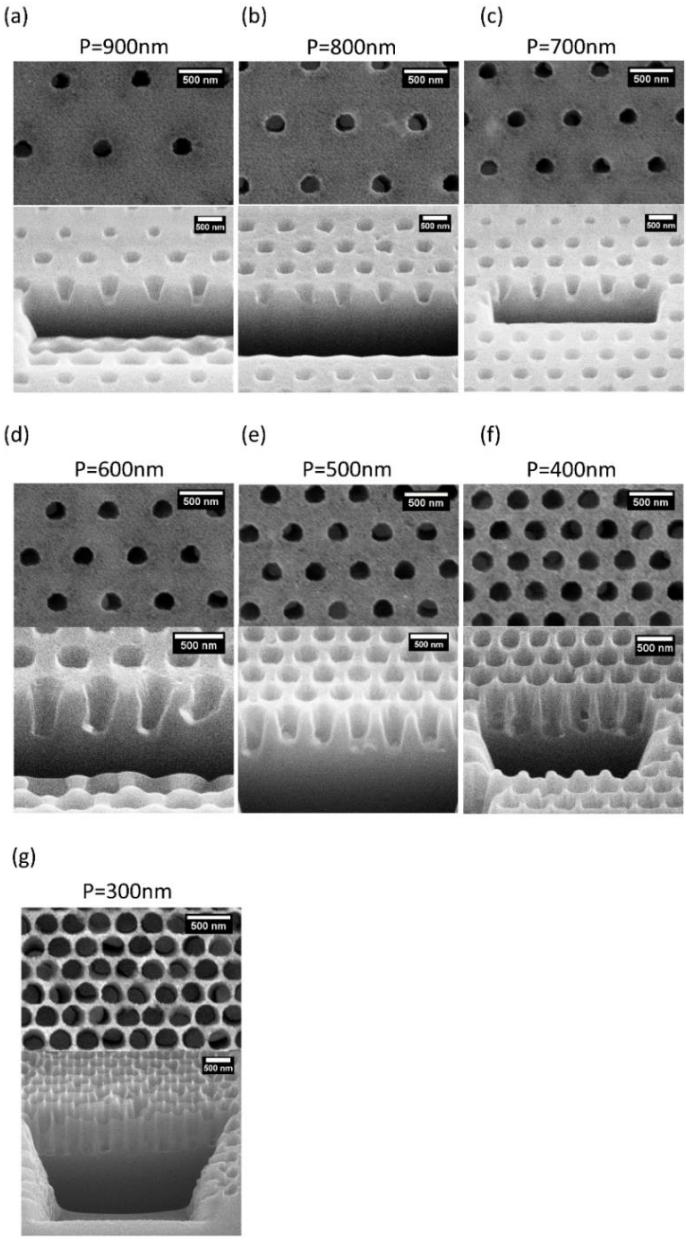

Figure 2.10: Top view (top) and 52 degree tilted view (bottom) SEM images of MacEtched dot arrays in a solution of 0.56 M HF, 0.26 M H_2O_2, 0.88 M DI, 0.21 M IPA ($\rho_{H_2O_2}$ = 0.32) for 15 minutes with the pitch of (a) 900 nm, (b) 800 nm, (c) 700 nm, (d) 600 nm, (e) 500 nm, (f) 400 nm, and (g) 300 nm at fixed diameter of 200 nm.

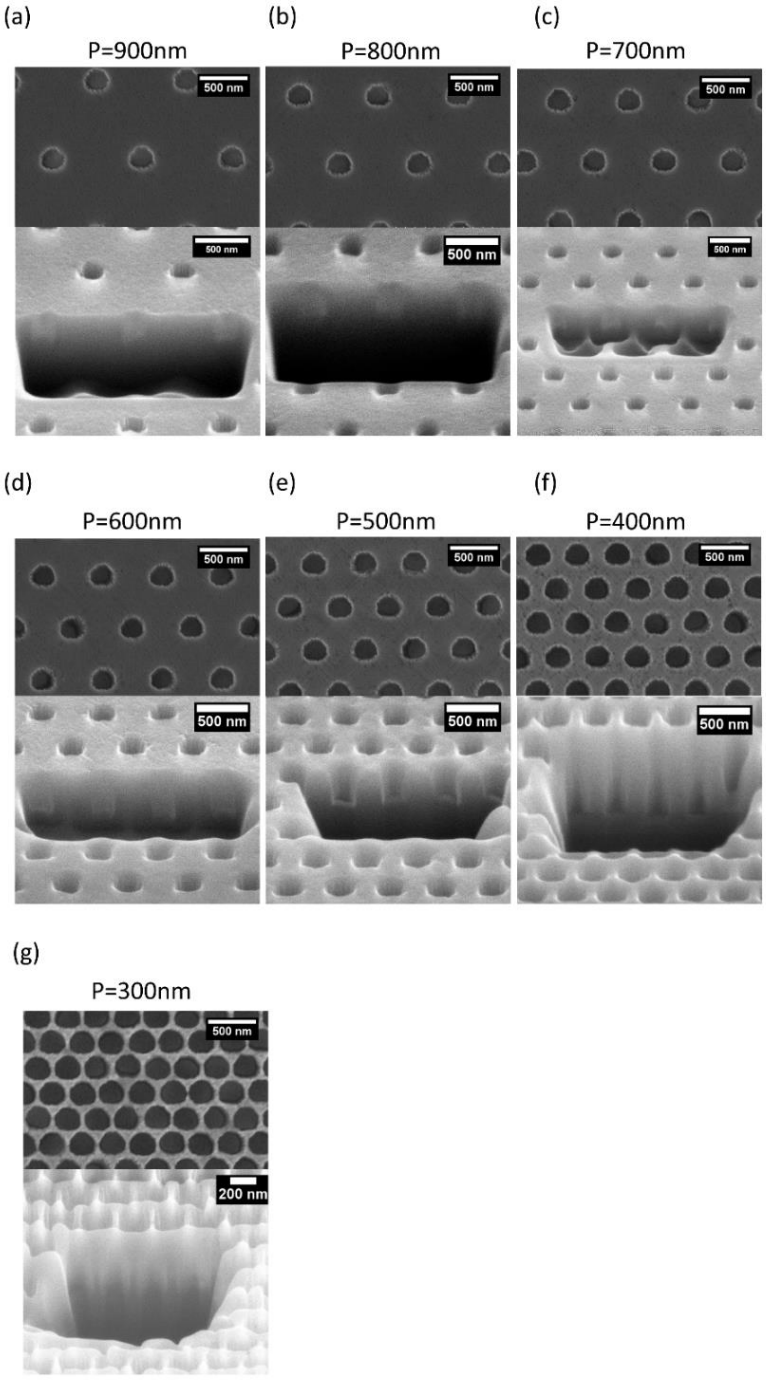

Figure 2.11: Top view (top) and 52 degree tilted view (bottom) SEM images of MacEtched dot arrays in a solution of 0.56 M HF, 0.39 M H_2O_2, 0.88 M DI, 0.21 M IPA ($\rho_{H_2O_2}$ = 0.41) for 10 minutes with the pitch of (a) 900 nm, (b) 800 nm, (c) 700 nm, (d) 600 nm, (e) 500 nm, (f) 400 nm, and (g) 300 nm at fixed diameter of 200 nm.

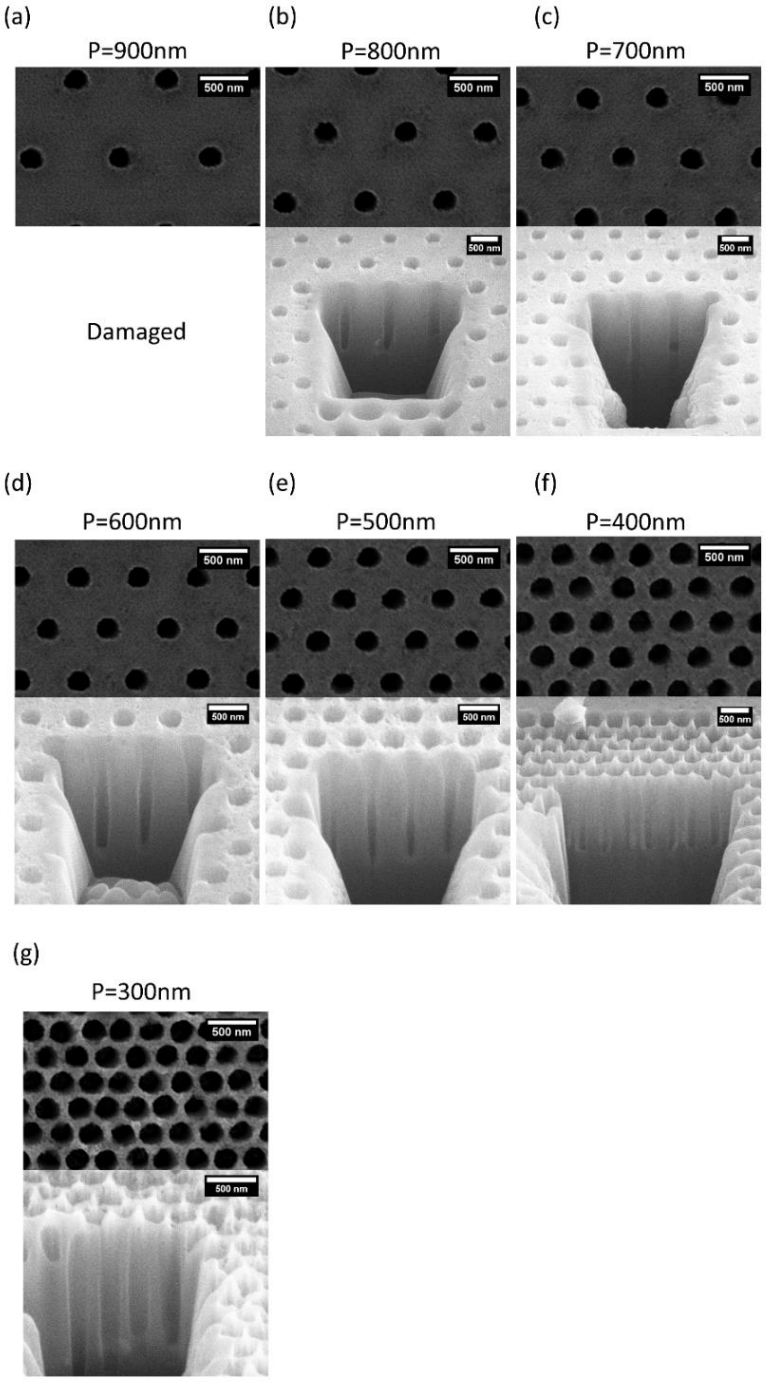

Figure 2.12: Top view (top) and 52 degree tilted view (bottom) SEM images of MacEtched dot arrays in a solution of 0.56 M HF, 0.52 M H_2O_2, 0.88 M DI, 0.21 M IPA ($\rho_{H_2O_2}$ = 0.48) for 10 minutes with the pitch of (a) 900 nm, (b) 800 nm, (c) 700 nm, (d) 600 nm, (e) 500 nm, (f) 400 nm, and (g) 300 nm at fixed diameter of 200 nm.

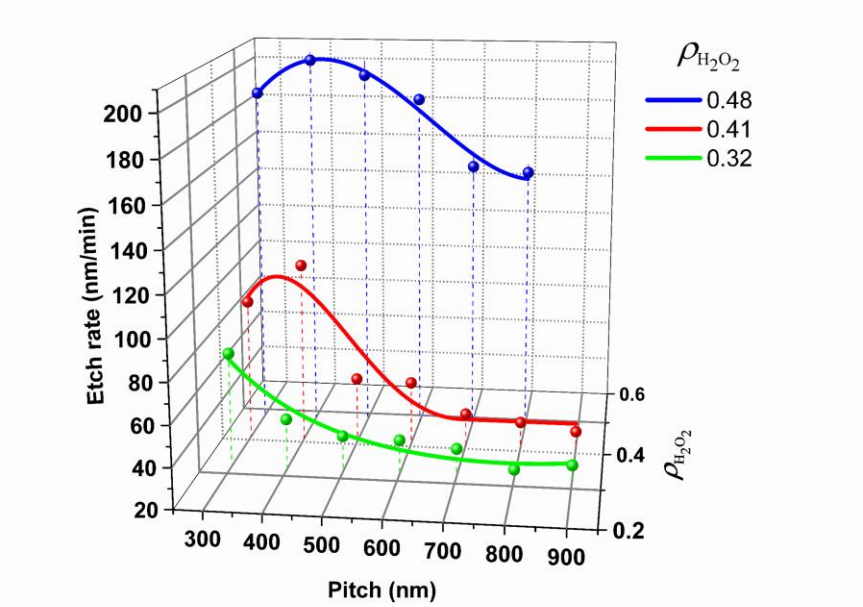

Figure 2.13: Vertical etch rate plotted as a function of pitch from 300 nm to 900 nm at fixed diameter of 200 nm, MacEtched at $\rho_{H_2O_2}$ of 0.32, 0.41 and 0.48.

Figure 2.13 shows the measured average vertical etch rate as the function of pitch from 300 nm to 900 nm at fixed diameter of 200 nm MacEtched at $\rho_{H_2O_2}$ of 0.32, 0.41, 0.48. For 0.32 $\rho_{H_2O_2}$, the vertical etch rate stays as the constant value for the pitch from 900 nm to 600 nm (slowly increases from 30 nm/min to 45 nm/min). The vertical etch rate increases from 45 nm/min to 80 nm/min as the pitch further decreases to 300 nm. The pitch where the etch rate starts to increase is defined as threshold pitch, P_{th}. As the $\rho_{H_2O_2}$ increases from 0.32 to 0.48, the vertical etch rate increases in every pitch and the P_{th} shifts from the 400 nm to 600 nm. For 0.41 and 0.48 $\rho_{H_2O_2}$, the vertical etch rate decreases as the pitch decreases from 400 nm to 300 nm.

The increased vertical etch rate with decreasing pitch below 600 nm results from the hole concentration overlap. During MacEtch, holes are continuously generated and injected in the Si. When the number of holes injected is larger than the number of the holes consumed, the unconsumed holes start to diffuse. When the unconsumed holes diffuse on the neighboring catalyst,

the effective hole concentration under the catalyst is increased by the overlapping that results in an enhanced etch rate similar to ones in higher H_2O_2 concentration. It is important to note that for a discrete catalyst, the etching direction can be detoured when the effective hole concentration is non-uniform; catalyst detours to the direction where the hole concentration is less. This proximity effect can be observed in the edge of the via array with small spacing at high H_2O_2 concentration.

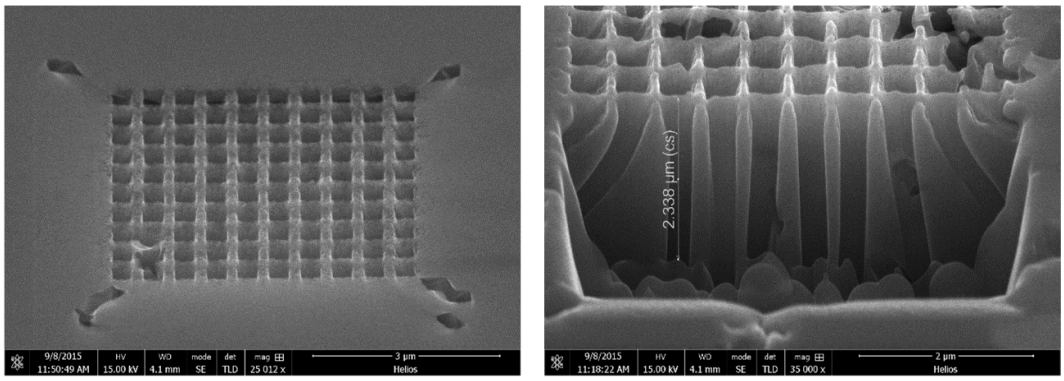

Figure 2.14: (a) Top view and (b) 52 degree tilted cross-sectional SEM of the via array with 300 nm diameter and 500 nm pitch showing the catalyst detouring at the edge of the array due to the proximity effect.

Figure 2.14 (a) and (b) shows the top view and 52 degree tilted cross-sectional SEM of the via array with 300 nm diameter and 500 nm pitch showing the catalyst detouring at the edge of the array due to the proximity effect.

The increase in P_{th} with increasing H_2O_2 concentration is due to the increased hole injection rate. With the increased hole injection rate, the diffusion rate of the unconsumed holes increases such that the hole concentration overlapping starts to occur in the larger pitch.

The decreased vertical etch rate below 400 nm pitch for 0.41 and 0.48 $\rho_{H_2O_2}$ is due to a reduced amount of shared MacEtch solution on each catalyst resulting from the increase in the

catalyst packing density. The packing density of the catalysts array is calculated using the rhombus unit cell, and it is described as

$$Packing\ Density = \frac{\pi r^2}{P\sqrt{P^2 - \left(P/2\right)^2}} \times 100 \qquad (2.2)$$

where r is the radius, P is the pitch of the catalyst array.

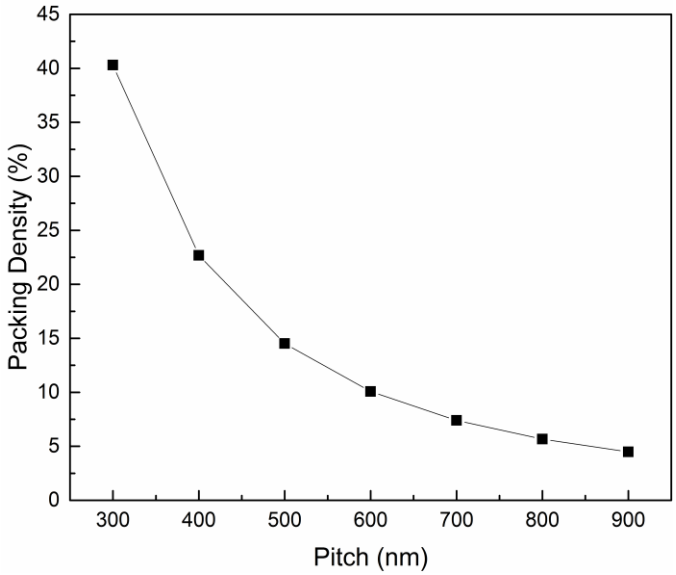

Figure 2.15: Calculated packing density of the catalyst array as function of the pitch from 300 nm to 900 nm at fixed diameter of 200 nm.

Figure 2.15 shows the calculated packing density of the hexagonally ordered 200 nm diameter catalyst as the function of the pitch from 300 nm to 900 nm. The packing density increases from 4.5% to 40.3% as the pitch decreases to 300 nm. The same amount of solution is shared by the catalyst array, and as the packing density increases, a lesser amount of the HF and H_2O_2 is shared in each catalyst. In this case where the catalyst pitch is small and the H_2O_2 concentration is large, the decrease in etch rate indicates that there is a smaller amount of HF that is shared on each catalyst.

2.5 Spacing Dependence

Figure 2.16 to Figure 2.18 show the set of top and 52 degree tilted SEM images of the via array with the varied diameter from 100 nm to 600 nm at fixed spacing of 100 nm that were MacEtched with 0.19, 0.32, 0.41, 0.48 $\rho_{H_2O_2}$ respectively.

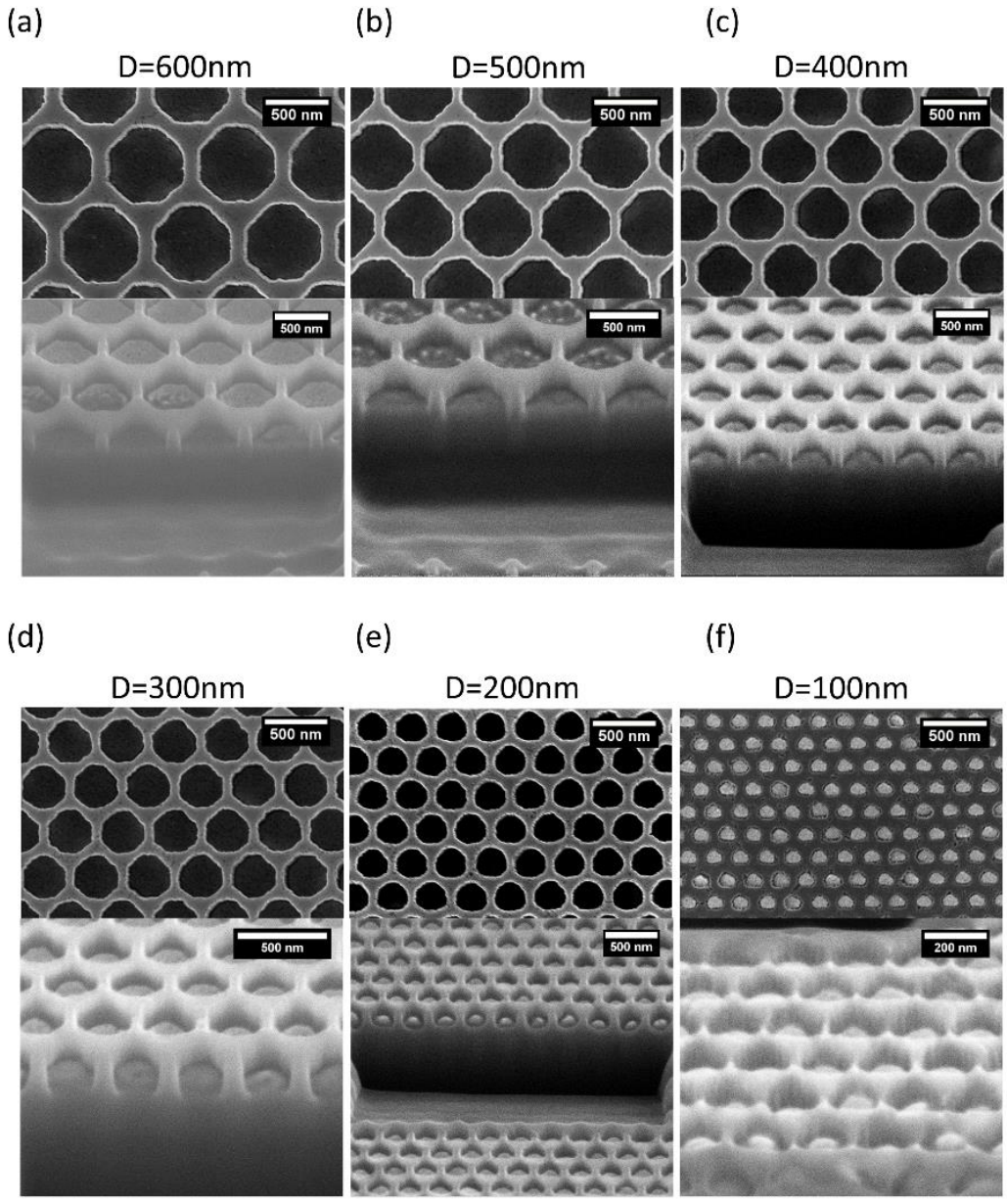

Figure 2.16: Top view (top) and 52 degree tilted view (bottom) SEM images of MacEtched dot arrays in a solution of 0.56 M HF, 0.13 M H_2O_2, 0.88 M DI, 0.21 M IPA ($\rho_{H_2O_2}$ = 0.19) for 10 minutes with the diameter of (a) 600 nm, (b) 500 nm, (c) 400 nm, (d) 300 nm, (e) 200 nm, and (f) 100 nm at fixed spacing of 100 nm.

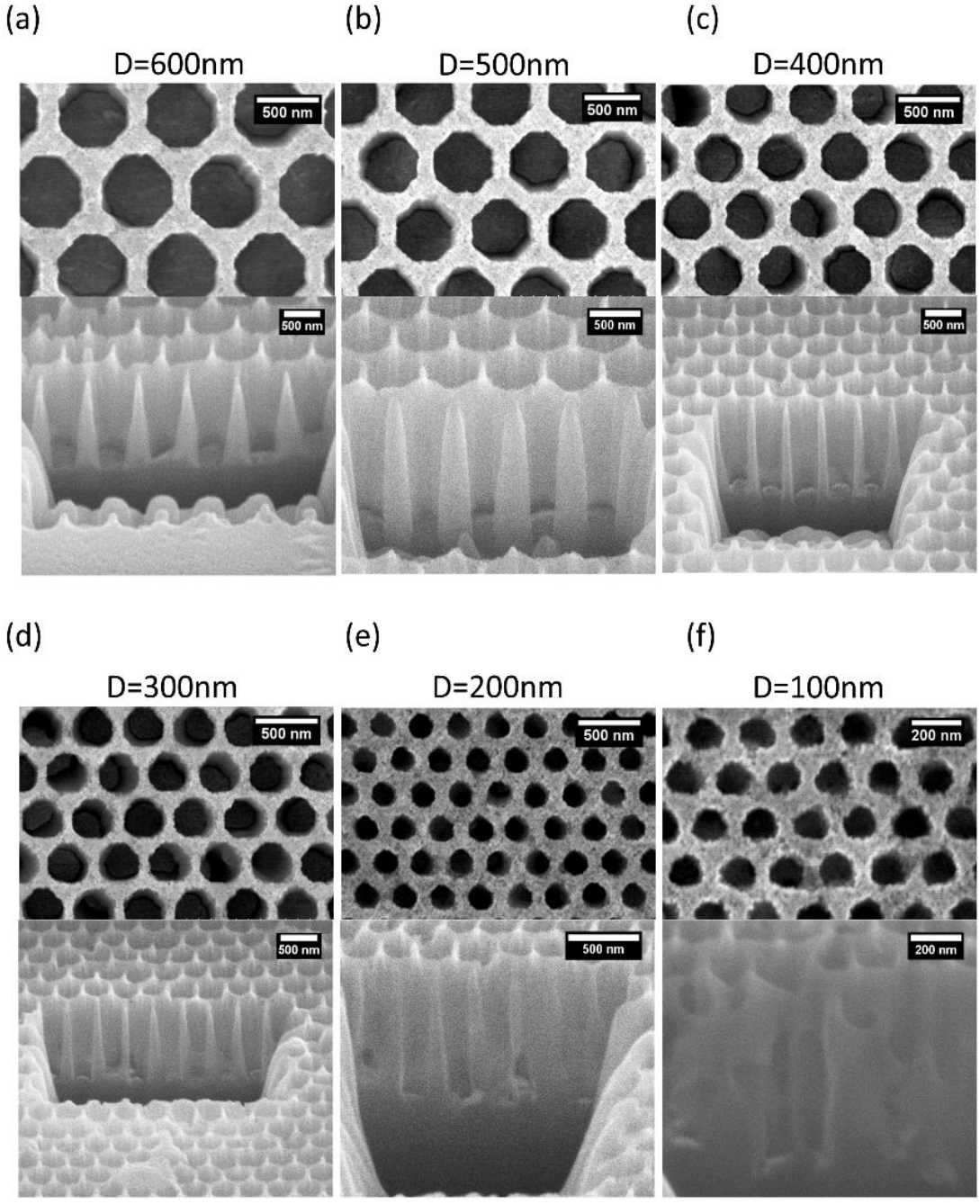

Figure 2.17: Top view (top) and 52 degree tilted view (bottom) SEM images of MacEtched dot arrays in a solution of 0.56 M HF, 0.26 M H_2O_2, 0.88 M DI, 0.21 M IPA ($\rho_{H_2O_2}$ = 0.32) for 15 minutes with the diameter of (a) 600 nm, (b) 500 nm, (c) 400 nm, (d) 300 nm, (e) 200 nm, (f) 100 nm, at fixed spacing of 100 nm.

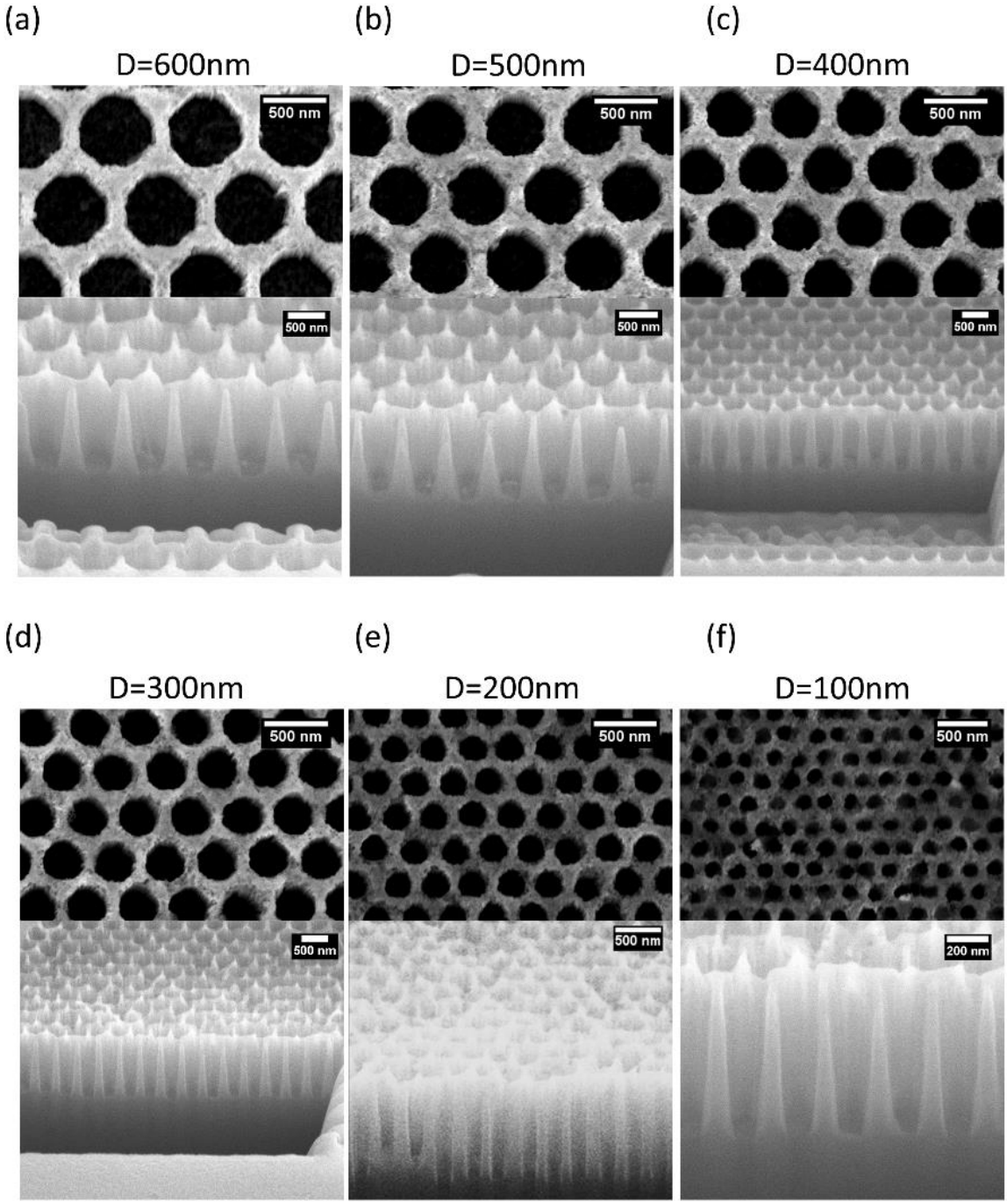

Figure 2.18: Top view (top) and 52 degree tilted view (bottom) SEM images of MacEtched dot arrays in a solution 0.56 M HF, 0.52 M H_2O_2, 0.88 M DI, 0.21 M IPA ($\rho_{H_2O_2}$ = 0.48) for 10 minutes with the diameter of (a) 600 nm, (b) 500 nm, (c) 400 nm, (d) 300 nm, (e) 200 nm, (f) 100 nm, at fixed spacing of 100 nm.

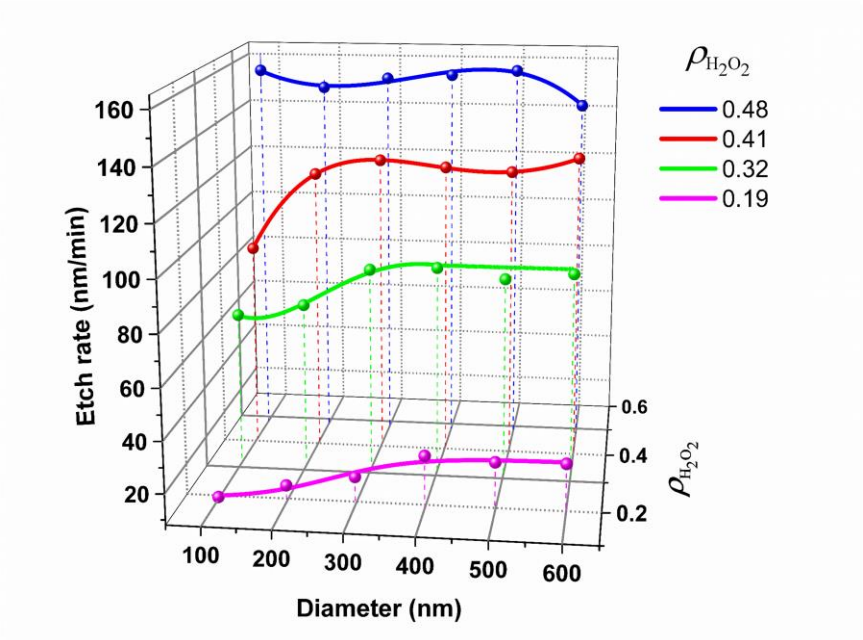

Figure 2.19: Vertical etch rate plotted as a function of diameter from 100 nm to 600 nm at fixed spacing of 100 nm, MacEtched at $\rho_{H_2O_2}$ of 0.19, 0.32, 0.41 and 0.48.

Figure 2.19 shows the measured vertical etch rate as the function of diameter from 100 nm to 600 nm at fixed spacing of 100 nm, MacEtched at $\rho_{H_2O_2}$ of 0.19, 0.32, 0.41 and 0.48. For the 0.19 $\rho_{H_2O_2}$, the etch rate increases from 10 nm/min to 30 nm/min as the diameter increases from 100 nm to 400 nm. The etch rate stays as the constant value of 30 nm/min as the diameter increases from 400 nm to 600 nm. The diameter where the etch rate starts to saturate (400 nm at 0.19 $\rho_{H_2O_2}$) is defined as the critical diameter D_C. As the $\rho_{H_2O_2}$ increases from 0.19 to 0.48, the etch rate in every diameter increases. The D_C shifts from 400 nm to 100 nm such that at 0.48 $\rho_{H_2O_2}$, the etch rate is completely saturated.

The increasing etch rate with increasing diameter from 100 nm to 400 nm is due to the limited-CG. As described in the diameter study shown in Figure 2.8, the rate of hole injection is less than the rate of the oxidized Si removal. The etch rate increases with increasing diameter due to the increased CG by increase in catalyst volume and the hole concentration overlapping.

The saturation of the etch rate for diameter larger than 400 nm is due to the balance of CG and MT. The etch rate increased by the enhanced-CG is balanced with the etch rate decrease by the limited-MT.

The shifting of D_C from 400 nm to 100 nm with increased $\rho_{H_2O_2}$ is due to the increased hole injection rate. The hole injection rate increases with increasing H_2O_2 concentration such that the limited-CG below D_C becomes balanced with MT.

2.6 Empirical Vertical Etch Rate Model

The hole concentration model using the 2D constant-source diffusion process is reported by Lianto et al. [11] in 2012. They described the catalyst deformation or detouring with the uneven hole concentration under the catalyst. However, there is still no modeling data which uses both CG and MT to estimate the vertical etch rate. In this section, the empirical vertical etch rate model is constructed to simulate the simultaneous influence of MT and CG on vertical etch rate respect to the array dimension and H_2O_2 concentration. The master code can be found in Appendix A.

First, the measured average vertical etch rate as the function of catalyst diameter at 1 μm pitch shown in Figure 2.8 is converted to etch rate as a function of the array spacing (*S*). Then, the curves are fitted with the second-order polynomial such that vertical etch rate, *R* is described as

$$R = a + bS - cS^2 \tag{2.3}$$

where *b* and *c* are first and second polynomial coefficients, and *a* is the intercept. It is important to note that only $R_{MacEtch} > 0$ is valid since a negative etch rate is invalid. Because *S* = *P*-*D*, equation (3.3) can be rewritten in terms of *P* and *D* as

$$R = a + b(P - D) - c(P - D)^2 \tag{2.4}$$

where *a*, *b*, and *c* for $\rho_{H_2O_2}$ of 0.19, 0.32, 0.41 and 0.48 are extracted from the fitting and corresponding values are shown in Table 2.1.

Table 2.1: Extracted *a*, *b* and *c* from the second polynomial fitting.

	a	***b***	***c***
0.19	40.78	108.71	320.72
0.32	74.08	214.98	319.58
0.41	87.30	310.39	418.69
0.48	95.79	348.27	388.60

Extracted *a* and *b* are fitted by a second-order polynomial function and *c* is fitted by a Gaussian function.

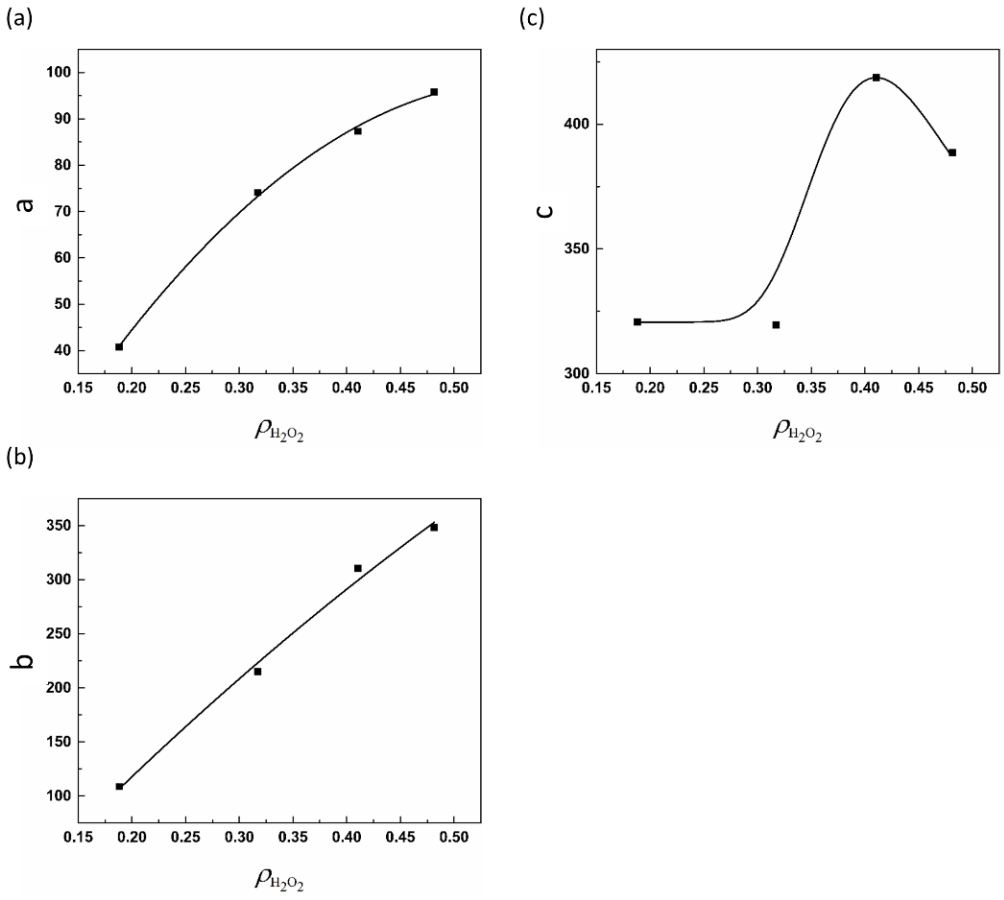

Figure 2.20: Shown are (a)*a*, (b)*b*, and (c)*c* as a function of the $\rho_{H_2O_2}$. Symbols and lines represents the experimental and fitted data respectively.

Figure 2.20 shows the fitted *a*, *b* and *c* parameter curves. The fitted equations of *a*, *b* and *c* are described as shown in equations (2.5) - (2.7).

$$a = -30 + 465.7\rho_{H_2O_2} - 397.5\rho_{H_2O_2}^2 \tag{2.5}$$

$$\mathrm{b} = -86.6 + 1099.1\rho_{H_2O_2} - 386.6\rho_{H_2O_2}^2 \tag{2.6}$$

$$\mathrm{c} = 320.72 + 97.97 * \exp(-\exp(-\mathrm{z}) - \mathrm{z} + 1) \quad ; z = \frac{\rho_{H_2O_2} - 0.41}{0.07} \tag{2.7}$$

Equation (2.4) can be simplified in terms of the vertical etch rate decreased by MT and the vertical etch rate increased by CG as shown in equation (2.8),

$$R = a + R_{MT} + R_{CG} \tag{2.8}$$

where R_{MT} = $-bD-cD^2$ and R_{CG} = $bP-cP^2+2cDP$. R_{MT} and R_{CG} indicate the etch rate decreased by the MT and increased by the CG, respectively. It is important to note that R_{MT} and R_{CG} have a series relationship and this can be derived from the *R* that is described as

$$R = (CG_{Total})\ (MT_{Net}) \tag{2.9}$$

where CG_{Total} is the effective hole concentration that contributes to MacEtch and MT_{Net} is the mass transport of reactants and byproducts. CG_{Total} and MT_{Net} are described as

$$(CG_{Total})^{-1} = (hole\_generation)^{-1} + (hole\_injection)^{-1} + (hole\_diffusion)^{-1} \tag{2.10}$$

$$(MT_{Net})^{-1} = (diffusion\ of\ reactants\ to\ the\ reaction\ site)^{-1} + (diffusion\ of\ products\ away\ from\ the\ reaction\ site)^{-1} \tag{2.11}$$

Since the mass transport (MT_{Net}) is the competing reactions of maximum rate of reactants and byproducts that can be transported (MT_{Max}) and the rate of reactants and byproducts that are limited by the limited mass transport ($MT_{Limited}$), MT_{Net} also can be described as

$$MT_{Net} = MT_{Max} - MT_{Limited} \tag{2.12}$$

where MT_{Max} and $MT_{Limited}$ are described as

$$(MT_{Max})^{-1} = (Maximum\ diffusion\ of\ reactants\ to\ the\ reaction\ site)^{-1}$$

$$+ (\textit{Maximum diffusion of products away from the reaction site})^{-1} \quad (2.13)$$

$$(MT_{Limited})^{-1} = (\textit{Limited diffusion of reactants to the reaction site})^{-1}$$

$$+ (\textit{Limited diffusion of products away from the reaction site})^{-1} \quad (2.14)$$

By using equation (2.12), equation (2.9) can be rewritten as

$$R = (CG_{Total})(MT_{Max} - MT_{Limited}) \quad (2.15)$$

From equation (2.15), we can divide into two components that are

$$R_{CG} = (CG_{Total})(MT_{Max}) \quad (2.16)$$

$$R_{MT} = (CG_{Total})(MT_{Limited}) \quad (2.17)$$

where R_{CG} indicates the maximum vertical etch rate the MacEtch can take with a given hole concentration and R_{MT} indicates the etch rate decreased by the limited mass transport. As a result, R_{MT} and R_{CG} in equation (2.8) are still in series relationship.

Equation (2.8) can be further simplified by setting the $\rho_{H_2O_2}$ to extreme values. Since $0 < \rho_{H_2O_2} < 1$, the lowest and the highest $\rho_{H_2O_2}$ values are defined as 0.1 and 0.9, respectively, and the calculated *a*, *b* and *c* are shown in Table 2.2.

Table 2.2: Etch rate model parameters and relationships at high and low ends of ρ_{H2O2}.

ρ_{H2O2}	*a*	*b*	*C*	***P* = 1 μm**			***D* = 1 μm**		
				R_{MT}	R_{CG}	*R*	R_{MT}	R_{CG}	*R*
0.1	11.2	19.5	320.7	$-19.5D-320.7D^2$	$-301.2+641D$	$-290+621.5D-320.9D^2$	-340.2	$660.5P-320.7P^2$	$-340.2+660.5P-320.7P^2$
0.9	54.5	589.5	320.9	$-589.5D-320.9D^2$	$286.6+641D$	$-290+621.5D-320.9D^2$	-910.4	$1230.5P-320.7P^2$	$-910.4+1230.5P-320.7P^2$

Assume that the pitch is 1 μm, then R_{MT} and R_{CG} are

$$R_{MT} = -bD - cD^2 \quad (2.18)$$

$$R_{CG} = b - c + 2cD \quad (2.19)$$

When $\rho_{H_2O_2}$ is 0.1, equation (2.8) can be written as

$$R = -290 + 621.5D - 320.7D^2 \quad (2.20)$$

Since $D < 1$ μm, the $R_{MacEtch}$ is governed by the D term in R_{CG}, thus,

$$R \propto D \quad (2.21)$$

When $\rho_{H_2O_2}$ is 0.9, equation (2.8) can be written as

$$R = 341.1 + 51.5D - 320.9D^2 \quad (2.22)$$

where $R_{MacEtch}$ is governed by $-D^2$ term in R_{MT}, thus,

$$R \propto -D^2 \quad (2.23)$$

Now assume that the diameter is 1 μm, then, equation (2.4) can be simplified as

$$R_{MT} = -b - c \quad (2.24)$$

$$R_{CG} = bP - cP^2 + 2cP \quad (2.25)$$

When $\rho_{H_2O_2}$ is 0.1, equation (2.8) can be written as

$$R = -340.2 + 660.5P - 320.7P^2 \quad (2.26)$$

where $R_{MacEtch}$ is governed by $-P^2$ term in R_{CG}, thus,

$$R \propto -P^2 \quad (2.27)$$

When $\rho_{H_2O_2}$ is 0.9, equation (2.8) can be written as

$$R = -910.4 + 1230.5P - 320.7P^2 \quad (2.28)$$

where $R_{MacEtch}$ is hyperbolic. The pitch where the maximum $R_{MacEtch}$ (P_m) can be calculated by differentiating equation (2.8) in terms of P, and setting it to 0.

$$\frac{\partial(R)}{\partial P} = (b + 2c) - 2cP = 0 \quad (2.29)$$

Then, the P_m that occurs can be described as

$$P_m = \frac{(b+2c)}{2c} \quad (2.30)$$

Thus, for $P < P_m$ (MT dominated from increased packing density),

$$R \propto P \tag{2.31}$$

for $P > P_m$, (CG dominated from hole concentration overlap),

$$R \propto -P^2 \tag{2.32}$$

The relationship of R_{MT} and R_{CG} at fixed spacing shown in Figure 2.19 can be analytically described. The R_{MT} and R_{CG} with increasing D and P can be described as

$$R_{MT} = -b(D_0 + D_1) - c(D_0 + D_1)^2 \tag{2.33}$$

$$R_{CG} = b(P_0 + P_1) - c(P_0 + P_1)^2 + 2c(D_0 + D_1)(P_0 + P_1) \tag{2.34}$$

where D_0 and P_0 are the initial value of the D and P, and D_1 and P_1 are the change in D and P. The etch rate resulting by increasing D_1 and P_1 (ΔR_{MT}, ΔR_{CG}) can be described as

$$\Delta R_{MT} = -bD_1 - cD_1{}^2 \tag{2.35}$$

$$\Delta R_{CG} = bP_1 - cP_1{}^2 + 2cD_1P_1 \tag{2.36}$$

when the spacing is fixed, $D_1 = P_1$, thus, ΔR_{CG} can be simplified as

$$\Delta R_{CG} = bD_1 + cD_1{}^2 = -\Delta R_{MT} \tag{2.37}$$

which indicates that the etch rate increased by CG (ΔR_{CG}) balances out by the etch rate decreased by MT(ΔR_{MT}), thus, the etch rate stays constant when the spacing is fixed.

Figure 2.21 shows the simulated etch rate as a function of diameter from 100 nm to 900 nm at fixed 1 µm pitch with $\rho_{H_2O_2}$ from 0.1 to 0.9. For the ratio of 0.1, the etch rate stays 0 nm/min as the diameter increases from 100 nm to 785 nm. Then, the etch rate increases to 10 nm/min as the diameter increases from 840 nm to 900 nm. As $\rho_{H_2O_2}$ increases to 0.2, the diameter where the etch rate starts to increase (threshold diameter, D_{th}) shifts to 400 nm. The parabolic etch rate trends start to appear from the concentration ratio of 0.2. The diameter where the highest etch rate, D_M, decreases from 700 nm to 100 nm as the ρ_{H2O2} increases from 0.2 to 0.9. At 0.9, the maximum

ratio at this condition, the parabolic trend is no longer observed and the etch rate only decreases with increasing diameter.

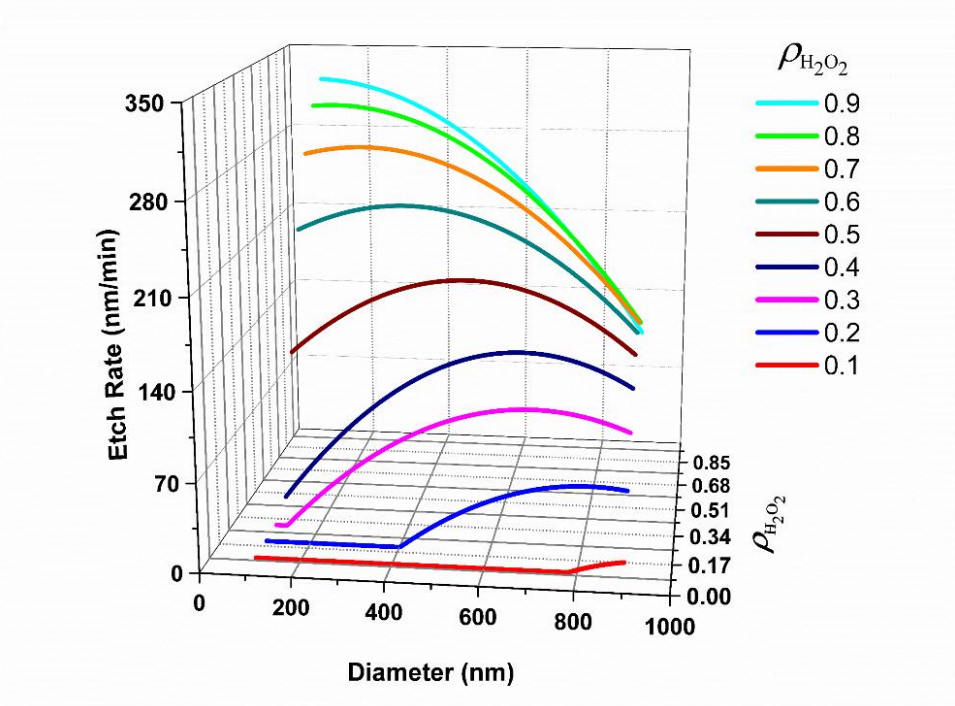

Figure 2.21: Simulated vertical etch rate as the function of diameter from 100 nm to 900 nm at fixed pitch of 1 μm for $\rho_{H_2O_2}$ from 0.1 to 0.9.

The increase in etch rate with increasing diameter at the ρ_{H2O2} values from 0.1 to 0.2 is due to the dominance of the CG process as discussed with regard to Figure 2.8. The decrease in D_{th} with increasing $\rho_{H_2O_2}$ indicates that the onset of vertical etching shifts with a diameter-dependent critical hole concentration. The parabolic etch rate trends shown for $\rho_{H_2O_2}$ values between 0.2 to 0.8 are again attributed to the competing process between CG and MT. A decrease in D_C with increasing concentration ratio indicates that the etch rate is more MT-limited as the ratio increases. The increase in etch rate with a decreasing diameter at the ratio of 0.9 shows that the etch rate is completely dominated by the MT process.

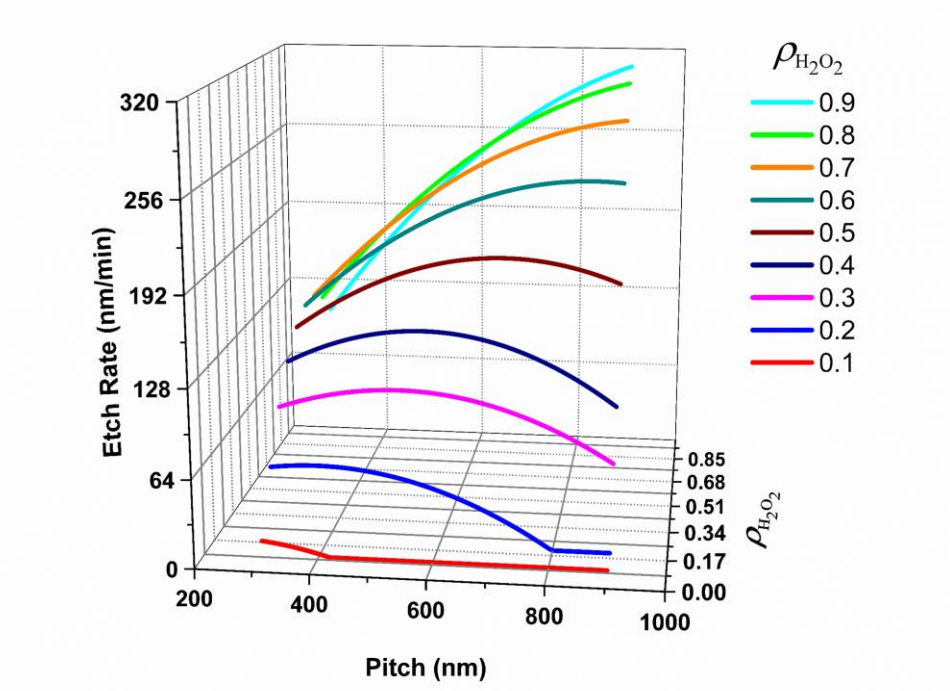

Figure 2.22: Simulated vertical etch rate as the function of the pitch from 300 nm to 900 nm at fixed diameter of 200 nm for $\rho_{H_2O_2}$ from 0.1 to 0.9.

Figure 2.22 shows the simulated vertical etch rate as a function of pitch from 300 nm to 900 nm at fixed diameter of 200 nm for $\rho_{H_2O_2}$ values from 0.1 to 0.9. At 0.1, the etch rate stays 0 nm/min as the pitch decreases from 900 nm to 420 nm. Then, the etch rate starts to increase to 10 nm/min when the pitch decreases to 300 nm. As the concentration ratio increases to 0.2, the pitch where etch rate starts to increase (threshold pitch, P_{th}) shifts to 800 nm. The parabolic etch rate trend starts to appear as the ratio increases higher than 0.2. The highest etch rate pitch, P_C increases from 300 nm to 900 nm as the ratio increases from 0.2 to 0.7. At above 0.7, the maximum ρ_{H2O2} at this condition, the etch rate only decreases with decreasing pitch.

The increase in etch rate with decreasing pitch at the $\rho_{H_2O_2}$ ratio from 0.1 to 0.2 is due to the hole concentration overlap as discussed in Figure 2.13. The notable increase in threshold pitch with increased ρ_{H2O2} is attributed to the formation of wider hole distributions due to an increase in the hole injection rate, which causes an overlap of adjacent distributions to occur at larger pitch

values that would otherwise be absent at lower $\rho_{H_2O_2}$ ratios. The parabolic etch rate trends shown in the concentration ratio from 0.3 to 0.7 are due to the competing processes of CG and MT. As $\rho_{H_2O_2}$ increases, hole concentrations under the catalyst are sufficiently high such that the etch rate is mainly limited by the MT process, and this is also shown by the increase in P_M with an increasing ρ_{H2O2} ratio. As previously noted, the decrease in etch rate below P_M at smaller pitch values indicates that higher packing densities force a reduction in MT due to the sharing of HF. At $\rho_{H_2O_2}$ above 0.7, the absence of P_M indicates that the etch rate is completely dominated by the MT process.

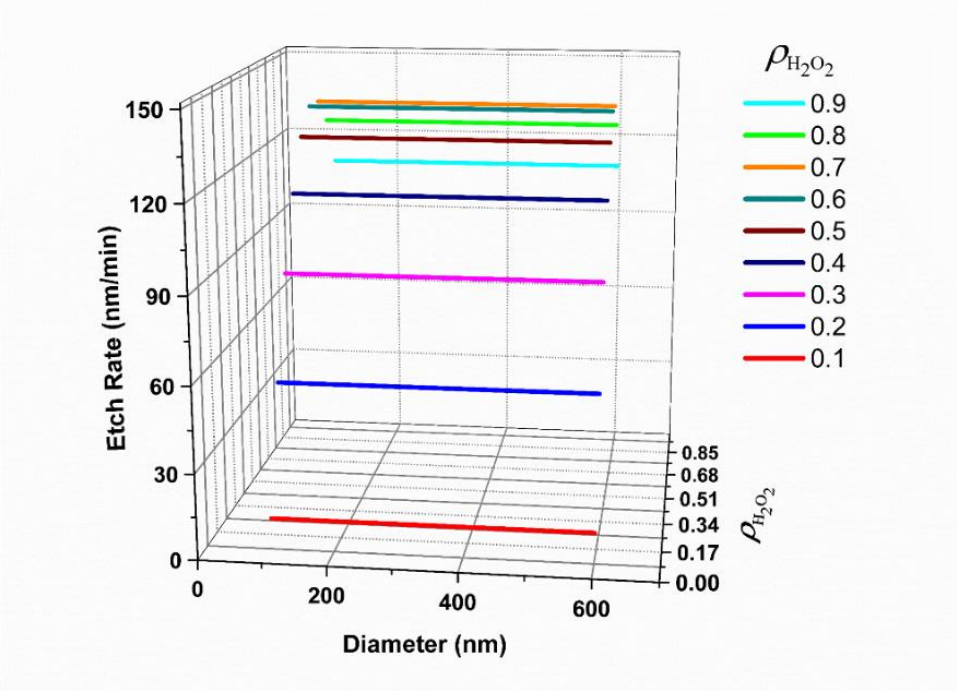

Figure 2.23: Simulated vertical etch rate as the function of the diameter from 100 nm to 600 nm at fixed spacing of 100 nm for $\rho_{H_2O_2}$ from 0.1 to 0.9.

Figure 2.23 shows the simulated vertical etch rate as function of diameter from 100 nm to 600 nm at a fixed spacing of 100 nm with $\rho_{H_2O_2}$ from 0.1 to 0.9. A constant etch rate over the entire diameter range from 100 nm to 900 nm is observed for every concentration ratio. The etch rate gradually increases as the ρ_{H2O2} ratio increases and saturates as the ratio reaches 0.7, then the etch

rate starts to decrease as the ratio increases from 0.7 to 0.9. The constant etch rate over every diameter is attributed to the balance between the CG and MT processes. In contrast to the experimental result shown Figure 2.19, the simulated data does not show the decrease in etch rate at a small diameter for low $\rho_{H_2O_2}$. This is because the threshold diameter of etching at equal spacing is not included in the empirical model. The saturation of the etch rate with $\rho_{H_2O_2}$ from 0.1 to 0.7 and the decrease in etch rate with ρ_{H2O2} from 0.7 to 0.9 are due to the greater CG over MT.

2.7 Fabrication of High Aspect Ratio Sub-Micron Scale Silicon Via Array

Based on the experimental data and empirical etch rate simulation data analysis, the high aspect ratio sub-micron scale Si via array is designed and fabricated by MacEtch.

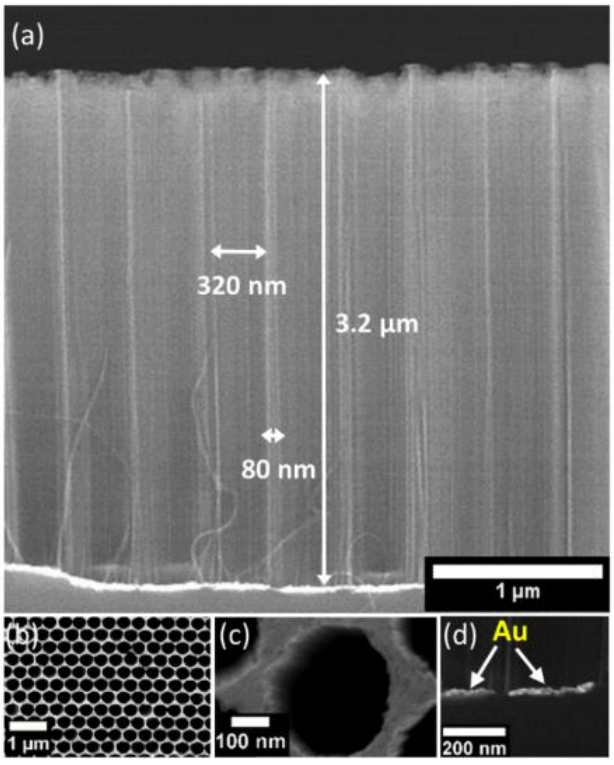

Figure 2.24: (a) Cross-sectional SEM image of the MacEtched via array with 320 nm diameter and 400 nm pitch showing the vertical sidewall with etch depth of 3.2 µm and spacing of 80 nm, (b) low magnification top view SEM image of the etched via array, (c) high magnification top view SEM image of the single via, and (d) SEM image of the Au catalyst at the bottom of the etched via array.

Figure 2.24 (a) shows the cross-sectional SEM image of the MacEtched via array with 320 nm diameter and 400 nm pitch. Catalyst array etched down to 3.2 μm with the absence of catalyst detouring or delamination keeping the constant spacing of 80 nm. Note the sidewall surface grooves are produced from the Au catalyst morphology. The grooves can be seen in the low- and high-magnification top view SEM of the MacEtched via array shown in Figure 2.24 (b) and (c). The Au catalysts at the bottom of the etched via can be seen in both Figure 2.24 (a) and (d).

3. FABRICATION OF POLYCRYSTALLINE SILICON VIA ARRAY BY SELF-ANCHORED CATALYST MACETCH

MacEtch of high aspect ratio (HAR) structures specifically in sub-micron scale via array on polycrystalline silicon (Poly-Si) substrate is challenging due to the catalyst delamination and detour resulted by the uneven etch rate originated from the non-uniform carrier generation (CG) and mass transport (MT) of the poly grains. In this chapter, the sub-micron scale highly ordered Poly-Si via array by self-anchored catalyst (SAC) MacEtch which uses the porous discrete catalyst array is presented. By using the porous catalyst, nanowire (NW) formed through the pinholes physically anchor the catalyst from delamination and detour. The systematical vertical etch rate study as the function of catalyst diameter increasing from 200 nm to 900 nm at a fixed pitch of 1 μm shows the SAC-MacEtch not only confines the etching direction normal to substrate but also enhances the etch rate by the increased liquid access path. With this MT engineering, via array is fabricated on poly/SiO_2 stacks through the alternating etching process of Poly-Si SAC-MacEtch and SiO_2 chemical etching which can be used in the 2.5D/3D photonic and electronic device applications.

3.1 Fabrication Process

The substrate consists of 2 μm low-pressured chemical vapor deposition (LPCVD) grown polysilicon on oxide deposited on boron doped p-type (100)-oriented crystalline Si with resistivity of 1-50 Ω-cm. Prior to any process, the substrate was subjected to the cleaning processes; organic contaminants removal in 1:1:5 NH_4OH:H_2O_2:DI water at 80˚C, native oxide stripe in 1:10 BOE, and ionic contaminant removal in 1:1 HCl:DI water. After the cleaning process, an electron lithography resist of 950 k PMMA in 2 percent anisole was spin-coated at 2500 rpm for 30 seconds to deposit 80 nm resist film on the substrate. Then, an electron beam (e-beam) lithography with a

10 KV beam voltage, and 20 µm aperture was used for exposure of sub-micron dot array patterns. The exposed patterns were developed in 1:3 MIBK: IPA for 2 minutes at room temperature. The PMMA residue and native oxide in the exposed patterns were etched in 1:1 HCL: DI water for 1 min and 1:10 BOE for 2 min, respectively. Then, porous Au and nonporous Au films were deposited using CHA SEC-600 e-beam evaporator. Next, the Au film on the PMMA was lifted off in Remover PG for 30 min at 60 °C and rinsed with four cycles in IPA for 30 s.

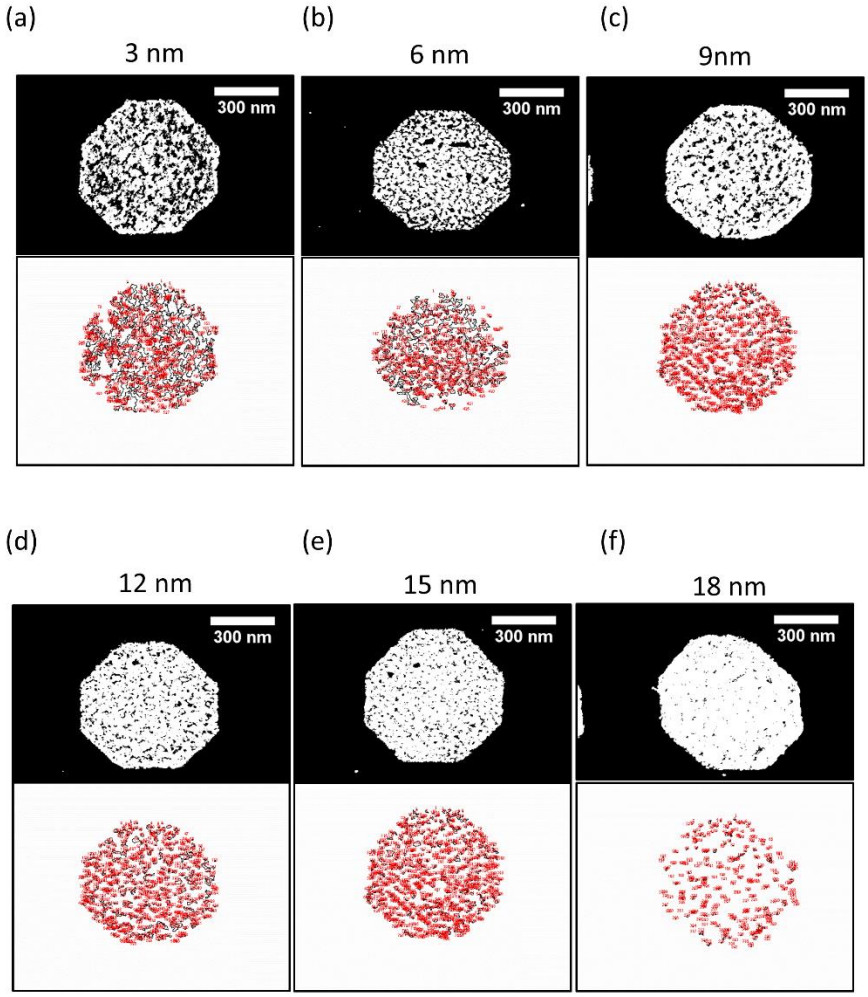

Figure 3.1: High contrast SEM images and particle analysis mapping images of the porous catalyst film with deposition thickness of (a) 3 nm, (b) 6 nm, (c) 9 nm, (d) 12 nm, (e) 15 nm, and (f) 18 nm at fixed deposition rate of 0.7 Å/s and fixed deposition pressure of ~$3x10^{-6}$ Torr.

The pinhole size of the porous film was controlled by Au deposition rate and thickness. The pinhole size as the function of the deposition thickness from 3 nm to 18 nm is at a fixed deposition rate of 0.7 Å/s and fixed deposition pressure of ~3x10^{-6} Torr was calibrated on the c-Si substrate. Top view SEM images of the 600 nm diameter catalyst for different Au thicknesses were taken at same magnification of 100 K. Then, using the particle analysis, the average pore size and the pore coverage were analyzed. Figure 3.1 shows the sets of the high contrast SEM images used for the particle analysis and the particle analysis mapping images.

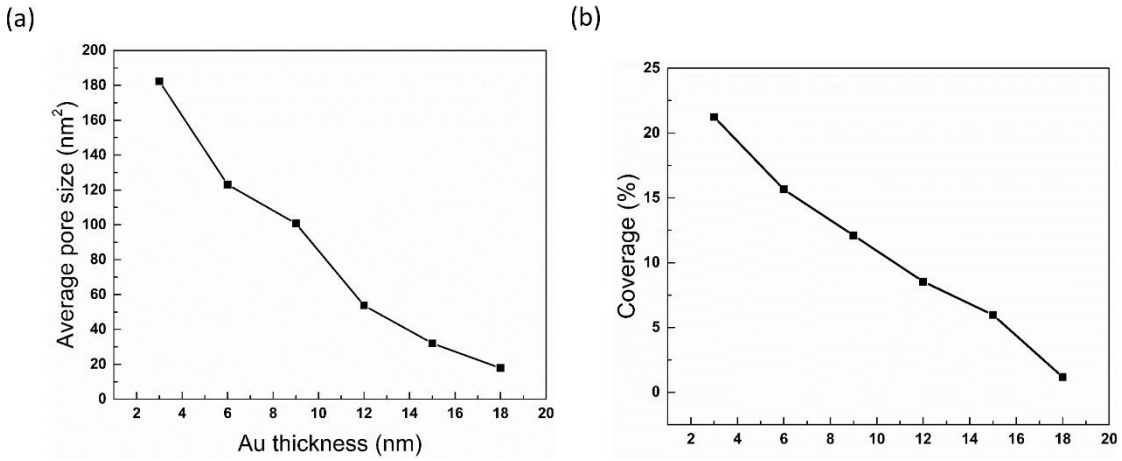

Figure 3.2: (a) Average pore size and (b) pore coverage as the function of Au deposition thickness from 3 nm to 18 nm at fixed deposition rate of 0.7 Å/s and fixed deposition pressure of ~3x10^{-6} Torr.

Figure 3.2 (a) and (b) show the average pore size and the pore coverage as the function of Au deposition thickness from 3 nm to 18 nm with step size of 3 nm at fixed deposition rate of 0.7 Å/s and fixed deposition pressure of ~3x10^{-6} Torr. The average pore size decreases from 180 nm^2 to 20 nm^2 and the pore coverage decreases from 20 % to 1 % as the deposition thickness increases from 3 nm to 18 nm. Both samples with porous and nonporous Au were MacEtched in the solution of 49 % HF (0.56 M), 30 % H_2O_2 (0.13 M, 0.26 M), IPA (0.21 M) and DI (0.88 M). Again, the HF to H_2O_2 ratio defined as $\rho_{H_2O_2}$ in equation (3.1) is used for the etch rate analysis ($\rho_{H_2O_2}$ = 0.19, 0.32).

The top view of the etched samples was inspected with a Hitachi S-4800 scanning electron microscope (SEM), and the cross-section of the etched samples was inspected with FEI DB 235 dual-beam focused ion beam (FIB) system at the same condition as described in Chapter 2.

3.2 Influence of Polycrystalline Grains and Grain Boundaries

Figure 3.3 (a) shows the top view SEM image of nonporous Au catalyst array with 700 nm diameter MacEtched in 0.32 $\rho_{H_2O_2}$ for 10 minutes.

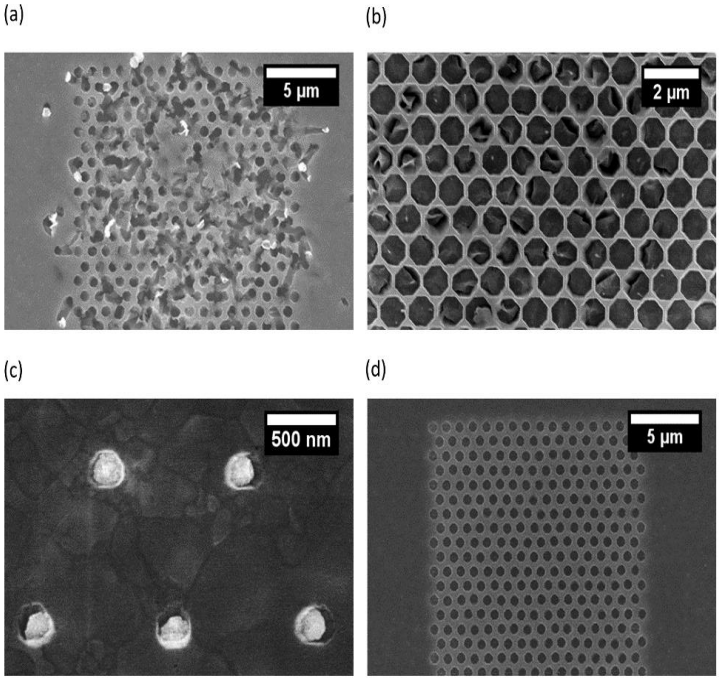

Figure 3.3 Top view SEM images of (a) nonporous Au catalyst array with 700 nm diameter and 1 µm pitch, MacEtched in 0.32 $\rho_{H_2O_2}$ for 10 minutes, (b) nonporous Au catalyst array with 700 nm diameter and 1 µm pitch, MacEtched in 0.1 $\rho_{H_2O_2}$ for 10 minutes, (c) nonporous Au catalyst array with 200 nm diameter and 1 µm pitch, MacEtched in 0.1 $\rho_{H_2O_2}$ for 10 minutes, and (d) porous Au catalyst array of 700 nm diameter and 1 µm pitch, MacEtched in 0.32 $\rho_{H_2O_2}$ for 10 minutes.

The discrete catalysts are delaminated or detoured. The delamination of the catalyst is attributed to the excessive H_2 generation in between catalyst and substrate [11]; the van der Waals'

force between the catalyst and the substrate is weaker than the upward force induced by the H_2 such that H_2 pushes the catalyst upward instead of escaping through the catalyst edge.

Catalyst detouring can be attributed to (i) catalyst motion resulted by H_2 trap [11] and (ii) limited mass transport [12]; etch rate is non-uniform under the catalyst due to the limited liquid access.

Figure 3.3 (b) shows the top view SEM image of nonporous Au catalyst array with the diameter of 700 nm at pitch of 1 μm, MacEtched in 0.1 $\rho_{H_2O_2}$. At a low H_2O_2 concentration, the catalyst delamination is minimized but the catalyst deformation within every etched via is observed. This is attributed to the uneven MT and CG originated from the Poly-Si. The grains in Poly-Si contain the crystallites with different crystal orientations. When the catalyst overlaps with more than one grain, the etch rate under the catalyst becomes non-uniform; etching is faster in <100> direction such that the catalyst deforms to the direction of the grain where the etch rate is the fastest. The crystal orientation-dependent MacEtch of NW array at low of HF to H_2O_2 ratio and mesh pattern with small spacing have been previously reported. Chern et al. demonstrated MacEtch of Si NW array using the Ag mesh patterned catalyst on (100), (110), (111) Si substrate as a function of the HF to H_2O_2 ratio [23]. They observed that at high oxidant concentration, the etching is preferred to <100> direction due to the limited amount of the HF, and the etching direction changes to <110> and <111> at low oxidant concentration. Chang et al. demonstrated the MacEtch of the Si NW array using the Au mesh patterned catalyst on (100), (110), (111) Si substrates with varied mesh dimension [24]. They observed that the etching with mesh catalyst with small spacing and the discrete island Au catalyst formed by depositing 3 nm Au are crystal-orientation dependent; etching is preferred to <100> direction.

The non-uniform etching under the catalyst becomes more evident as the catalyst diameter decreases. Figure 3.3 (c) shows the top view SEM image of nonporous Au catalyst array of 200 nm diameter at 1 μm pitch MacEtched in the same etching condition as shown in Figure 3.3 (b). As the catalyst diameter decreases, catalyst deformation is reduced but the catalyst detouring to random directions is observed. This is attributed to the change in catalyst direction resulted from the etching dominated by the one grain. The catalyst detouring to random directions in poly-Si is consistent with the results presented by Chang et al.

In order to confine the etching direction normal to the substrate, porous catalyst is deposited by controlling the thickness and deposition rate instead of depositing the non-porous catalyst. The porous Au can be deposited at intermediate deposition condition of the discrete island and nonporous film. The average pinhole size increases as the deposition thickness decreases or the deposition rate increases. The average pinhole size as function of the Au film thickness and deposition rate on c-Si substrate is calibrated as shown in Figure 3.2. Figure 3.3 (d) shows the top view SEM image of porous Au catalyst array of 700 nm at 1 μm pitch MacEtched at same condition as shown in Figure 3.3 (a) (0.32 $\rho_{H_2O_2}$). The catalyst delamination resulted by the excessive H_2 generation and the deformation and detouring resulted by the uneven etch rate under the catalyst are significantly reduced as compared to the nonporous catalyst. This method of confining the catalyst is defined as self-anchored catalyst (SAC) MacEtch. The detailed mechanisms and the etching characteristics are discussed in the following sections.

3.3 Self-Anchored Catalyst (SAC) MacEtch

The mechanism of the catalyst anchoring and the etching direction confinement in porous catalyst is investigated by etching the sample for short duration. Figure 3.4 (a) shows the top view

SEM image of the porous catalyst array before MacEtch. The subset image shows the high magnification image of single catalyst deposited on the multi-poly g rains. Figure 3.4 (b) shows the SEM image of the 700 nm diameter catalyst with porous Au MacEtched in 0.32 $\rho_{H_2O_2}$ for 2 minutes. The sub 20 nm diameter NWs are formed through the pinholes in the porous Au. This makes the catalyst similar to the mesh pattern catalyst with smaller mesh area. During the MacEtch, NWs formed though the pinholes anchor the catalyst from the catalyst delamination and deformation. Figure 3.4 (c) shows the array of 700 nm diameter porous catalyst with sub 20 nm pinholes MacEtched in 0.32 $\rho_{H_2O_2}$ for 10 minutes. With the longer duration etching, the NWs are chemically polished away by the diffusion of the unconsumed holes.

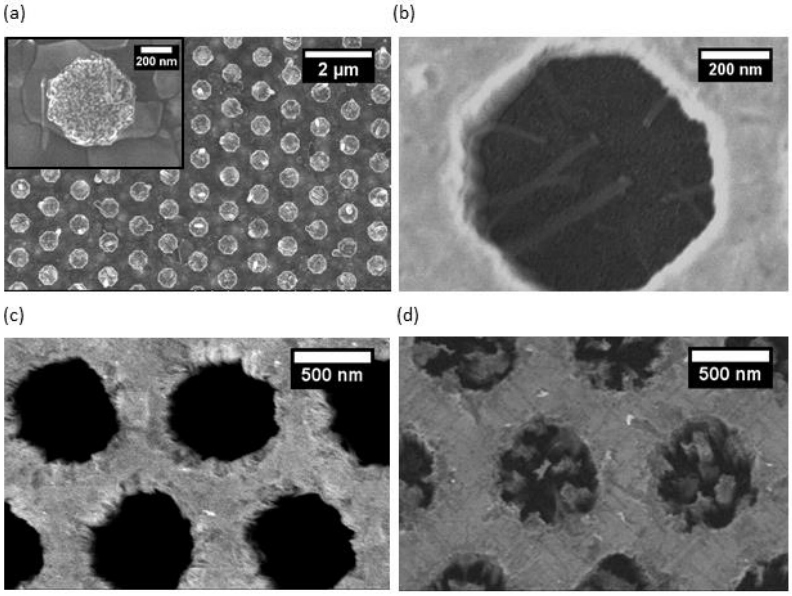

Figure 3.4: Top view SEM image of (a) porous catalyst before MacEtch where subset image shows the high magnification image of the single catalyst deposited on the multi-poly grains, (b) initial stage of MacEtch showing the formation of sub 20 nm nanowires through the porous catalyst pinholes, (d) vias showing the sub 100 nm nws were chemically etched at long time etching, and (e) vias showing the sub 100 nm nanowires are remaining with long time etching.

Figure 3.4 (d) shows the array of the 500 nm diameter porous catalyst with pinhole size of sub 100 nm MacEtched in same condition as shown in Figure 3.4 (c). In this case, the NWs formed

though the pinholes are clearly shown from the top view. This is because only the surface of NWs is chemically polished from the diffusion of the unconsumed holes.

In contrast to the etching direction confinement in mesh catalyst reported by Chang et al. , crystal-orientation dependent etching in larger pinholes (i.e. smaller spacing) was not observed. This indicates that the directional confinement is not only affected by the spacing between pores but also affected by the effective area of the mesh catalyst.

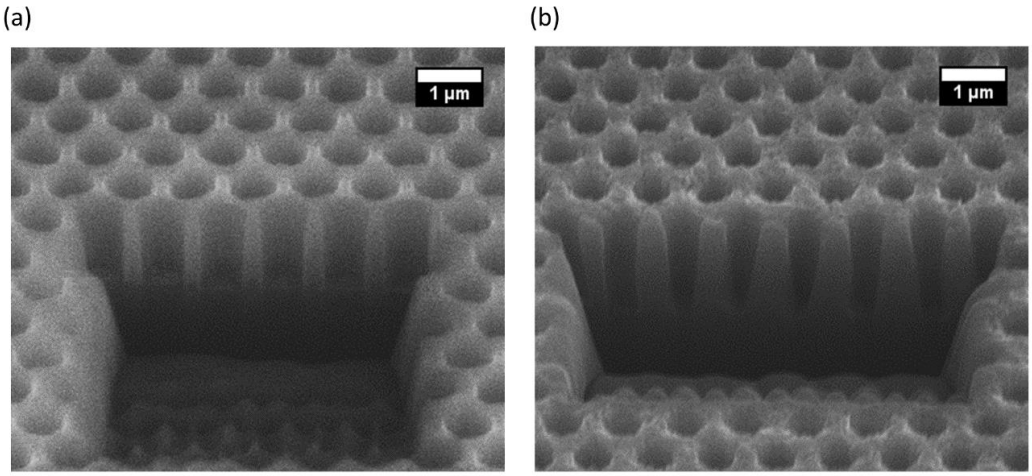

Figure 3.5: A 52 degree tilted cross-section SEM images after FIB showing array of Poly-Si via array fabricated with porous Au catalyst array of (a) 800 nm diameter with pitch of 1 µm, SAC-MacEtched in 0.32 $\rho_{H_2O_2}$ for 10 min, and (b) 600 nm diameter with pitch of 1 µm SAC-MacEtched in 0.19 $\rho_{H_2O_2}$ for 10 min.

Figure 3.5 (a) show the 52 degree tilted cross-sectional SEM images of the 800 nm diameter with pitch of 1 µm, SAC-MacEtched in 0.32 $\rho_{H_2O_2}$ for 10 min, and Figure 3.5 (b) shows the 600 nm diameter with pitch of 1 µm, SAC-MacEtched in 0.19 $\rho_{H_2O_2}$ for 10 min. Images clearly show both 800- and 600-nm diameter catalyst arrays are vertically etched down without catalyst detouring or delamination. It also shows that the NWs formed through the pinholes were chemically polished away during the etching process.

3.4 Influence of Catalyst Diameter on Poly-Si Via MacEtch

Figure 3.6 to Figure 3.7 show the set of top and 52 degree tilted SEM images of the Poly-Si via array with the varied diameter from 100 nm to 900 nm at fixed pitch of 1 µm that were SAC-MacEtched with 0.19, 0.32 $\boldsymbol{\rho_{H_2O_2}}$ respectively.

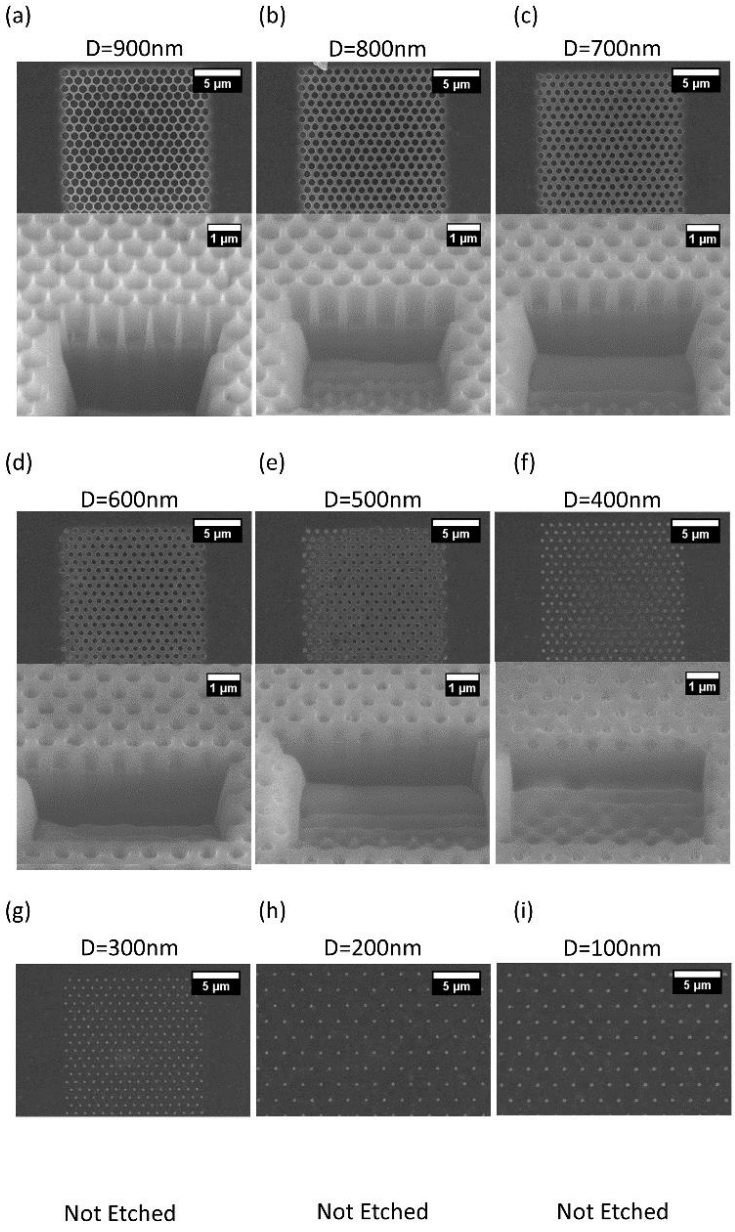

Figure 3.6: Top view (top) and 52 degree tilted view (bottom) SEM images of SAC-MacEtched dot arrays in a solution of 0.56 M HF, 0.13 M H_2O_2, 0.88 M DI, 0.21 M IPA ($\rho_{H_2O_2}$ = 0.19) for 10 minutes with the diameter of (a) 900 nm, (b) 800 nm, (c) 700 nm, (d) 600 nm, (e) 500 nm, (f) 400 nm, (g) 300 nm, (h) 200 nm, and (i) 100 nm at fixed pitch of 1 µm.

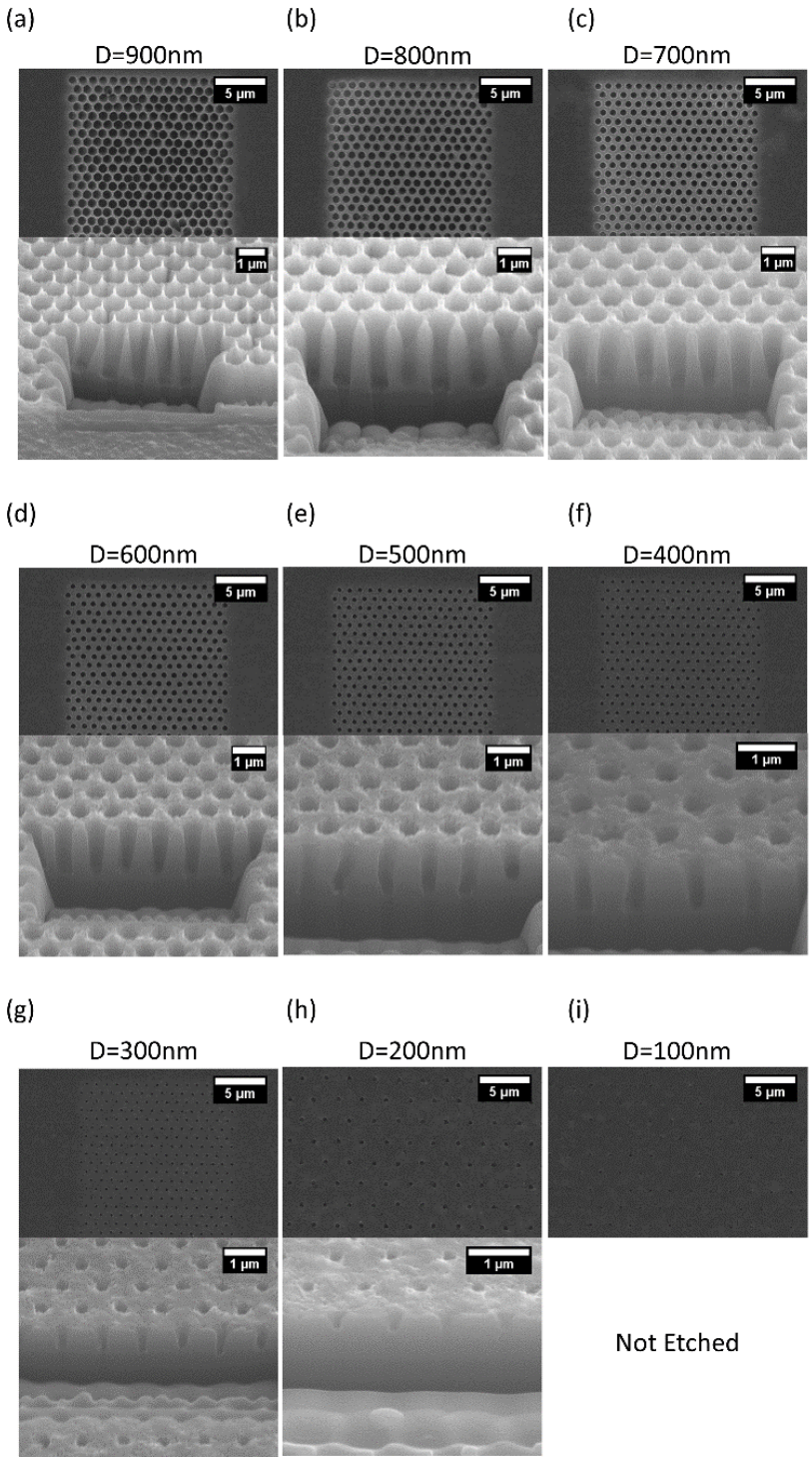

Figure 3.7: Top view (top) and 52 degree tilted view (bottom) SEM images of SAC-MacEtched dot arrays in a solution of 0.56 M HF, 0.26 M H_2O_2, 0.88 M DI, 0.21 M IPA ($\rho_{H_2O_2}$ = 0.32) for 10 minutes with the diameter of (a) 900 nm, (b) 800 nm, (c) 700 nm, (d) 600 nm, (e) 500 nm, (f) 400 nm, (g) 300 nm, (h) 200 nm, and (i) 100 nm at fixed pitch of 1 µm.

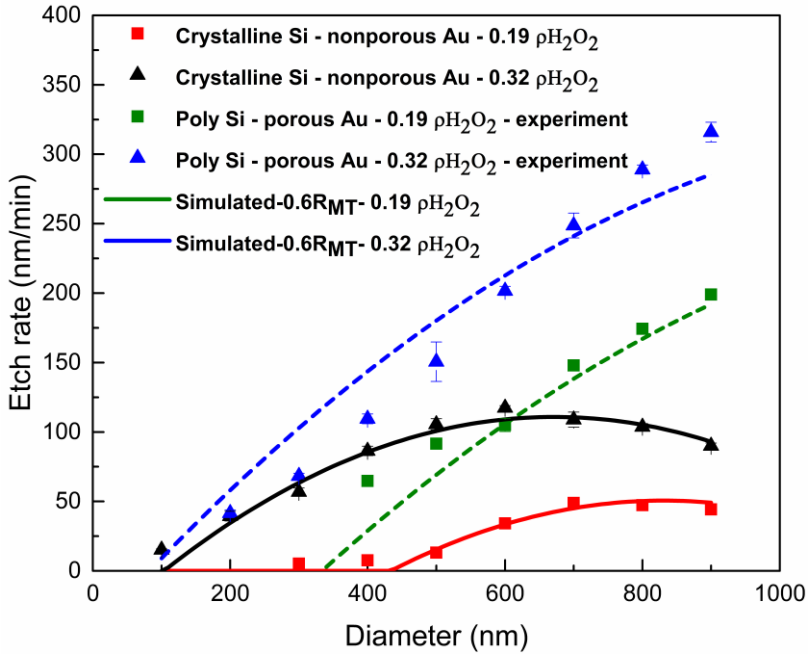

Figure 3.8 Etch rate as a function of diameter at fixed pitch of 1 µm, MacEtched at 0.19 and 0.32 $\rho_{H_2O_2}$.

Figure 3.8 shows the vertical etch rate as a function of the catalyst diameter from 100 nm to 900 nm at fixed pitch of 1 µm for c-Si with regular MacEtch and Poly-Si with SAC-MacEtch. Red and black symbols and curves represent the measured and fitted etch rate of c-Si via array MacEtched at 0.19 and 0.32 $\rho_{H_2O_2}$ respectively. Green and blue symbols represent the measured vertical etch rate of Poly-Si SAC-MacEtched at 0.19 and 0.32 $\rho_{H_2O_2}$ respectively. Green and blue curves show the fitted vertical etch rate of 0.19 and 0.32 $\rho_{H_2O_2}$ based on the modified empirical vertical etch rate model from the c-Si MacEtch. For Poly-Si, at 0.32 $\rho_{H_2O_2}$, etch rate increases from 40 nm/min to 320 nm/min as the diameter increases from 200 to 900 nm. As the H_2O_2 concentration decreases from 0.19 $\rho_{H_2O_2}$, the etch rate in every diameter decreases.

Decrease in etch rate with decreasing H_2O_2 concentration is due to the reduced hole injection rate. The vertical etch rate increase with increasing catalyst diameter is attributed to the enhanced CG. The oxidized Si under the catalyst need to be etched in order for catalyst to vertically

sink down. When the oxidized Si etch rate is fast or the effective area of the oxidized Si is small (i.e. smaller catalyst diameter), the vertical etching is governed by the amount of the holes injected in the Si (CG-limited). In this case, as the diameter of the catalyst increase, the effective area of the catalyst increases such that more amount of the holes is injected under the catalyst.

In contrast to the regular MacEtch on c-Si, (red and black), in Poly-Si SAC-MacEtch (green and blue), the vertical etch rate does not saturate and decrease as the diameter increases. This is because the MT is enhanced by increased solution access through the pinholes in the porous catalyst. The MT enhancement can be estimated by fitting the experimental etch rate data to modified empirical vertical etch rate model from the c-Si, equation (2.8) which is described as

$$R_{MacEtch} = a + xR_{MT} + R_{CG} \tag{3.1}$$

where a is the intercept, R_{CG} is the etch rate increased by the CG and R_{MT} is the etch rate decrease by the limited MT; $R_{MT} = -bD-cD^2$, $R_{CG} = bP-cP^2+2cDP$, D and P are the diameter and pitch of the catalyst array, b and c are extracted first- and second-order polynomial coefficients.

Assume the difference in oxidized Si etch rate in Poly-Si and crystalline Si substrates are small and the decrease in CG with porous catalyst is not significant. Then, the etch rate of the Poly-Si can be fitted by replacing the R_{MT} to xR_{MT} which indicates that the etch rate decreased by MT (R_{MT}) is reduced by x percent. The Poly-Si etch rate for both 0.19 and 0.32 fit when x = 0.6 which indicates that the vertical etch rate decreased by the limited MT is reduced by 60% (i.e. MT is enhanced by 40%).

3.5 Through Via Array on Stacked PolySi/SiO_2 Substrate by SAC-MacEtch

The longer time SAC-MacEtch is demonstrated to investigate the etching behavior at PolySi/SiO_2/c-Si substrate interface. On the SOI substrate consists of 1 μm Poly-Si and 100 nm

SiO_2, 2 μm and 4 μm diameter catalyst arrays with fixed spacing of 2 μm are patterned, then deposited with 10 nm porous Au.

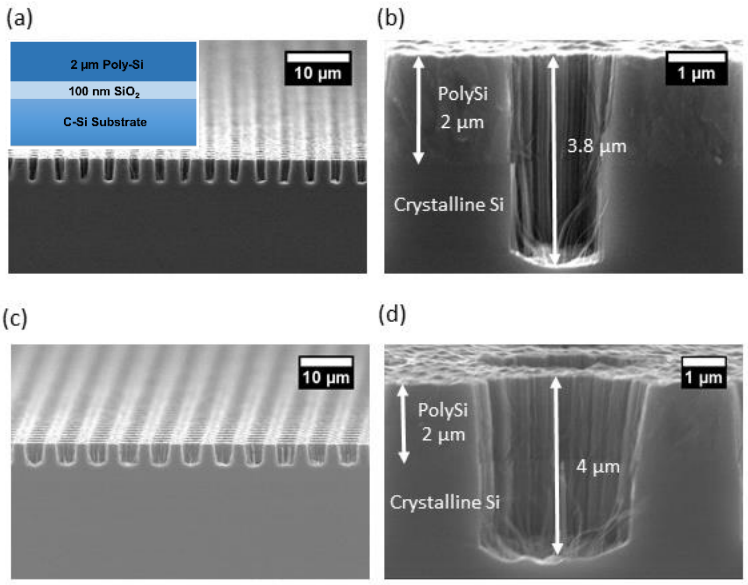

Figure 3.9: Low-magnification cross-sectional SEM images showing via arrays of (a) 2 μm and (c) 4 μm diameter with 2 μm spacing fabricated by SAC-MacEtch. High-magnification cross-sectional SEM images of single via of (b) 2 μm (d) 4 μm diameter showing the SAC-MacEtch continues to c-Si substrate after etch through 2 μm PolySi and 100 nm SiO_2.

Figure 3.9 (a) and (b) show the low- and high-magnification cross-sectional SEM images of 2 μm diameter, 2 μm spacing (4 μm pitch) via array SAC-MacEtched in 0.1 $\rho_{H_2O_2}$ for 15 min respectively. Figure 3.9 (c) and (d) show the low- and high-magnification images of the 4 μm diameter, 2 μm spacing (6 μm pitch) via array etched in same condition as shown in Figure 3.9 (a) and (b).

Both 2 μm and 4 μm catalyst arrays are MacEtched completely through 2 μm Poly-Si, 100 nm SiO_2 and continued to the c-Si substrate, formed via arrays with total depth of 3.8 μm and 4 μm respectively, without the catalyst delamination or detouring. Even though the SiO_2 etch rate is fast (1.8 μm/min at 49 % HF), the lateral etching of SiO_2 in between the PolySi and c-Si is minimal as compared to the MacEtch. On the bottom of every via, NWs for which the length corresponds

to the etched depth of c-Si substrate are formed through the catalyst pinholes (~ 1.8 and ~2um for 2 and 4 um diameter respectively).

The minimized catalyst delamination or detouring is due to the anchoring mechanism of SAC-MacEtch as described in the Section 3.3. The quenched SiO_2 lateral etching can be explained by the decreased SiO_2 etch rate resulted by the limited mass transport. The transport of etchant and byproducts of SiO_2 are limited not only by the thickness of the SiO_2 but also the consumption HF and limited transport of byproducts resulting from the MacEtch such that the effective SiO_2 etch rate decreases smaller than the MacEtch rate (253 and 266 nm/min for 2 μm and 4 μm diameter respectively). The shorter NWs formed through the pinholes of the porous catalyst at the bottom of the vias is due to (1) selectively polished Poly-Si resulted from the unconsumed hole diffusion and (2) Poly-Si liftoff from the SiO_2 lateral etching in NWs.

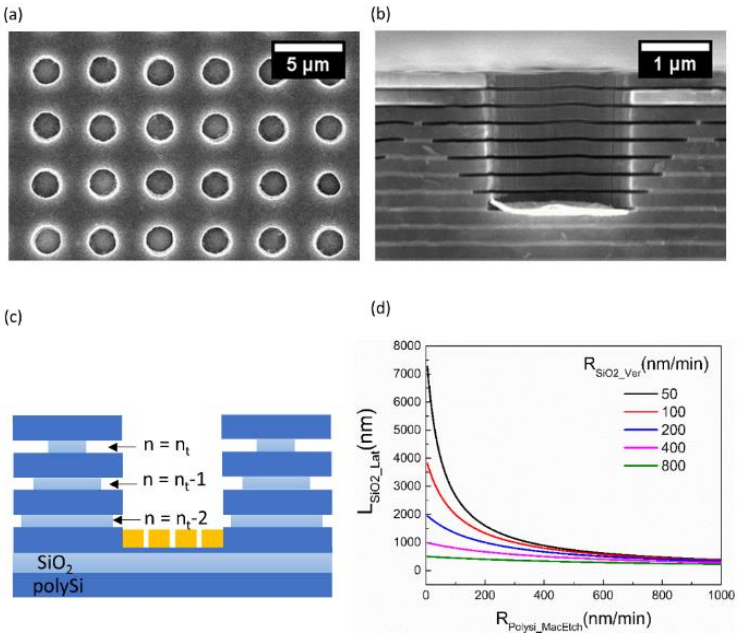

Figure 3.10: (a) Top and (b) cross-sectional SEM images of 2 μm diameter 4 μm pitch via array formed on poly-Si/SiO_2 stacks by MacEtched at 0.32 $\rho_{H_2O_2}$ for 5 min, (c) cross-sectional schematic of the etched via with SiO_2 lateral etching, (d) simulated SiO_2 lateral etching depth ($L_{SiO_{2Lat}}(n_t)$) as the function of poly-Si MacEtch rate ($R_{Polysi\_MacEtch}$) at varied SiO_2 vertical etch rate ($R_{SiO_2\_Ver}$).

Figure 3.10 (a) and (b) show top and cross-sectional SEM images of 2 μm diameter discrete dot catalyst array at pitch of 4 μm deposited on the 200 nm/50 nm Poly-Si/SiO2 stacked substrate MacEtched in 0.32 $\rho_{H_2O_2}$ for 5 min.

The catalyst vertically etches through the Poly-Si by SAC-MacEtch, then continues to etch through the SiO_2 layer by chemical etching. During this alternating etching process, the catalyst is anchored from the delamination and detouring such that it forms the uniform through via array on stacked Poly-Si/SiO_2 substrate. Note that the SiO_2 layers are laterally etched; etch depth linearly increases from 256 to 910 nm from the bottom to the top of the SiO_2 layers. The SiO_2 lateral etching starts when the SiO_2 layer is exposed right after catalyst etches through the Poly-Si placed above the SiO_2 layer such that the time that SiO_2 layer is exposed to solution for lateral etching decreases for the deeper layer.

The lateral etch depth of the first SiO_2 layer is smaller than the vertical via etch depth. This indicates that the lateral etch rate of the SiO_2 is slower than the vertical etch rate of Poly-Si and SiO_2. The MT of the Poly-Si and the SiO_2 vertical etching is greater than the MT of SiO_2 lateral etching; MT of the vertical etching is enhanced by the porous catalyst while the MT of the SiO_2 lateral etching is limited by the thickness of the SiO_2.

Figure 3.10 (c) shows the cross-sectional schematic of the etched Poly-Si/SiO_2 stacked via. The lateral etch depth for the n-th SiO_2 layer ($L_{SiO_2\_Lat}(n)$) can be analytically described as

$$L_{SiO_{2_{Lat}}}(n) = R_{SiO_2\_Lat} \times \frac{n}{n_t} t \tag{3.2}$$

where n_t is the total number of the stacked poly-Si/SiO_2 vertically etched through, $R_{SiO_2\_Lat}$ is the SiO_2 lateral etch rate, and *t* is the total etch time.

On the other hand, the vertical etch depth though stacked Poly-Si/SiO_2 can be described as

$$L_{Ver} = (R_{Polysi\_MacEtch} + R_{SiO_2\_Ver}) \times t \tag{3.3}$$

where L_{Ver} is the vertical etch depth, $R_{Polysi\_MacEtch}$ is the poly-Si vertical MacEtch rate, $R_{SiO_2\_Ver}$ is the SiO_2 vertical etch rate. $R_{SiO_2\_Lat}$ and $R_{SiO_2\_Ver}$ are different due to the etch rate difference from the limited MT. Since the *T* is same, equations (3.2) and (3.3) can be combined as

$$L_{SiO_{2Lat}}(n) = \frac{n(R_{SiO_{2Lat}} \times L_{ver})}{n_t(R_{Polysi\_MacEtch} + R_{SiO_2\_ver})} \tag{3.4}$$

This indicates that the $L_{SiO_2\_Lat}$(n) can be quenched by increase the $R_{Polysi\_MacEtch}$ or $R_{SiO_2\_Ver}$ or decreasing the $R_{SiO_{2Lat}}$. $R_{Polysi\_MacEtch}$ can be increased by increasing H_2O_2 concentration, $R_{SiO_2\_ver}$ can be increased by increasing the catalyst pinhole density. Note that $R_{SiO_2\_Ver}$, $R_{SiO_2\_Ver}$ and $R_{SiO_{2Lat}}$ are simultaneously affected by the solution concentration.

Figure 3.10 (d) shows the simulated $L_{SiO_{2Lat}}(n = n_t)$ as the function of $R_{Polysi\_MacEtch}$ from 5 to 1000 nm/min at varied $R_{SiO_2\_Ver}$ from 50 to 800nm/min. The L_{ver} is fixed to 2 μm, and $R_{SiO_{2Lat}}$ is fixed to 200 nm/min. $L_{SiO_{2Lat}}$ decreases as the $R_{Polysi\_MacEtch}$ increases then gets saturated at large $R_{Polysi\_MacEtch}$. $L_{SiO_{2Lat}}$ decreases as the $R_{SiO_2\_Ver}$ increases from 50 to 800 nm/min. The decrease in $L_{SiO_{2Lat}}$ with increasing $R_{SiO_2\_Ver}$ is larger for low $R_{Polysi\_MacEtch}$.

4. LARGE-SCALE THROUGH SILICON VIA ARRAY AND GALLIUM ARSENIDE VIA ARRAY BY SAC-MACETCH

Self-Anchored Catalyst (SAC) MacEtch is not only limited to fabricate the vertical via array on polycrystalline silicon (Si) substrate. The advantage of enhancing the mass transport (MT) of the reactants and byproducts and anchoring the catalyst from delamination and detouring can be applied in the Si and compound semiconductor materials. In this chapter, the large scale through Si via and GaAs via array is demonstrated by SAC-MacEtch.

4.1 Large-Scale Through Silicon Via (TSV) Array by SAC-MacEtch

SAC-MacEtch can be applied on the large dimension catalyst to enhance the vertical etching uniformity. On the 500 μm thick p-type substrate, 320 μm x 320 μm square catalyst arrays with pitch of 740 μm are patterned by optical lithography, then 20 nm nonporous Au and 10 nm porous Au are deposited for the MacEtch comparison.

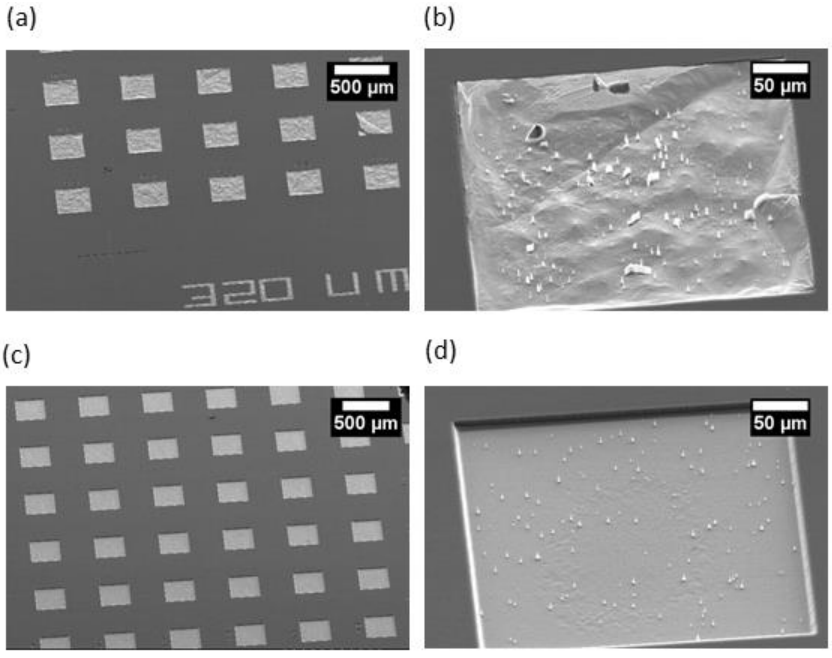

Figure 4.1: A 45 degree tilted SEM images of MacEtched 320 um x 320 um catalyst array deposited with (a), (b) 20 nm nonporous Au and (c), (d) 10 nm porous Au.

Figure 4.1 (a) and (b) show the low- and high-magnification 45 degree tilted SEM images of nonporous 20 nm Au catalyst, (c) and (d) show ones with the 10 nm porous Au catalyst MacEtched in the identical solution. The catalyst delamination, cracks, and non-uniform vertical etching across the pattern are observed in the nonporous catalyst while uniform vertical MacEtch is observed in the porous catalyst. The enhanced etching uniformity in the porous catalyst is attributed to the enhanced MT and the catalyst anchoring. The transport of etchant and byproducts is enhanced through the pinholes, and the catalyst perturbation caused during the transport is minimized with the catalyst anchoring by the NWs formed through the pinholes.

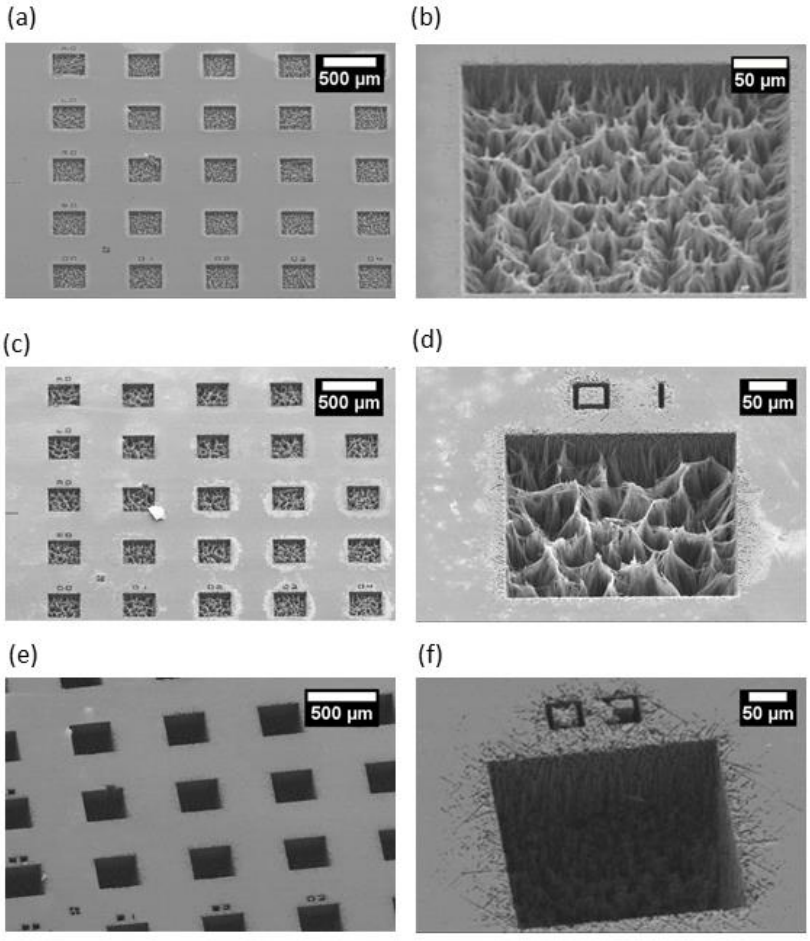

Figure 4.2: The 45 tilted cross-sectional SEM images of 320 um x 320 um catalyst array SAC-MacEtched for (a) (b) 1.5 hours, (c) (d) 6 hours, and (e) (f) for 48 hours.

Figure 4.2 (a) to (f) show the low-and high-magnification images of the 320 μm x 320 μm catalyst array SAC-MacEtched in 0.41 $\rho_{H_2O_2}$ for 1.5, 6 and 48 hours, respectively. The MacEtch solution is replaced every 3 hours to prevent the change in solution concentration due to solution evaporation and consumption. The sample etched for 1.5 hours shows the dense NWs arrays formed through the pinholes are clustered together due to the high surface tension. With the longer time etching, the length of the NWs decreases by the chemical polishing resulted from the diffusion of excess holes.

Figure 4.3: The 320 μm x 320 μm though silicon via array fabricated by SAC-MacEtch in 20 ml HF, 30 ml H_2O_2, 16 ml IPA, and 16 ml DI for 96 hours.

Figure 4.3 shows the 320 μm x 320 μm through Si via array fabricated by SAC-MacEtch in the identical etching condition shown in Figure 4.2 for ~96 hours.

4.2 GaAs Via Array by SAC-MacEtch

The SAC MacEtch can be applied not only on the Si but also on the compound semiconductor materials. This allows to MacEtch the discrete catalyst array which could not be demonstrated by the conventional MacEtch.

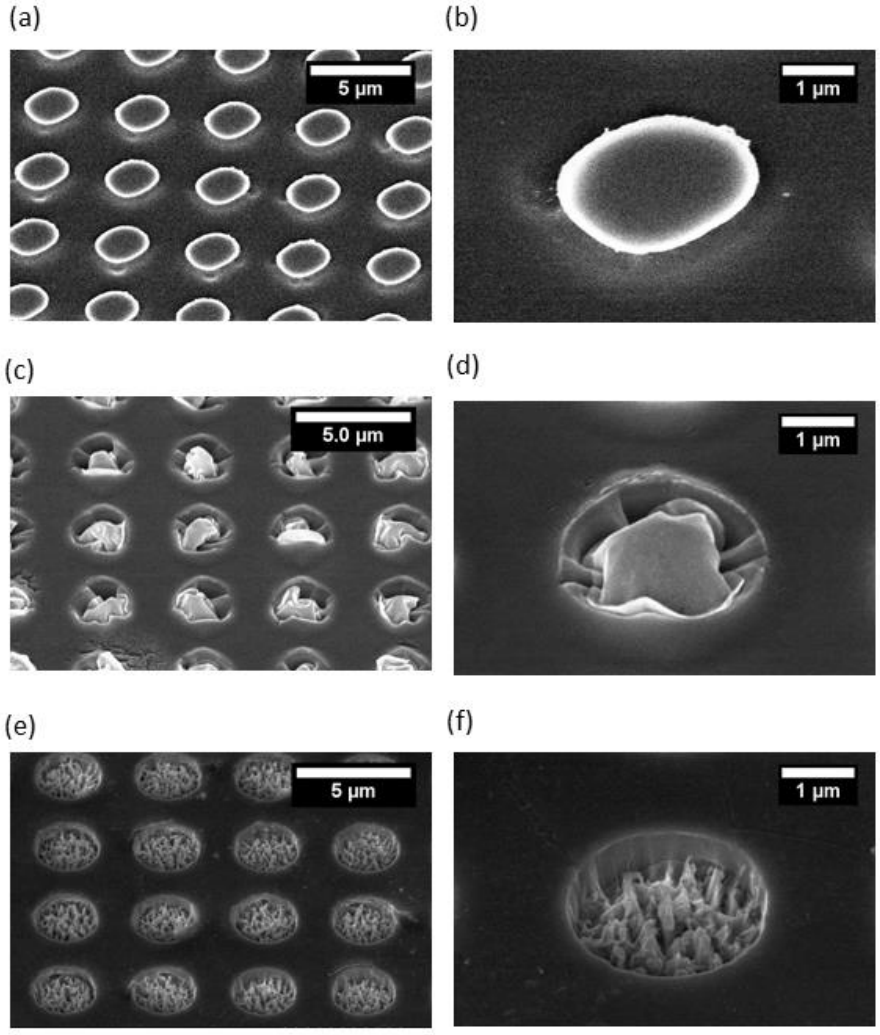

Figure 4.4: The 45 tilted cross-sectional SEM image of GaAs substrate with (a), (b) 20 nm nonporous catalyst array MacEtched in the 0.28 M HF, 0.56 M DI, 0.025 g $KMnO_4$ for 10 minutes (low oxidant concentration), (c), (d) 20 nm nonporous catalyst array MacEtched in 10 ml HF, 10 ml DI, 0.1g $KMnO_4$ for 10 minutes (high oxidant concentration), (e), and (f) 10 nm porous catalyst Array SAC-MacEtched in the identical solution as (c), (d).

The semi-insulating (SI) GaAs wafer is patterned with the 2 μm diameter array with 2 μm spacing using optical lithography, then 20 nm nonporous and 10 nm porous Au are deposited for the MacEtch comparison.

Figure 4.4 show the 45 degree tilted SEM images of GaAs substrate with (a), (b) 20 nm nonporous Au catalyst array MacEtched in the 0.28 M HF, 0.56 M DI, 0.025 g $KMnO_4$ for 10 minutes (low oxidant concentration), (c), (d) 20 nm nonporous Au catalyst array MacEtched in the 10 ml HF, 10 ml DI, 0.1g $KMnO_4$ for 10 minutes (high oxidant concentration), (e), (f) 10 nm porous Au catalyst array MacEtched in the 0.28 M HF, 0.56 M DI, 0.1g $KMnO_4$ for 10 minutes.

The inverse MacEtch is observed for the nonporous catalyst array MacEtched in low oxidant concentration. Here, inverse MacEtch is defined as the chemical etching of the bare GaAs regions. For the nonporous catalyst MacEtched in high oxidant concentration, forward MacEtch is observed but the catalyst deformation and detouring are observed in every etched pores. For the porous catalyst, the catalyst vertically etched down by ~600 nm with minimized catalyst deformation and detouring and formed GaAs NWs through the catalyst pinholes.

The inverse MacEtch in nonporous catalyst MacEtched at low oxidant concentration is due to the limited mass transport. The unconsumed holes in the center of the catalyst are diffused on the bare GaAs results in the chemical etching; the catalyst acts as an etching mask instead. The catalyst deformation and detouring in nonporous catalyst MacEtched at high oxidant concentration is due to the limited transport and vigorous catalyst perturbation resulted by transport of etchant/byproducts. The uniform etching in porous catalyst MacEtched at high oxidant concentration is attributed to the enhanced mass transport though pinholes and catalyst anchoring by the GaAs NWs formed through the pinholes.

5. MACETCH OF TITANIUM NITRIDE CMOS-COMPATIBLE CATALYST

Despite to the advantage of producing high aspect ratio (HAR) complex structure using the MacEtch, using the noble metal catalyst is a major drawback for MacEtch to be applied in electronic device applications specifically in the front end of the line (FEOL) and back end of the line (BEOL) in the metal-oxide semiconductor (CMOS) fabrication process due to the deep level defects. In order for MacEtch to be applied in the CMOS process, the catalyst not only has to be CMOS-compatible but also has to satisfy the MacEtch catalyst requirements of (i) high HF resistivity and (ii) hole generation and injection capability. Such a metal catalyst has not been found yet.

In this chapter, the first demonstration of CMOS-compatible titanium nitride assisted chemical etching is demonstrated using the modified true vapor phase MacEtch. The Si nanowire arrays are fabricated by mesh patterned TiN. The nanowire length as the function of the mesh dimension, solution concentration, etching temperature, and TiN thickness is systematically investigated.

5.1 Property of TiN

TiN is a hard ceramic material that is often used as the conductive barrier in Si device contacts to prevent the metal diffusion into the Si substrate [25-29]. TiN is categorized as Level 2 which is allowed for both the front end of the line (FEOL) and back end of the line (BEOL) processing. TiN is a good candidate for the CMOS-compatible MacEtch. Unlike the other CMOS-compatible materials such as Al, Co and Ni, TiN is resistive to HF [30]. In addition, TiN has the work function between 4.2 eV to 4.5 eV [31, 32], thus, it has the capability to produce the holes by reduction reaction and to inject the holes in the valence band of the Si.

5.2 Fabrication Process

Boron doped p-type Si crystalline (100) substrate with resistivity of 1-100 Ω-cm was used for every experiments. Lam Research Corporation (LRCX) provided the substrate deposited with TiN; native oxide on Si was etched in 1:100 HF:DI. Then, the substrates were deposited with 5, 10 and 30 nm thickness TiN using physical vapor deposition (PVD). Then, a 15 nm SiO_2 hard mask was deposited using Trion Minilock – Orion plasma enhanced vapor deposition (PECVD). The electron beam (e-beam) resist of 950 k PMMA in 2 % anisole was spin-coated at 2000 rpm for 60 s (~80 nm thickness) and baked at 200 ˚C for 2 minutes. Patterns consist of hexagonal ordered dot arrays with diameters varying from 200 nm, 400 nm, 600 nm, 800 nm at pitch of 400 nm, 600 nm, 800 nm, and 1000 nm (total of 10 arrays) were exposed using e-beam lithography and developed in 1:3 MIBK:IPA for 2 minutes.

The patterns were transferred on the SiO_2 hard mask by etching in 1:10 BOE for 15 s. The PMMA was removed in 5 min cycles in Aceton, Methanol, and IPA. The residual PMMA was etched by O_2 RIE at 200 mw for 2 min. The exposed TiN patterns were etched in 1:10 $NH_4OH:H_2O_2$ (~15 nm/min). The SiO_2 hard mask was etched in 1:10 BOE for 15 s.

The modified vapor phase (VP) MacEtch was done after the sample patterning. First, the 3-inch home Si substrate was placed on the hot plate. Then, the TiN sample was placed on the center of the home substrate. The surface temperature of the home substrate and TiN sample were calibrated to match the etching temperature (50, 60, 70, 80, 90 ˚C). The MacEtch solution of 0.28 M HF, 13 mM H_2O_2, 0.39 M IPA was premixed. The 10 μL solution was dropped on the home substrate around the TiN sample using the HF resistive micro-pipette. A total of 6~8 solutions were dropped on the home substrate ~2 cm away from the TiN sample. The solution was replenished soon after the drops were completely evaporated. The VP-MacEtched samples were

inspected using the secondary electron microscope (Hitachi S-4800). The average NW heights were measured from the 45 degree tilted SEM images. The height aspect ratio NWs at given etching time were inspected by the 52 degree tilted images after the cross-sectional ion milling using the focused ion beam (FEI-DB4800).

For the current density measurement sample, the same p-type silicon substrates deposited with 30, 10, 5 nm thickness TiN were first deposited with 15 nm SiO_2 by PECVD. Then, HMDS and PR were spin-coated at 4500 RPM for 30 s respectively. The resist is baked in 110 °C for 1 min and the interdigitated pad patterns were exposed using a Karl Suss MJB-3 aligner. The samples were developed in AZ 917 MIF developer for 2 minutes. The exposed patterns were transferred on SiO_2 by etching in BOE for 15 s. After removing PR in acetone, methanol, IPA cycles, patterns on the SiO_2 were transferred on the TiN by etching in 1:10 NH_4OH:H_2O_2. Then, the I-V curve was measured and the current density was calculated by dividing the measured current by the area of the TiN interdigitated pads.

5.3 Liquid Phase TiN MacEtch: Inverse MacEtch

Figure 5.1 (a) and (b) shows the 45 degree tilted SEM image of the mesh patterned TiN on Si substrate liquid phase (LP) MacEtched in 0.28 M HF, 13 mM H_2O_2, and 0.39 M IPA for 30 minutes at 70 °C. The bare Si area (off TiN area) is chemically etched instead of Si under the TiN forming the inverse MacEtched via like surface textures. Figure 5.1 (c) shows the cross-sectional SEM image of mesh patterned TiN on Si LP-MacEtched in the same solution for 5 minutes showing the process of forming the porous Si under the bare Si and TiN. Top- and bottom-right subset images show the high-magnification SEM images under the bare Si and TiN respectively.

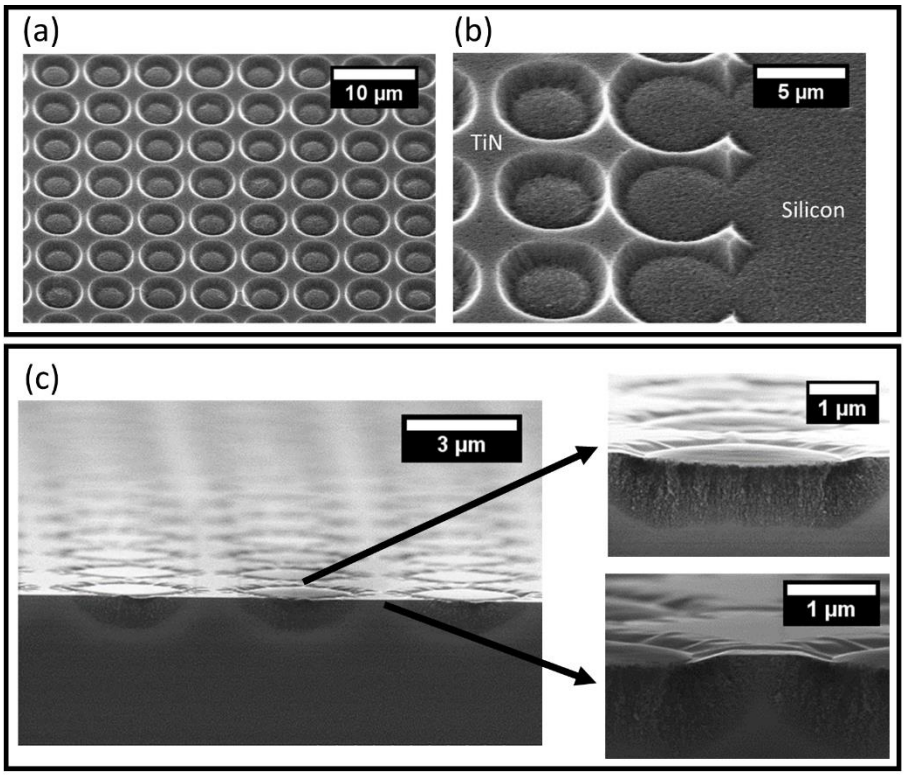

Figure 5.1: The (a) and (b) show high- and low-magnification 45 degree tilted SEM images of the mesh patterned 30 nm thickness TiN MacEtched in conventional liquid phase with 0.28 M HF, 13 mM H_2O_2, 0.39 M IPA for 30 minutes at 70 °C showing the inverse MacEtch, (c) cross-sectional SEM image of the same sample MacEtched in the same solution concentration for 5 min showing the process of inverse MacEtch subset images on top-right shows the Si at off TiN, bottom-right shows the Si under the TiN.

The Si under the TiN is unevenly etched resulting the deformation of the TiN. The porosity increases for the Si further away from the TiN. This indicates that the formation and removal of the oxidized Si is faster on the bare Si. The inverse MacEtch of InP substrate with a Pt catalyst is previously reported by Kim et al. [33]. For InP with a Pt catalyst, inverse MacEtch is a result of the native oxide forming in between the Pt and InP interface that is not dissolvable in acid (H_2SO_4). For Si with a TiN catalyst, based on the comparison images in Figure 5.1 (b), we find that inverse MacEtch results from the limited MT of the etchant under the TiN. The injection and diffusion of holes are faster than the removal of the oxidized Si formed under the TiN such that the unconsumed

holes are diffusing away from under the TiN to bare Si surface. This results in the formation and removal of the oxidized Si on the bare Si instead.

5.4 Vapor Phase TiN MacEtch: Forward MacEtch

The mesh patterned 30 nm thickness TiN on Si substrate is MacEtched using the conventional LP- and VP-MacEtch and modified VP-MacEtch with the solution mixture of 49% HF, 30% H_2O_2 and IPA.

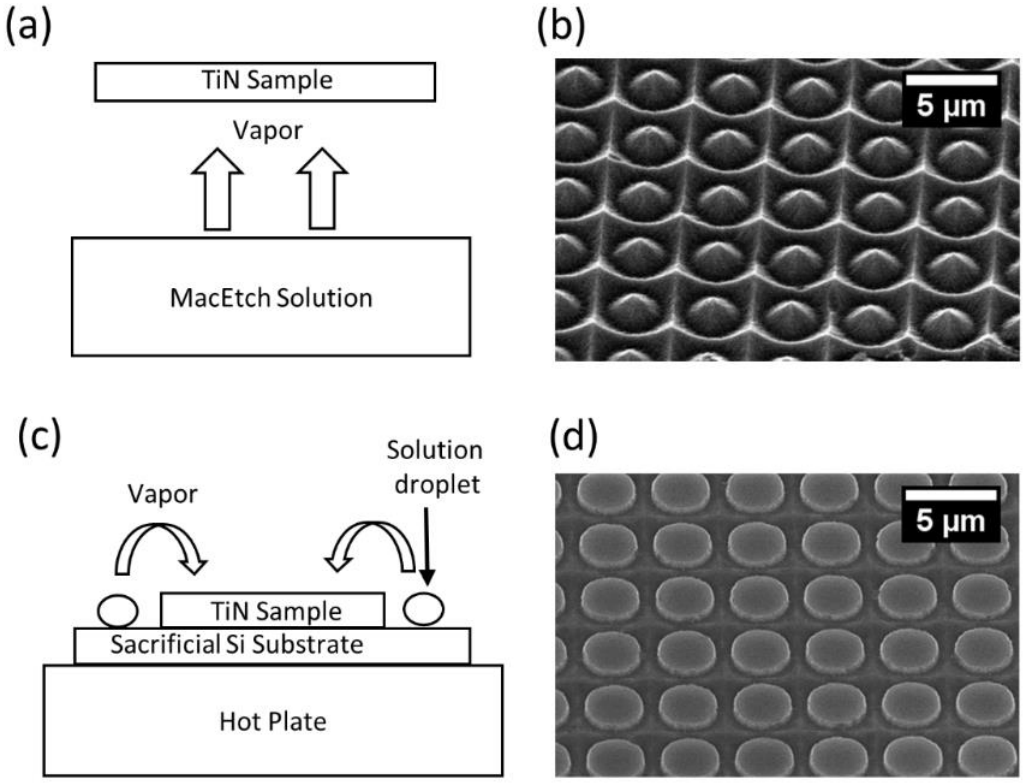

Figure 5.2: (a) Conventional vapor phase MacEtch setup schematic reported by Hildreth et al., (b) 45 degree tilted SEM image of mesh patterned TiN vapor phase MacEtched with the setup shown in (a), (c) new vapor phase MacEtch setup schematic, and (d) 45 degree tilted SEM image of mesh patterned TiN MacEtched with the new vapor phase MacEtch shown in (c).

Figure 5.2 (a) shows the VP-MacEtch setup schematic that is first purposed by Hildreth et al. for the demonstration of VP-MacEtch of Au, Ag, Pd/Au catalyst on Si substrate [34]. In this

case, the TiN sample is held upside-down ~5 cm above the MacEtch solution. The substrate is heated while the solution is kept at room temperature. The MacEtch occurs when the solution is evaporated and diffused on the sample surface. Figure 5.2 (b) shows the 45 degree tilted SEM image of the mesh patterned TiN VP-MacEtched with the same solution with substrate at 70 °C for 5 minutes.

The etched features show process of both inverse and forward MacEtch that is not observed in the conventional VP-MacEtch of Au on Si substrate (i.e. intermediate MacEtch); the pyramidal-like tapered pillars are formed on the bare Si region by the forward MacEtch. At the same time, the connected pyramidal-like textures are formed under the TiN mesh by the inverse MacEtch. This indicates that the MT enhancement by the conventional vapor phase MacEtch is still not sufficient to quench the inverse MacEtch by reducing the number of unconsumed holes diffusing to the bare Si regions. This is attributed to the simultaneous MacEtch reactions in vapor and liquid phases. In the conventional VP-MacEtch, the solution vapor is easily condensed on the sample surface from the temperature difference between solution vapor and substrate. The condensed solution can be trapped in the TiN and Si interface that can block the diffusion path of etchant and byproduct vapor species.

In order to overcome the vapor condensation, both the solution and the sample are heated at the same temperature. Figure 5.2 (c) shows the schematic of the modified VP-MacEtch setup schematic. The sacrificial 4-inch Si substrate is placed on the hot plate and the mesh patterned TiN sample is placed on top of the heated sacrificial Si substrate. The 10 μL droplets from the premixed MacEtch solution were dispersed on the sacrificial Si substrate ~1 cm away from the edge of the TiN sample using the micro-pipette. The MacEtch starts when the vaporized MacEtch solution

diffuses on the TiN. The solution droplets on the sacrificial Si substrate were replenished soon after the droplets were completely evaporated.

Figure 5.2 (d) shows the 45 degree tilted SEM image of the mesh patterned TiN VP-MacEtched with the same solution at 70 °C for 5 minutes using the setup shown in Figure 5.2 (c). The Si under the TiN is uniformly etched by forward MacEtch while the tapering of the forward MacEtched pillars is reduced by quenching the inverse MacEtch.

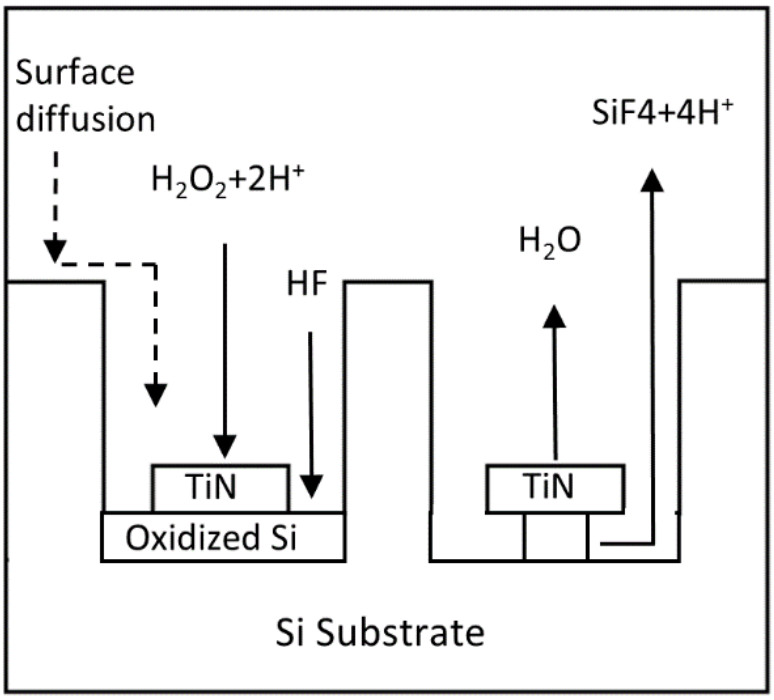

Figure 5.3: Cross-sectional schematic showing the mechanism of the vapor phase MacEtch.

Figure 5.3 shows the cross-sectional 2D schematic of the VP-TiN-assisted chemical etching mechanism. The etching mechanism can be divided into two parts; (a) vapor phase diffusion of the reactants (HF and H_2O_2) and (b) vapor phase diffusion of the byproducts (H_2O, H_2SiF_6, and H_2). When H_2O_2 and H^+ vapor diffuse on the TiN, the holes are generated and injected in the valance band of the Si by reduction reaction to produce the oxidized Si under the TiN. When

H_2O_2 and H^+ vapor diffuse on the bare Si, reduction reaction does not occur due to the absence of the catalyst, thus bare Si serves as the mask that allows the etchant species to be diffused in lateral direction until they reach the nearest TiN catalyst (i.e. surface diffusion). The vertical etching occurs when the HF vapor diffuses on the oxidized Si produced by the hole injection. Since only the oxidized Si is chemically etched by HF, the effective amount of the HF vapor is again contributed by the vapor diffusing perpendicular to the oxidized Si and the vapor surface diffusing from Si or TiN to the oxidized Si.

The byproduct of reduction reaction (H_2O) is evaporated from the TiN interface to atmosphere. The byproducts of SiO_2 etching (H_2, SiF_4 and H_2SiF_6) are diffused from under the TiN to the atmosphere. It is important to note that the liquid byproducts (H_2O_2 and H_2SiF_6) need to be evaporated to be diffused to atmosphere while the vapor byproducts (H_2, SiF_6) can be diffused as they produce. When the evaporation rate of the liquid byproducts is slow due to the low substrate temperature, the vapor byproducts can be trapped under the catalyst which can lead to the delamination or crack of the catalyst.

The vertical etching is defined by the transport of the etchant and byproducts similar as the LP-MacEtch. However, the diffusion in the vapor phase is affected by the temperature with an order of 3/2 according to the Chapman-Enskog theory [35] which is described as

$$D = \frac{1.858\times10^{-3}T^{3/2}\sqrt{\frac{1}{M_1}+\frac{1}{M_2}}}{p\sigma_{12}^2\tau} \tag{5.1}$$

where D is the diffusion coefficient, T is the temperature, M_1 and M_2 are the molar mass of the vapor species, p is the pressure, σ_{12}^2 is the average collision diameter and τ is the temperature-dependent collision integral.

Where as in liquid phase, the diffusion coefficient of the solution is affected by the dynamic viscosity of the solution according to the Stokes-Einstein equation [36] which is described as

$$\frac{D_{T_1}}{D_{T_2}} = \frac{T_1}{T_2}\frac{\boldsymbol{u}_{T_2}}{\boldsymbol{u}_{T_1}} \tag{5.2}$$

where *D* is the diffusion coefficient, *T* is the temperature, *u* is the dynamic viscosity. Therefore, the MT can be significantly enhanced in the VP-MacEtch to overcome the limited MT resulted from the strong vdW's force between the TiN and Si substrate [37].

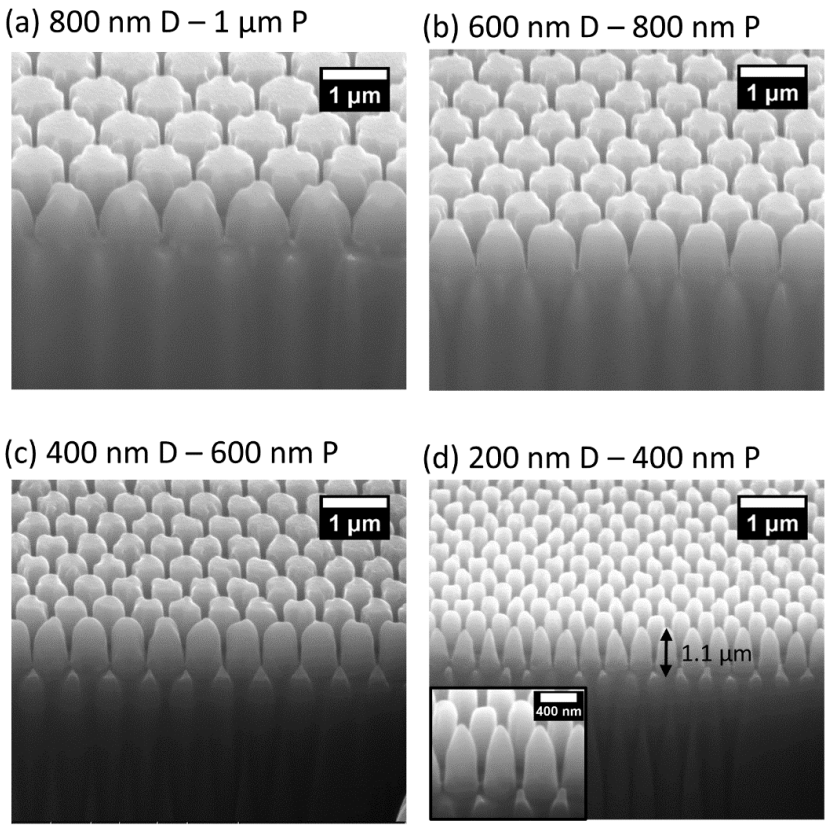

Figure 5.4: A 52 degree tiled cross-sectional SEM images after FIB showing the NW array fabricated by modified VP MacEtch with mesh catalyst of (a) 800 nm diameter, 1 um pitch (b) 600 nm diameter, 800 nm pitch, (c) 400 nm diameter, 600 nm pitch, and (d) 200 nm diameter, 400 nm pitch

Figure 5.4 (a) to (d) show 52 degree tilted cross-sectional SEM images after the FIB showing the mesh patterned TiN with diameter of 800, 600, 400, and 200 nm at fixed spacing of 200 nm VP-MacEtched with 0.28 M HF, 13 mM H_2O_2, and 0.39 M IPA at 90 °C for 5 minutes.

The 200 nm diameter NW array with length of 1.1 μm is produced (Figure 5.4 (d)), giving the aspect ratio > 5. The tapering of the NWs results from the material redeposition during the ion milling.

5.5 Dimension Dependence

Figure 5.5 and Figure 5.6 show the 45 degree tilted SEM images of 30 nm TiN mesh with diameter from 200 nm to 800 nm with varied pitch from 400 nm to 1000 nm VP-MacEtched with 13 mM and 32 mM H_2O_2 at the fixed 0.28 M HF and 0.39 M IPA at 70 °C for 5 minutes, respectively.

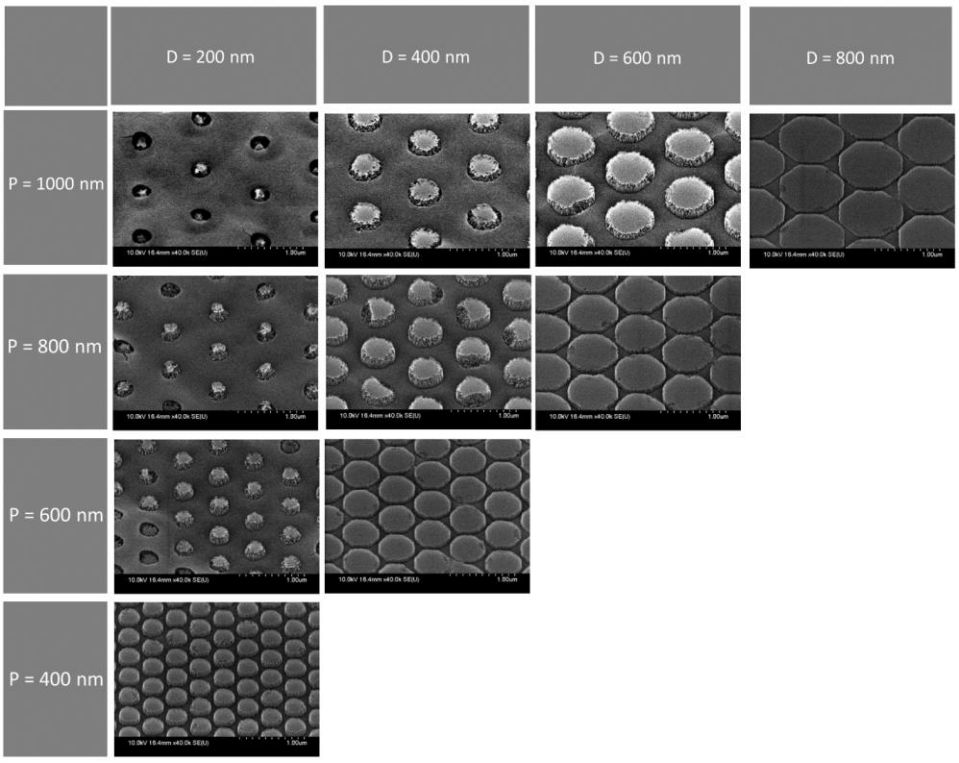

Figure 5.5: A 45 degree tilted SEM images of 30 nm TiN mesh with diameter from 200 to 800 nm with pitch from 400 to 1000 nm vapor phase MacEtched with 0.28 M HF, 13 mM H_2O_2, 0.39 M IPA at 70 °C for 5 minutes.

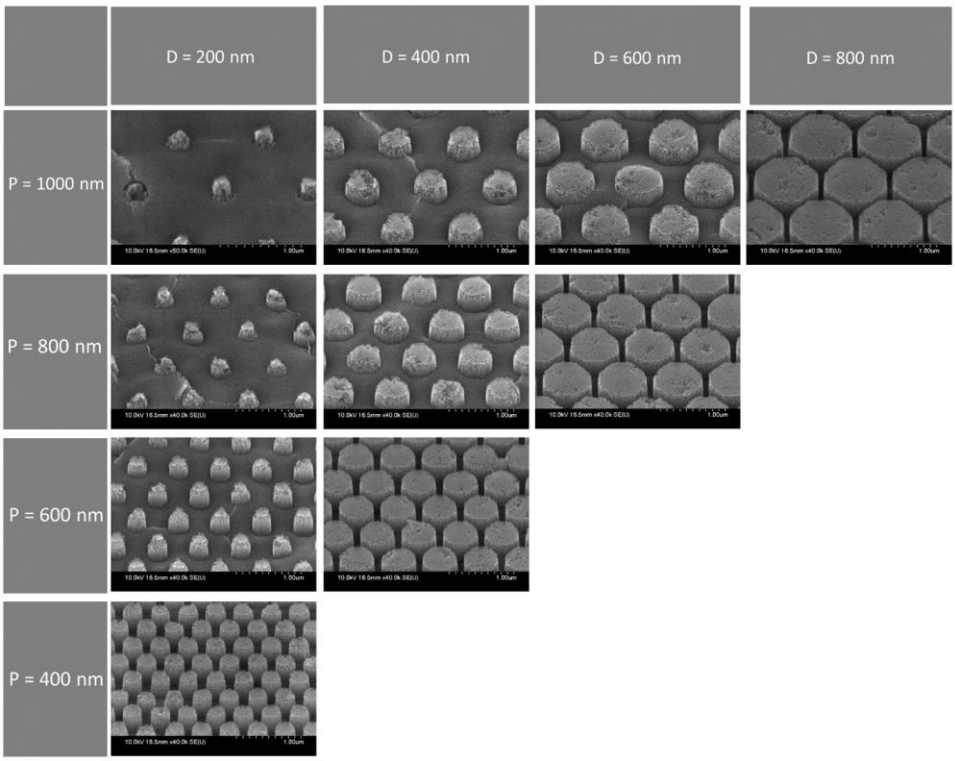

Figure 5.6: A 45 degree tilted SEM images of 30 nm TiN mesh with diameter from 200 to 800 nm with pitch from 400 to 1000 nm vapor phase MacEtched with 0.28 M HF, 32 mM H_2O_2, 0.39 M IPA at 70 °C for 5 minutes.

Figure 5.7 shows the average NW length as the function of mesh diameter from 200 to 800 nm at varied pitch of 1000, 800, 600, 400 nm VP-MacEtched with 13 and 32 mM H_2O_2 with fixed 0.28 M HF and 0.39 M IPA at 70 °C for 5 minutes. For 13 mM H_2O_2 at 1000 nm and 800 nm pitch, the average NW length shows the inverted parabolic trends; for 1000 nm pitch, the NW length increases from 60 to 220 nm as the diameter increases from 200 to 600 nm and it decreases to 80 nm as the diameter further increases to 800 nm. The diameter where the highest NW length is defined as D_M. As the pitch decreases from the 1000 nm to 400 nm, D_M shifts from 600 to 200 nm. When the H_2O_2 concentration increases from 13 to 32 mM, the average NW length in every diameter increases and the parabolic etching trend changes to linear such that the NW length only increases with increasing diameter for every pitch.

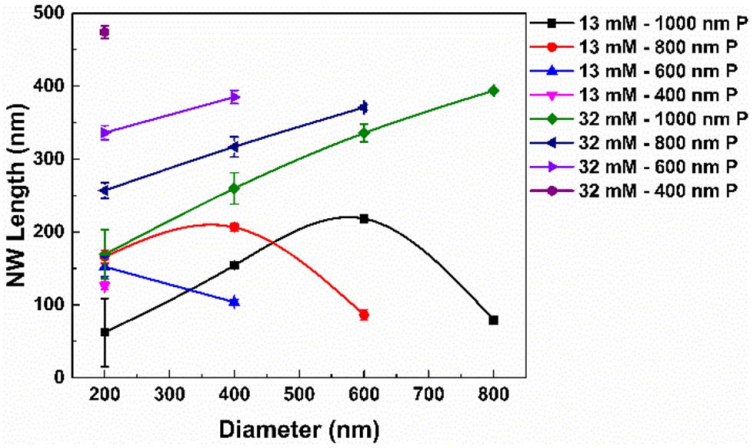

Figure 5.7: A 52 degree tiled cross-sectional SEM images after FIB showing the NW array fabricated by modified VP MacEtch with mesh catalyst of (a) 800 nm diameter, 1 um pitch (b) 600 nm diameter, 800 nm pitch, (c) 400 nm diameter, 600 nm pitch, and (d) 200 nm diameter, 400 nm pitch

The parabolic NW length trend is resulted from the competition of CG and MT similar to the one that is observed in the via array MacEtch in Chapter 3. However, the etching trend is opposite due to the difference in the catalyst shape (discrete vs. mesh). In this case, the increase in NW length with an increasing diameter ($D < D_M$) is contributed from the limited-MT. As the mesh diameter increases, the spacing of the TiN decreases such that the amount of the oxidized Si that needs to be removed to make the vertical etching is reduced. The decrease in NW length with an increasing mesh diameter ($D > D_M$) is due to the limited-CG. The effective area of the TiN that can inject the holes by the reduction reaction decreases with increasing diameter (i.e. decreased TiN spacing).

Critical diameter shifting to the smaller diameter with decreasing pitch is simply due to the fixed spacing; the volume of the oxidized Si that needs to be removed is the same for the fixed spacing. We find that the difference in etch depth at fixed mesh spacing is not significant for different diameters. This indicates that the etch depth contributed by the surface diffusion is not significant at the given etching condition.

The increased average NW length at every mesh diameter and pitch for increased H_2O_2 (32 mM) is contributed from the increased hole injection rate. The increase in etch rate with increasing mesh diameter also supports the CG and MT competition mechanism by showing the etching is completely governed by the limited MT.

5.6 Temperature Dependence

Figure 5.8 to Figure 5.11 show the 45 degree tilted SEM images of 30 nm TiN mesh with diameter from 200 nm to 800 nm with varied pitch from 400 nm to 1000 nm VP-MacEtched with the fixed 0.28 M HF, 0.13 mM H_2O_2 and 0.39 M IPA at varied temperature of 50, 60, 80, and 90 °C for 5 minutes, respectively.

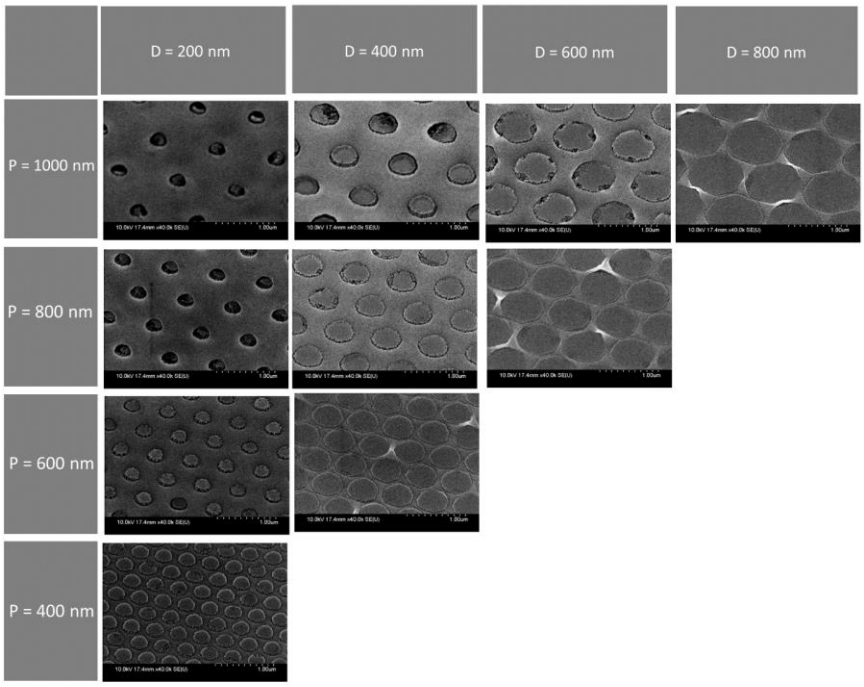

Figure 5.8: A 45 degree tilted SEM images of 30 nm TiN mesh with diameter from 200 to 800 nm with pitch from 400 to 1000 nm vapor phase MacEtched with 0.28 M HF, 13 mM H_2O_2, 0.39 M IPA at 50 °C for 5 minutes.

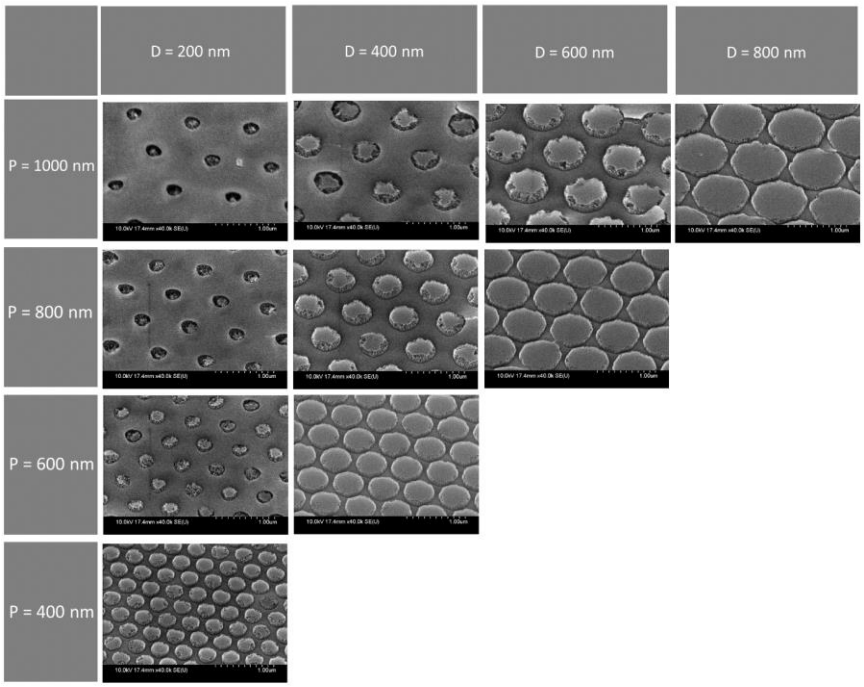

Figure 5.9: A 45 degree tilted SEM images of 30 nm TiN mesh with diameter from 200 to 800 nm with pitch from 400 to 1000 nm vapor phase MacEtched with 0.28 M HF, 13 mM H_2O_2, 0.39 M IPA at 60 °C for 5 minutes.

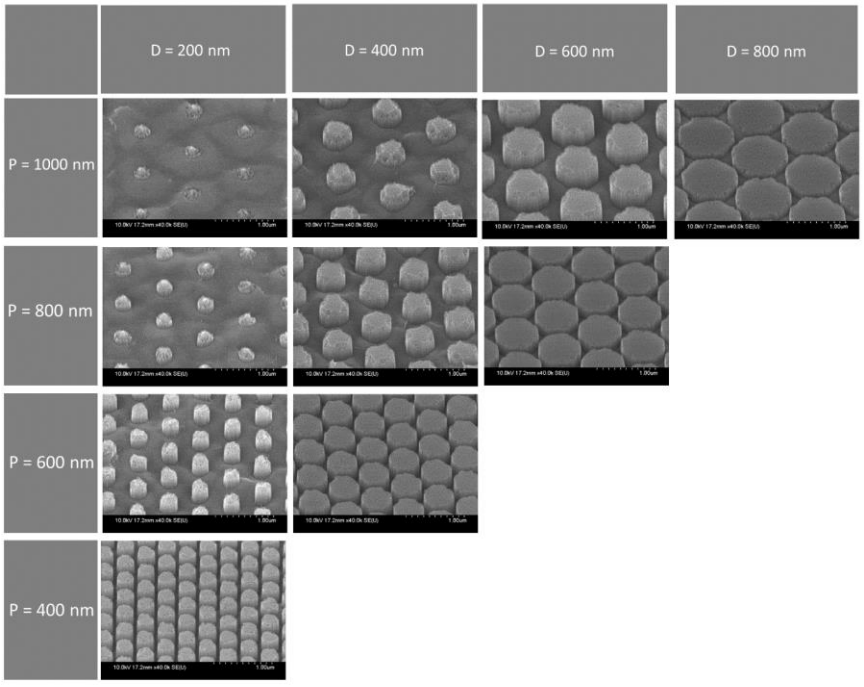

Figure 5.10: A 45 degree tilted SEM images of 30 nm TiN mesh with diameter from 200 to 800 nm with pitch from 400 to 1000 nm vapor phase MacEtched with 0.28 M HF, 13 mM H_2O_2, 0.39 M IPA at 80 °C for 5 minutes.

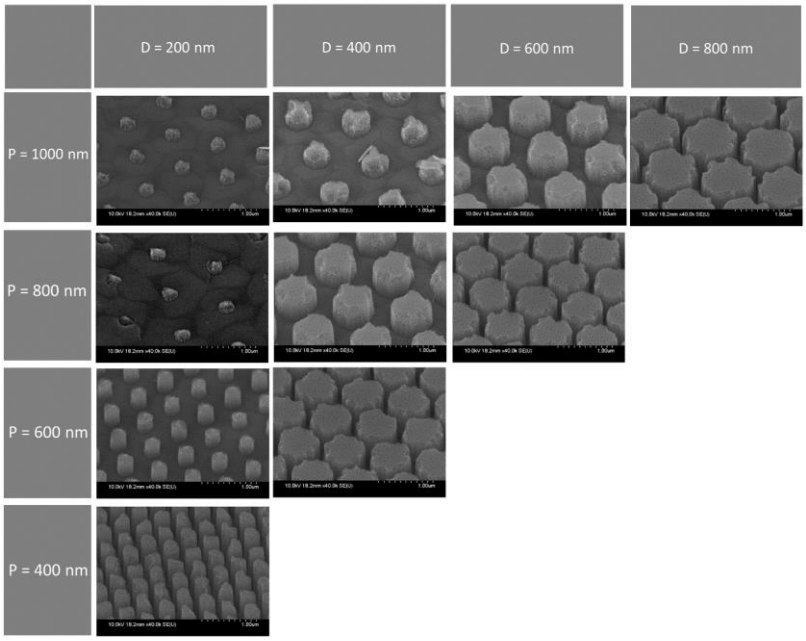

Figure 5.11: A 45 degree tilted SEM images of 30 nm TiN mesh with diameter from 200 to 800 nm with pitch from 400 to 1000 nm that were vapor phase MacEtched with 0.28 M HF, 13 mM H_2O_2, 0.39 M IPA at 90 °C for 5 minutes.

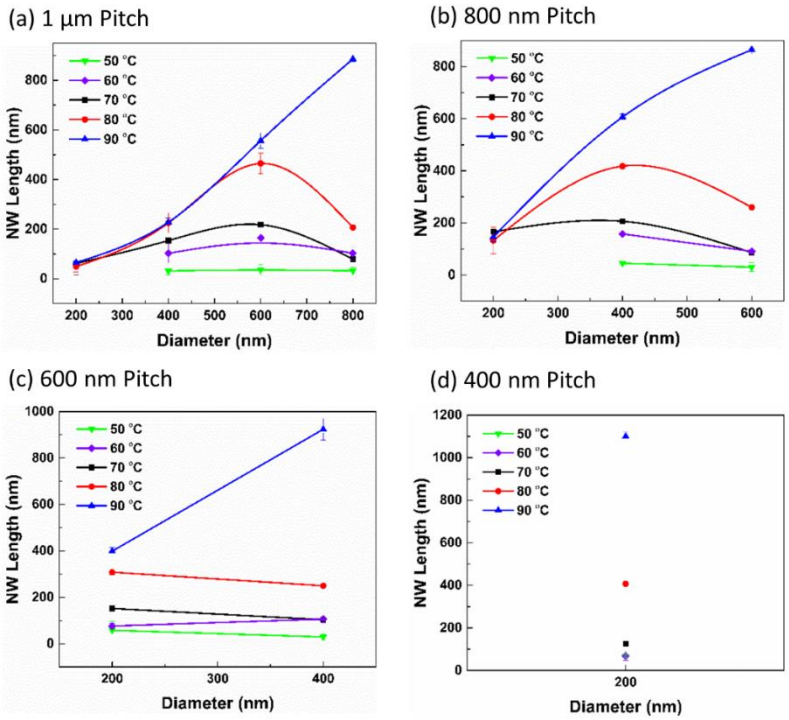

Figure 5.12: The average NW length as the function of mesh diameter from 200 to 800 nm at varied pitch of 1000, 800, 600, 400 nm VP-MacEtched with 13 and 32 mM H_2O_2 with fixed 0.28 M HF and 0.39 M IPA at 70 °C for 5 minutes.

Figure 5.12 (a) to (d) shows the average NW length as the function of mesh diameter from 200 to 800 nm at fixed pitch of (a) 1000 nm, (b) 800 nm, (c) 600 nm and (d) 400 nm, VP-MacEtched with 0.28 M HF, 13 mM H_2O_2, and 0.39 M IPA at varied etching temperatures from 50 to 90 °C for 5 minutes. For 1000 nm pitch, at 50 °C, average NW length stays as the constant value of ~30 nm for the diameter increases from 400 to 800 nm. As the temperature increases from 50 to 80 °C, the parabolic NW length trends appears. For 80 °C, the NW length increases from 50 to 460 nm as the diameter increases from 200 to 600 nm and it decreases to 210 nm as the diameter further increases to 800 nm. The NW length increases the most at 600 nm diameter (from ~30 to 460 nm). When the temperature further increases to 90 °C, the parabolic etching trend changes to linear such that the NW length increases with increasing mesh diameter. However, the NW length only increases for diameter from 600 to 800 nm; The NW length at the diameter from 200 and 400 nm is the same as the ones in 80 °C. The etching trend for temperature increasing from 50 to 80 °C can be divided in to three regions that are (i) 200 nm diameter where the NW length stays as constant value of 60 ± 9 nm with increasing temperature, (ii) 400 and 600 nm diameter where the NW length increases with increasing temperature and increasing diameter, and (iii) 800 nm diameter where the NW length increases with temperature but decrease with increasing diameter. The constant NW length at region (i) results from the limited MT via the large mesh spacing. The area of the oxidized Si under the TiN is significantly large such that the oxidized Si etch rate enhanced by increasing temperature is insufficient to increase the vertical etching.

The increase in NW length with increasing temperature and diameter at region (ii) is due to the balanced CG and MT. The enhanced oxidized Si etch rate with increasing temperature allows to completely etch away the oxidized Si to enable the vertical etching. The development of the

parabola peak (i.e. maximized NW length) at a 600 nm diameter indicates that formation of oxidized Si by CG and removal of the oxidized Si by MT are both at maximum.

The increase in NW length with increasing temperature but decrease with increasing diameter at region (iii) results from the limited CG. The number of holes injected by the CG is reduced by the increased diameter (decrease in TiN area) while the oxidized Si etch rate by MT is maximized by increasing temperature. Due to the limited amount of CG, there are insufficient volumes of oxidized Si to be etched to enhance the vertical etching.

The transition from the parabola to linear etching trend at 90 °C not only supports the enhanced CG at 800 nm diameter but also indicates the saturation of the MT enhancement with increasing temperature.

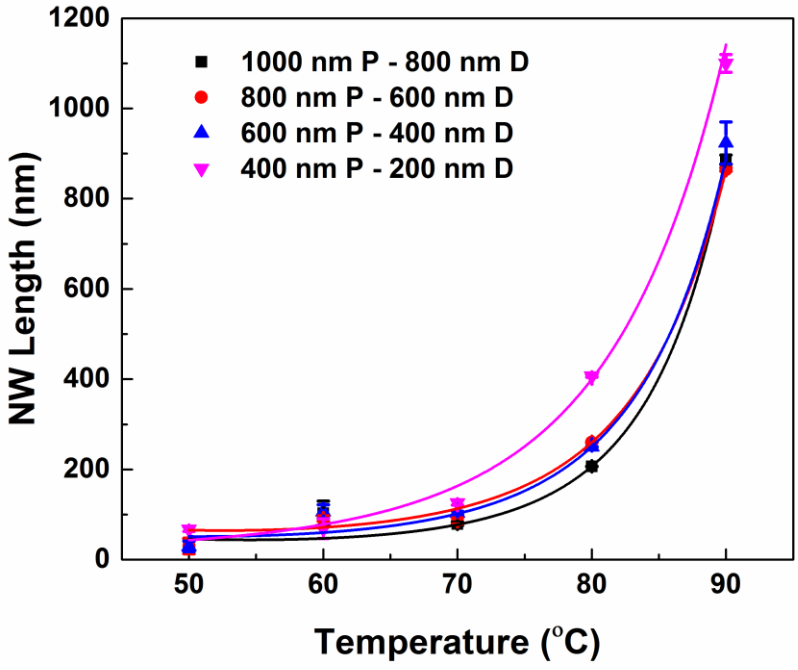

Figure 5.13: Average NW length as the function of etching temperature from 50 °C to 90 °C for 200 nm, 400 nm, 600 nm, and 800 nm at fixed spacing of 200 nm VP-MacEtched with fixed solution concentration of 0.28 M HF, 13 mM H_2O_2, and 0.39 M IPA for 5 minutes.

Figure 5.13 shows the average NW length as the function of etching temperature from 50 °C to 90 °C for fixed spacing of 200 nm for varied pitch of 400 nm, 600 nm, 800 nm and 1000 nm. The NW length exponentially increases with increasing temperature. The differences in NW length for fixed mesh spacing at different pitches are not significant.

The increase in NW length with increasing etching temperature again indicates that the MT is enhanced. The small difference in NW length for fixed mesh spacing indicates that the etching enhancement by the surface diffusion of the etching species is not significant even at high temperature. We believe that the effect of surface diffusion on etch depth can be observed in low etching pressure since the diffusion coefficient is inversely proportional to the pressure in the vapor phase. It is important to note that the exponential etching trend contradicts the one on Au/Si vapor phase MacEtch reported by Hildreth et al. where they observed the parabolic etching trend with the highest etching depth at 40 °C [34]. They described the parabola trend is resulted from the condensation of the adsorbed etchant species contributing the combination of LP- and VP-MacEtch. This parabolic etching trend resulted by the vapor condensation is also reported in the SiO_2 etching with vapor phase HF reported by Fukuta et al. [38]. Therefore, the exponential etching trend experimentally demonstrates that the modified VP-MacEtch of fixing identical temperature for the solution and substrate eliminates the LP-MacEtch.

5.7 TiN Thickness Dependence

Figure 5.14 and Figure 5.15 show the 45 degree tilted SEM images of 10 nm and 5 nm TiN mesh with diameter from 200 nm to 800 nm with varied pitch from 400 nm to 1000 nm VP-MacEtched with the fixed 0.28 M HF, 0.13 mM H_2O_2 and 0.39 M IPA at 80 °C for 5 minutes, respectively.

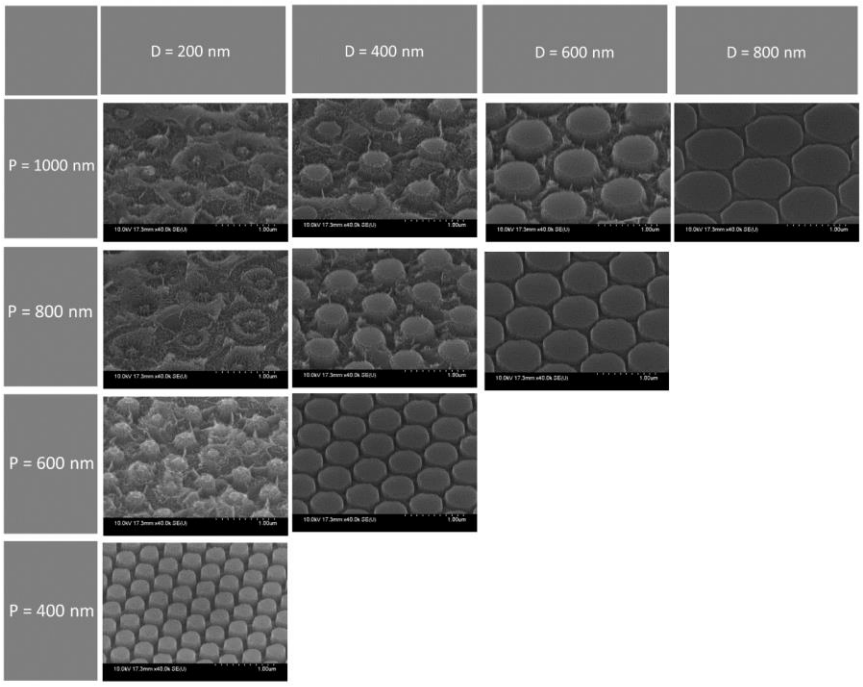

Figure 5.14: A 45 degree tilted SEM images of 10 nm TiN mesh with diameter from 200 to 800 nm with pitch from 400 to 1000 nm vapor phase MacEtched with 0.28 M HF, 13 mM H_2O_2, 0.39 M IPA at 80 °C for 5 minutes.

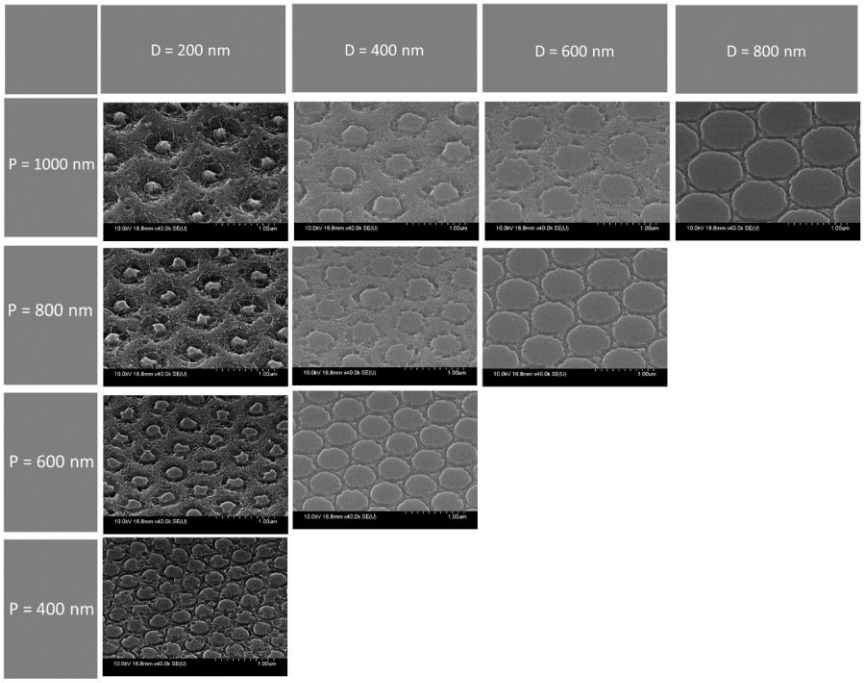

Figure 5.15: A 45 degree tilted SEM images of 5 nm TiN mesh with diameter from 200 to 800 nm with pitch from 400 to 1000 nm vapor phase MacEtched with 0.28 M HF, 13 mM H_2O_2, 0.39 M IPA at 80 °C for 5 minutes.

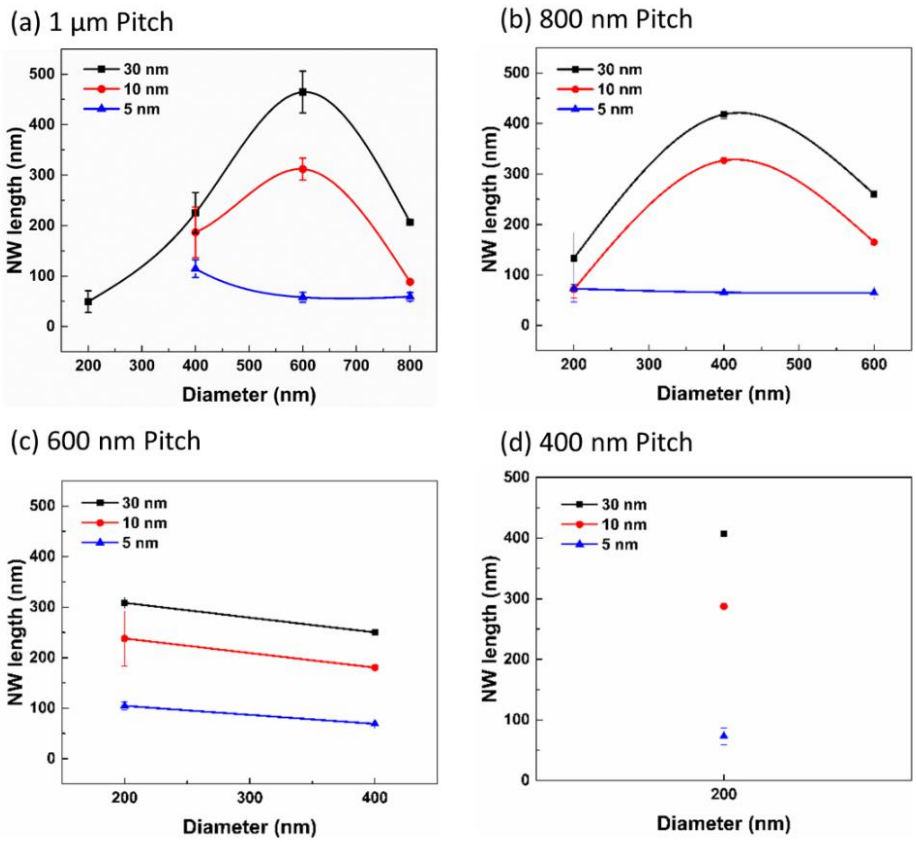

Figure 5.16: The average NW length as the function of the mesh diameter from 200 to 800 nm with varied TiN thickness of 5, 10 and 30 nm for pitch of (a) 1 um, (b) 800 nm, (c) 600 nm, and (d) 400 nm vapor phase MacEtched with fixed solution concentration of 0.28 M HF, 13 mM H_2O_2, 0.39 M IPA at 80 °C for 5 minutes.

Figure 5.16 shows the average NW length as the function of mesh diameter from 200 to 800 nm at fixed pitch of (a) 1000 nm, (b) 800 nm, (c) 600 nm, and (d) 400 nm for TiN thickness of 30, 10, 5 nm VP-MacEtched with 0.28 M HF, 13 mM H_2O_2 and 0.39 M IPA at 80 °C for 5 minutes. For 5 nm TiN, the NW length decreases from 110 nm to 60 nm as the diameter increases from 400 to 800 nm.

As the thickness increases to 10 nm, a parabolic trend appears. The NW length is the highest at a 600 nm diameter. As the thickness increases to 30 nm, etch rate in every diameter increases but the parabolic trend is still shown. Note that for 5 and 10 nm TiN, the mesh TiN is cracked or delaminated for the diameter smaller than 400 nm.

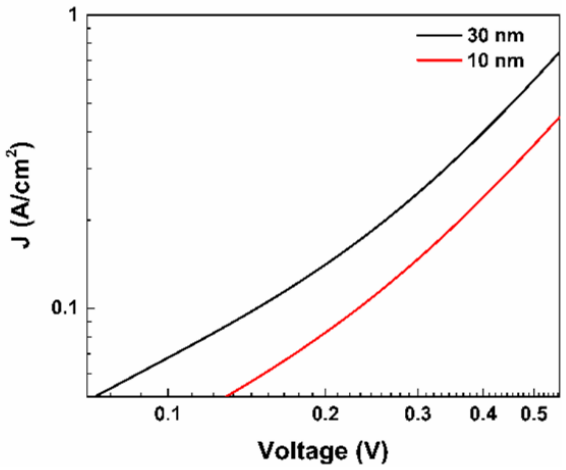

Figure 5.17: The measured current density as the function of the biased voltage from 0 to 0.6 V in log scale for 10 and 30 nm TiN on p-type substrate.

The increase in NW length with increasing TiN thickness is the result of the change in conductivity. Figure 5.17 shows the current density as the function of the biased voltage from 0 to 0.6 V in log scale for 10 and 30 nm TiN on same p-type substrate showing its quasi-ohmic contact.

The current density increases as the TiN thickness increases from 10 to 30 nm. This is due to the increase in barrier height from the change in TiN work function. This explains that the increase in the NW length with increasing TiN thickness observed in Figure 5.16 is due to the increase in a hole injection rate by a higher conductivity via lower barrier height.

The crack and delamination of the 5 and 10 nm TiN for the diameter smaller than 400 nm indicates that the thinner TiN cannot overcome the film stress of uneven etching from limited MT because of the high Young's modulus.

6. GALLIUM PHOSPHIDE MACETCH WITH AU CATALYST

The MacEtch of the III-V compound semiconductor material is an important process technology that can be used to solve the problems of the dry etching process in III-V electronic and optoelectronic applications. By reducing the sidewall roughness, the nonradiative recombination and scattering induced by the defects can be minimized.

The first demonstration of the GaAs was reported by Dejarld et al. [39], and the demonstration of the MacEtched GaAs pillar array based light emitting diode (LED) was reported by Mohseni et al. [40]. Both works showed that the GaAs could be MacEtched to form the high aspect ratio structure that can be used to enhance the device performance.

The first demonstration of the GaP MacEtch is reported by Kim et al. [41]. They used the n-type GaP with Pd as the catalyst. The mesh patterned Pd was MacEtched with the solution of HF and H_2O_2 and produced the GaP nanocone array. They described the anode reaction of GaP MacEtch as

$$GaP + nh^+ + 3H_2O \rightarrow Ga^{3+} + H_3PO_3 + 3H^+ + (6\text{-}n)e^- \quad (6.1)$$

The drawback of Pd catalyst is that the Pd gets dissolved by HF, thus the MacEtch duration is limited by the etch rate of the MacEtch solution. In this section, the GaP MacEtch using the Au catalyst is presented.

The Zn doped p-type GaP (100) substrates were used for the experiment. First, the native oxide in GaP substrate was etched in 1:3 = H_2SO_4:H_2O_2 for 10 min. Next, mesh patterned Au with thickness of 10 nm was deposited on the GaP substrate after patterning with various types of lithography (optical, nanosphere and e-beam lithography). Then, the samples were MacEtched in the solution mixture of HF and H_2O_2.

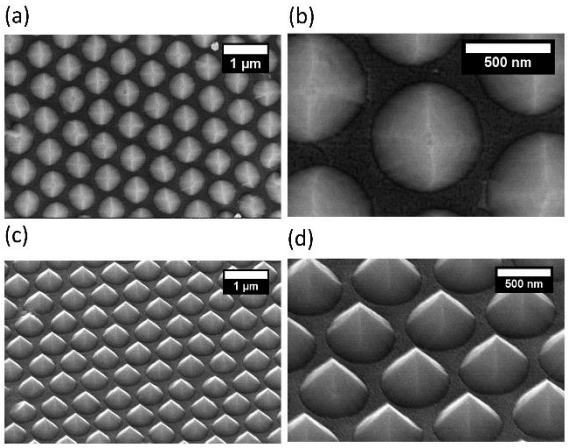

Figure 6.1: (a) and (b) show the low- and high- magnification top view SEM images, (c) and (d) show the low and high magnification 45 degree tiled SEM images of GaP pyramidal texture fabricated by MacEtch.

Figure 6.1 (a), (b) show the low- and high-magnification top view SEM images and (c), (d) show low- and high- magnification 45 degree tilted SEM images of the mesh patterned Au on GaP prepared by nanosphere lithography, MacEtch in 0.28 M HF and 0.065 M H_2O_2 for 1 hr. The images show the pyramidal textures are produced by the forward MacEtch. The pyramidal texture array resulted from the slow etch rate of the GaP; the band gap of the GaP (2.25 eV) is larger than the band gap of the Si (1.1 eV) such that the hole injection to produce the oxidized GaP and dissolution of the oxidized GaP are slower than the one in Si substrate.

The pyramidal texture indicates that the etching is limited by the MT. The holes are continuously injecting while the GaP under the catalyst is slowly etching. The unconsumed holes diffuse on the surface of etched pillars resulting in the oxidation and dissolution of the bare GaP. This chemical etching process is crystallographic orientation dependent. Top view SEM images in Figure 6.1 (a) and (b) show that the etched pyramidal array has four facets that correspond to the (111)-A and (111)-B planes.

The chemical etching of the etched pillar indicates that the GaP MacEtch is influenced by both forward and inverse MacEtch (i.e. intermedicate MacEtch). This intermediate MacEtch can be changed to either complete forward or inverse MacEtch by enhancing or limiting MT.

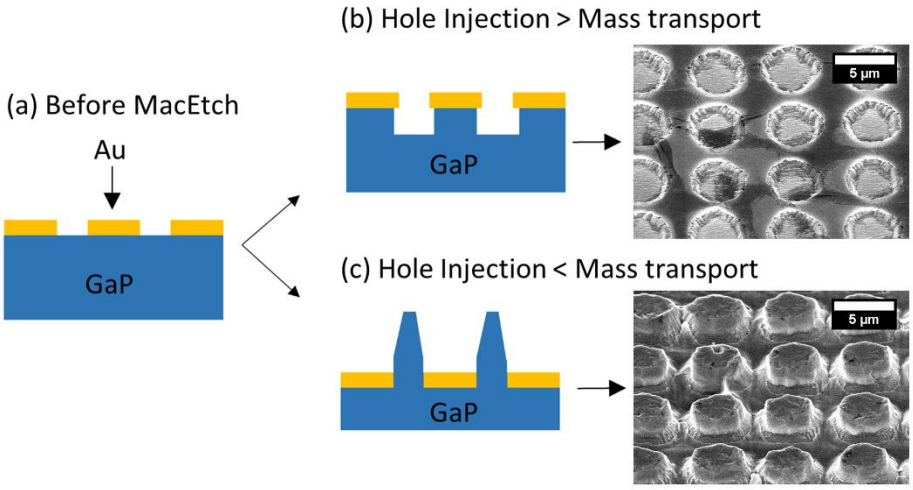

Figure 6.2: (a) GaP sample before MacEtch. (b) schematic (left) and SEM image (right) of inverse MacEtched GaP when the hole injection is greater than the mass transport. (c) Schematic (left) and SEM image (right) of forward MacEtched GaP when the mass transport is greater than the hole injection.

Figure 6.2 (a) shows the cross-section schematic of the mesh patterned Au deposited on the GaP. Figure 6.2 (b) left and right images illustrate and the corresponding tiled SEM images of the inverse MacEtched GaP when the MT is limited. In this case, the hole injection and diffusion are faster than the removal rate of the GaP under the catalyst such that the bare GaP (off metal regions) are chemically etched. Figure 6.2 (c) left and right images illustrate the corresponding tiled SEM images of the forward MacEtched GaP when the MT is enhanced. In this case, hole injection and diffusion are slower than the removal rate of the GaP such that the chemical etching on the bare GaP regions are quenched by minimizing the diffusion of the unconsumed holes.

As discussed in the previous chapters, MT can be enhanced by reducing the volume of the GaP under the catalyst by decreasing the catalyst area.

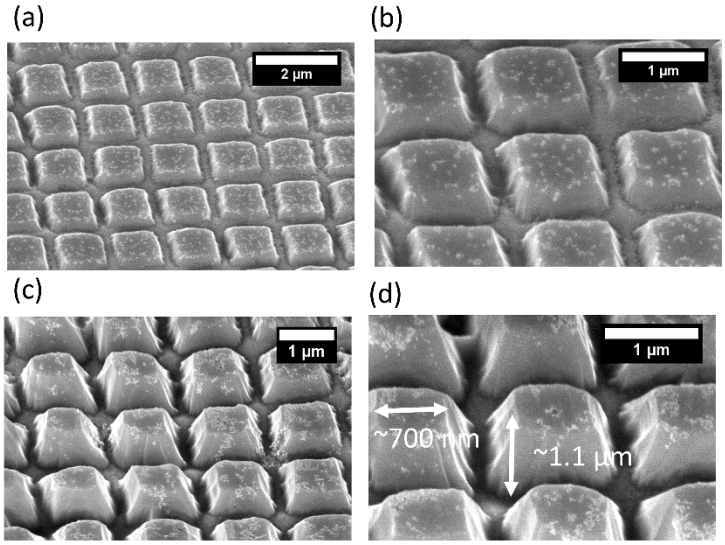

Figure 6.3: The 45 degree tilted SEM images of the sub-micron pillar array fabricated by MacEtch in (a), (b) low oxidant concentration, and (c), (d) high oxidant concentration.

Figure 6.3 (a) and (b) show the tilted SEM image of the sample with Au mesh with 800 nm x 800 nm square and 200 nm spacing patterned with e-beam lithography, MacEtched in 0.28 M HF and 0.065 M H_2O_2 for 1 hr, and Figure 6.3 (c) and (d) show the same sample MacEtched in the 0.28 M HF and 0.13 M H_2O_2 for 1 hr.

Images shows that the chemical etching of the etched GaP pillars are significantly reduced as compared to the images shown in previous figures. It is important to note that the spacing of the mesh is similar to one shown in the mesh prepared by the nanospher lithography shown in Figure 6.1, but the chemical etching is much reduced. This is because the uniformity of the mesh in nanospher lithography is poor such that any of the non-uniform area (region where there is no mesh) is anchoring the catalyst preventing it from vertically sinking down.

7. CONCLUSION

In this dissertation, the background of Metal-assisted Chemical Etching (MacEtch) was reviewed. Then, the fabrication of sub-micron scale crystalline silicon (c-Si) via array was discussed. The systematical analysis of vertical etch rate as the function of catalyst diameter, pitch and spacing experimentally demonstrated the influence of carrier generation (CG) and mass transport (MT) in MacEtch. Using the experimental data, the empirical vertical etch rate model was made to simulate the etching behavior at the extreme etching condition where the CG or the MT is dominating. With the guidance of experimental and simulation data, the sub-micron closely packed a high aspect ratio via array of 320 nm diameter, 80 nm spacing and aspect ratio larger than 10 was fabricated. Next, the sub-micron scale polycrystalline Si via array was demonstrated by Self-Anchored Catalyst (SAC) MacEtch. The catalyst delamination and detouring resulted from the even etch rate originated from the poly grain and grain boundaries were minimized by anchoring the catalyst with nanowires formed through the porous catalyst. The vertical etch rate as the function of the catalyst diameter at fixed pitch also demonstrated that the MT is enhanced by an increased liquid path with SAC-MacEtch. The SAC-MacEtch was also applied to stacked Poly-Si/SiO2 via array, large scale though Si via array and GaAs via array to overcome the non-uniform etching from limited-MT. Next, the first demonstration of CMOS-compatible titanium nitride catalyst MacEtch was demonstrated. The inverse MacEtch observed in the conventional liquid phase MacEtch was switched to forward MacEtch by using the modified vapor phase MacEtch. The mesh patterned TiN was vapor phase MacEtched and the length of the produced NW arrays were analyzed as the function of mesh dimension, etching temperature and TiN thickness. Next, GaP MacEtch using the Au catalyst and solution mixture of HF and H_2O_2 was

demonstrated. Etching result showed that the inverse and forward MacEtch can be controlled by the enhancing or limiting the MT.

8. FUTURE WORK

In this chapter, the future directions of the MacEtch works are discussed. In Section 8.1, a schematic and description of the proposed low pressure vapor phase MacEtch reactor is described. In Section 8.2, the idea of fabricating multi-stacked InGaAs inverse quantum dot array by III-V MacEtch is described. In Section 8.3, the idea of graphene assisted chemical etching of the GaAs is described.

8.1. Low Pressure Vapor Phase MacEtch Reactor

In Chapter 5, the modified vapor phase MacEtch is demonstrated to fabricate the nanowire arrays with mesh patterned TiN catalyst. The results showed that the advantage of enhancing the mass transport (MT) in vapor phase allows to make the transition from inverse to forward MacEtch. However, there are still limitations in the vapor phase MacEtch setup that could be improved to achieve not only the enhanced-MT but also the etching uniformity. In the setup described in the previous chapter, the solution is dispersed on the sacrificial Si substrate near the MacEtch sample using the pipette such that the location where the solution is dispersed is inconsistent which can result the etching condition variation within the sample surface. Also, etching is performed in the atmosphere such that the diffusion of vapors can be interrupted by the external sources such as humidity and wet bench air circulation setup. More importantly, the etching only take place in the atmospheric pressure which makes it difficult to observe the etching result in low pressure. As the result, it is necessary to come up with the reactor which can precisely control the direction and amount of the reacting vapor and minimize the disturbance from the external environmental sources.

Figure 8.1 shows a proposed schematic of low pressure vapor phase MacEtch reactor setup. The reactor is composed of a chamber and multiple vapor lines. The chamber consists of a

hemispherical SiC chamber, a SiC base substrate and a heater. The vapor lines consist of four Teflon vaporizers with acid (HF), oxidant (H_2O_2) and surfactants (IPA, DI) connected to the nitrogen (N_2) carrier gas lines which the amount of N_2 supplied is controlled by the individual mass flow controller (MFC).

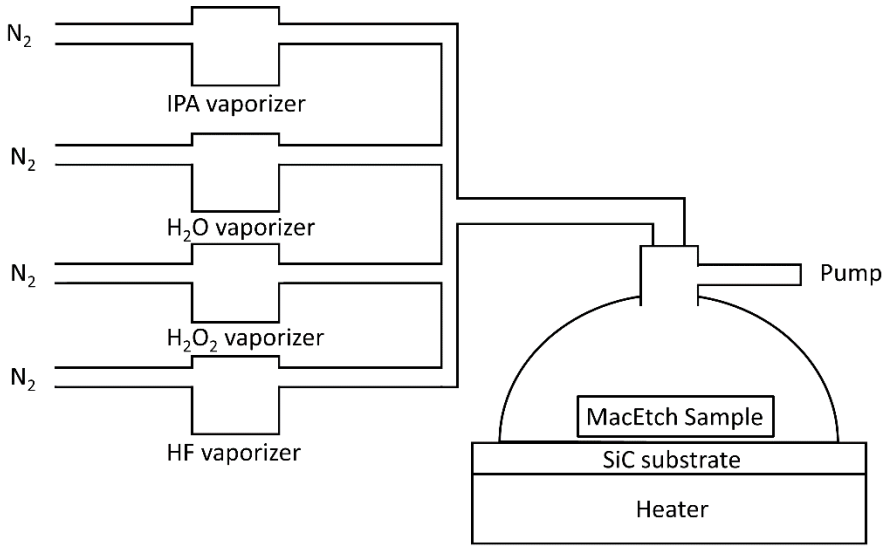

Figure 8.1: Proposed schematics of low pressure vapor phase MacEtch reactor.

The MacEtch sample is placed on the SiC base substrate. Then the hemispherical SiC chamber is placed on top of the SiC base substrate. The MacEtch sample is heated to the desired temperature through the heater under the SiC base substrate. The pressure of the chamber is controlled by the pump connected on the hemispherical SiC chamber. HF, H_2O_2, IPA and DI in the vaporizers are heated to the specific temperatures to produce the vapors. The produced vapors are carried by the nitrogen carrier gas to the main chamber. The MacEtch occurs as the mixture of the vapor species reach the sample surface. Once the etching is finished, only the H_2O vapor is supplied to rinse the sample and the main chamber.

The concentration of the MacEtch vapor mixture can be controlled by the amount of the vapor produced by the set temperature of the vaporizers and the flow rate of N_2 carrier gas that is

controlled by the MFCs. Because the vaporizing condition for HF, H_2O_2, DI and IPA are different, using the individual vaporizing line will allow precise control of the amount of the produced vapor and final vapor mixture concentration that reaches on the sample surface. The pressure of the main chamber can be controlled such that the VP-MacEtch can be done under the low pressure. This will give another degree of freedom to control the MT of etchant and byproducts.

The vertical etch rate as a function of the vapor concentration, substrate and vapor temperature, and the etching pressure need to be characterized. With the systematically calibrated etching conditions, this setup may solve the limitations in the conventional vapor phase MacEtch to increase the etching quality.

8.2. Multi-Stacked Inverse Quantum Dot (MIQD) Using III-V Via MacEtch

In this section, the idea of fabricating the multi-stacked InGaAs Inverse Quantum Dot (IQD) using III-V MacEtch is discussed. Also, the idea of fabricating and characterizing the multi-stacked InGaAs IQD intermediate band gap photovoltaic is presented. In Section 8.2.1, the background of IQD is presented. In Section 8.2.2, fabrication and characterization of the InGaAs IQD intermediate band gap photodiode using conventional RIE dry etching is presented. In Section 8.2.3, the idea of fabricating and characterizing the multi-stacked IQD structure by III-V via MacEtch is presented.

8.2.1 Inverse Quantum Dot (IQD)

The IQD is a periodically perforated QW with the pores refilled by wider band gap materials [42]. Figure 8.2 shows the schematics of the IQD structure. The active layer of the IQD can evolve from a QW-like to a QD-like structure by tuning the diameter of the pores and the pitch

of the IQD array. Unlike the conventional QDs, the confined region in the IQD is normally connected to its neighbors, which allows the IQDs to share the same carrier pool instead of interacting via tunneling. This eliminates the spatial isolation and reduces the inhomogeneous broadening which typically occurs for the self-assembled QDs with non-uniform size.

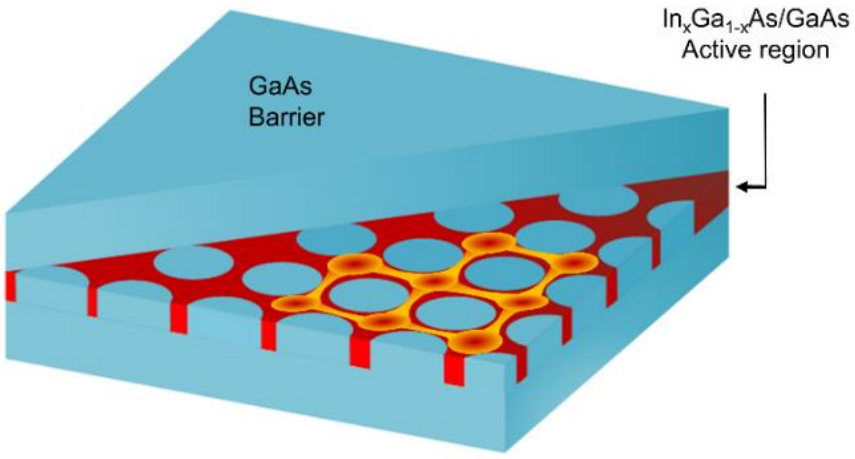

Figure 8.2: Tiled cross-sectional schematic of the IQD structure.

When the pore diameter of IQD reaches the critical value where the device starts to exhibit characteristics of a 0D-structure, discrete-energy sub-bands begin to form in both the conduction and the valence bands. The separation between these sub-bands increases with the pore diameter due to the stronger spatial confinement. The detailed parametric study and the optical characteristics of the IQD were reported separately [25, 42].

8.2.2 InGaAs IQD Intermediate Band Gap Photodetector

Figure 8.3 shows the energy band diagram that illustrates the primary physical processes that contribute the photocurrent generation in the IQD-based IB photodetector. We designed the device so that $k_BT < E_C - E_{C2}$ (~0.05 eV) at room temperature, which allows us to simplify the

discussion by ignoring the thermal excitation of the electrons from the conduction IBs to the continuum. This ensures that the photocurrent could only be generated when both the primary and the secondary sources are applied, and allows us to identify the enhancement of photocurrent generation from each IB when the quantization become stronger by increasing the pore diameter of the IQD. Due to the selection rules between the IBs [42], photons from the primary light source, $\hbar\omega_1$, will only trigger transition of the electrons from the valence IB to the conduction IB with the same quantum number. However, once the electrons are in the higher conduction IB, they are allowed to thermally relax down to a lower conduction IB.

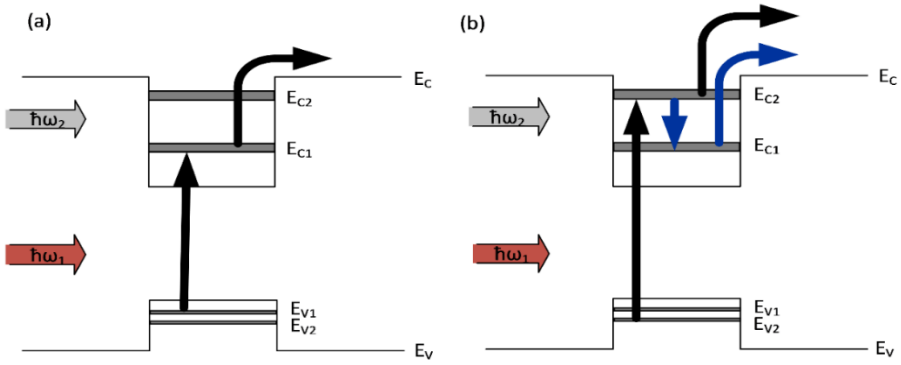

Figure 8.3: Energy band diagram illustrating the photocurrent generation in IQD when (a) the electrons in the first IB are excited to the first conduction IB with the primary light and the excited electrons in the first conduction IB are excited to the conduction band of the barrier with the secondary light, and (b) the electrons in the second valence IB are excited to the second conduction IB with primary light and the excited electrons in second conduction IB and relaxed electrons in the first conduction IB are excited to the conduction band of the barrier with secondary light.

The total photocurrent generated by the device depends on the carrier relaxation time and the number of IBs. The longer the carrier relaxation time, the longer electrons will be trapped in a conduction IB. On the other hand, more IBs will increase the number of available states for the electrons in the higher energy state to relax down to and, in turn, increase the probability for electrons to stay in the excited states. Therefore, the efficiency of the photocurrent generation can be maximized by increasing the carrier relaxation time and the number of the IBs. In an IQD

structure, the number of IBs can be increased by choosing the base QW with a higher potential barrier, while the carrier relaxation time can be increased by enhanced quantization via increasing the pore diameter and decreasing the pitch.

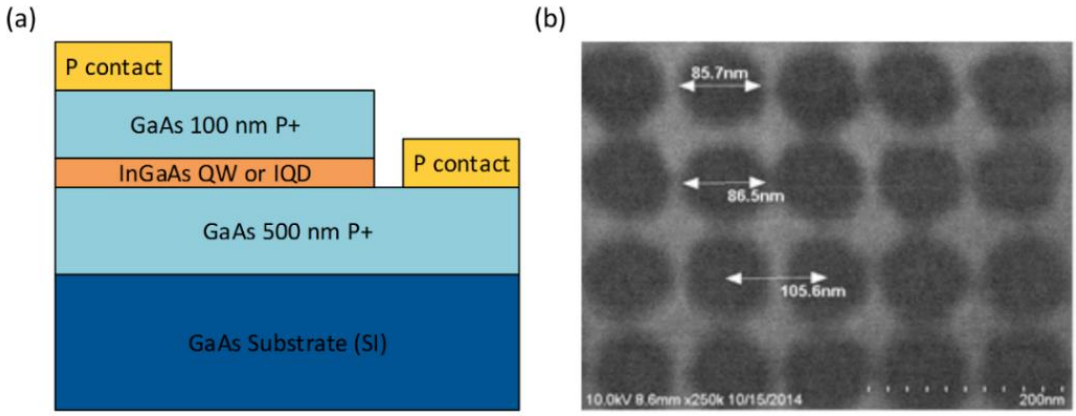

Figure 8.4: (a) Cross-section schematic of the QW and IQD IB photodetector, (b) SEM images of pattern transferred on QW showing IQD with pore diameter of 86 nm.

We fabricated the p-type QW and IQD photodetector with top and bottom contacts, as shown in Figure 8.4 (a). The IQD was designed to have two excited states at 1010 nm and 940 nm by using $In_{0.2}Ga_{0.8}As$ QW as the active layer. The base structure was grown on the semi-insulating (100) GaAs substrate using metal-organic chemical vapor deposition (MOCVD). The base structure consists of a 500 nm P+ GaAs bottom contact layer, an 8.6 nm $In_{0.2}Ga_{0.8}As$ QW, and a 5 nm GaAs capping layer. After the base structure growth, 20 nm SiO_2 was deposited as the hard mask using PECVD. Then, PMMA was spin-coated and the IQD arrays were patterned using the e-beam lithography. The PMMA was developed with 1:3 IPA to MIBK. Then, the patterns were transferred to the SiO_2 using BOE. After the PMMA removal, patterns in SiO_2 were transferred to QW using $SiCl_4$ RIE. The SiO_2 was then removed with BOE.

Square ordered IQDs with diameters of 61 nm, 73 nm, 81 nm, 86 nm, 89 nm, and 92 nm were fabricated. The pitch was fixed to 100 nm for all devices. The average pore diameter was determined using image analysis. The offset of the patterned pore diameter was ±5 nm. Figure 8.4 (b) shows the SEM image of IQD with an 86 nm pore diameter. After the IQD array was fabricated, a 100 nm P+ GaAs top contact layer was regrown using MOCVD. The bottom contact layer was exposed using optical lithography and $SiCl_4$ RIE. The top and the bottom contacts were defined, and metals with 10 nm Ti, 10 nm Pt, and 150 nm Au were deposited.

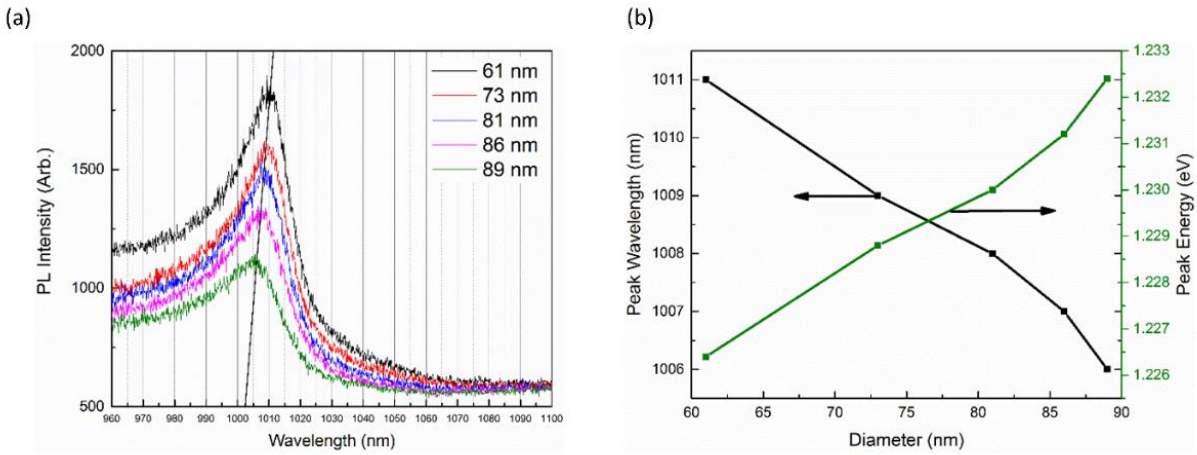

Figure 8.5: (a) Photoluminescence (PL) spectrum of the IQDs with 61 nm, 73 nm, 81 nm, 86 nm, and 89 nm at fixed pitch of 100 nm, (b) ground state peak wavelength, energy shift as a function of the IQD pore diameter.

The room temperature photoluminescence (PL) of the IQDs with diameters of 61 nm, 73 nm, 81 nm, 86 nm, and 89 nm were measured using Renishaw Micro PL system which uses 633 nm laser, focused with 50x objective lens, and the spectrums are shown in Figure 8.5 (a). The peak in the PL spectrum corresponds to the ground state of the corresponding IQD. The PL intensity of the ground state reduces as the IQD pore diameter increases. This could be attributed to the reduced total volume of the InGaAs active material with increased in the IQD pore diameter. Figure 8.5 (b) shows the wavelength and the energy shifts with increasing IQD pore diameter. The peak

wavelength of the ground state monotonically blue-shifts by 6 nm as the pore diameter increases from 61 nm to 89 nm due to the enhancement in lateral carrier confinement, which agrees with the IQD PL measurement reported in the previous publication [43].

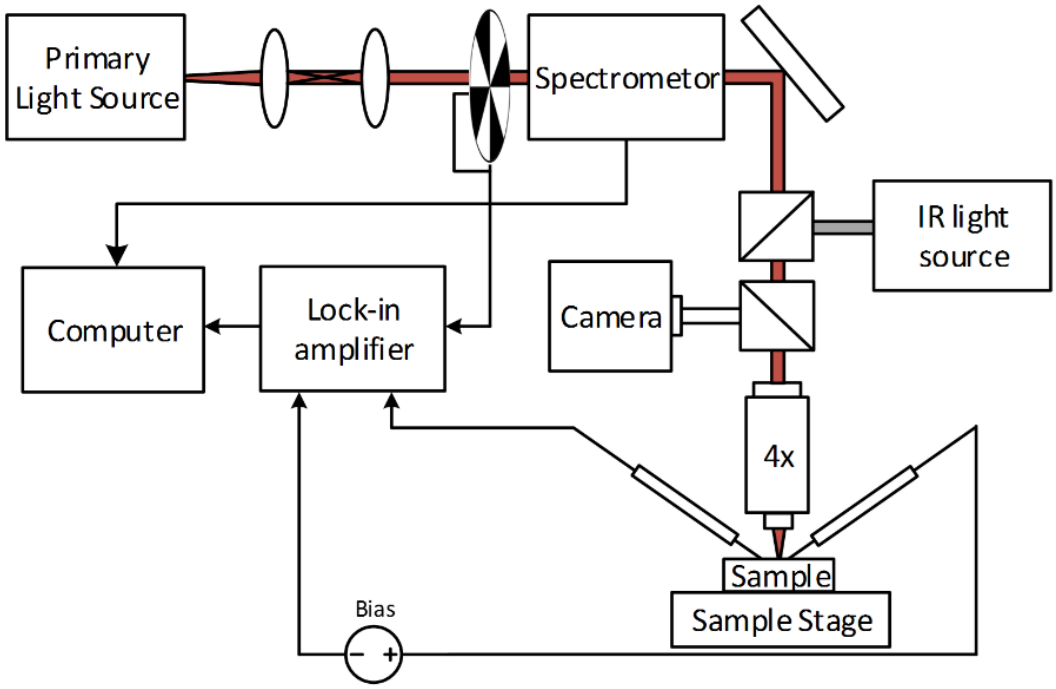

Figure 8.6: Photocurrent measurement setup schematic.

Figure 8.6 shows the photocurrent measurement setup. We used two different light sources to study the photocurrent generation in the IQD-based IB photodetector, similar to the one reported by Marti et al. [44] in 2006. The primary light source was a 20 W halogen light bulb. It was collimated before passing through the monochromator which allows the incident wavelength to be tuned from 850 nm to 1100 nm. It can excite the electrons from the valence IB to the conduction IB. The primary light was chopped to facilitate lock-in detection. It was then focused with a 4x Edmund objective lens with N.A. = 0.1 onto the sample. The reflected light passed through a 50%

beam splitter and was collected by an IR camera for monitoring. The beam spot size was approximately 300 µm which covered the entire area of an individual device. The secondary light source is an IR one with spectral range of 1 µm to 20 µm, which was filtered by a low-pass filter with cutoff wavelength at 4 µm to only excite the electrons from the conduction IBs to barrier conduction band to facilitate the photocurrent generation and collection. The photocurrent was measured with the two probe tips contacting with the top and the bottom contacts while the sample was biased at 10 mV. The photocurrent data were measured using a lock-in amplifier to minimize the background noise.

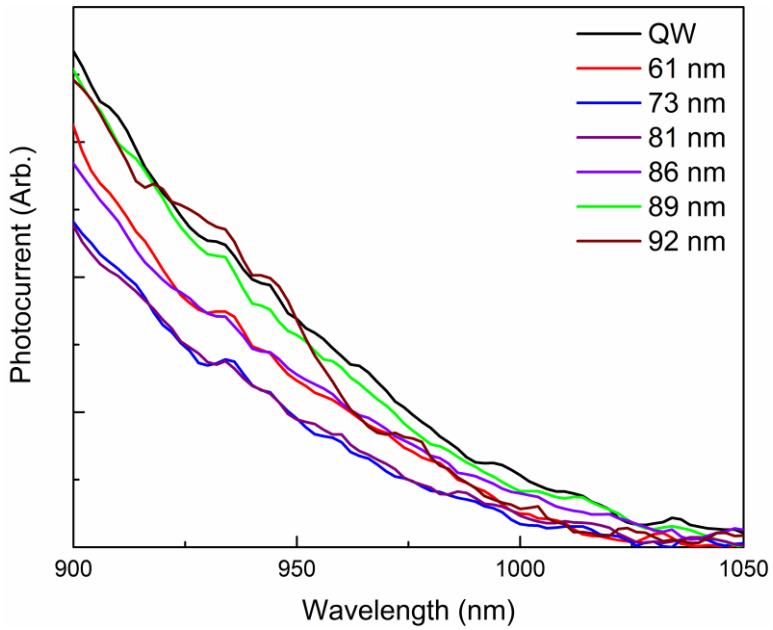

Figure 8.7: Photocurrent spectrum of the QW device and IQD devices with various diameters at fixed pitch of 100 nm.

Figure 8.7 shows the photocurrent spectra of the IQD devices and the QW (as a benchmark) measured by sweeping the wavelength of the primary light source from 900 nm to 1050 nm while keeping the secondary IR light always on. The measured photocurrent monotonically decreases when the IQD pore diameter increases from 61 nm to 73 nm, which indicates that, for these pore

diameters, the lateral confinement is not strong enough to induce a measureable quantization effect and these devices still behave like QW-like material. The reduction in measured photocurrent can be attributed to the decreased total volume of the active InGaAs material with increasing IQD pore diameter. However, the measured photocurrent stops decreasing when the IQD pore diameter reaches 81 nm and it reverses the trend to increase as the diameter goes from 81 nm to 92 nm. Such an increase in the photocurrent is a clear manifestation of the quantization effect and the formation of IBs originated from the lateral carrier confinement. Even though the total volume of the active material keeps decreasing, the formation of IB allows the available states to be concentrated in a much narrower spectral range and hence results in an enhanced photocurrent generation within that spectral region. The net photocurrent of the IQD with a diameter from 81 nm to 89 nm is still smaller than the photocurrent of the QW device. This indicates that the additional photocurrent generated is still surpassed by the photocurrent reduction from reduced InGaAs volume. However, net increase in the photocurrent of the IQD compared to that of the QW can be observed for IQD with a 92 nm diameter at a spectral range between 925 nm to 950 nm. As the IQD pore diameter approaches the pitch, the device behaves like a 0D-structure. The enhancement in photocurrent generation is due to the formation of delta-like density of state (DOS).

Figure 8.8 (a) to (e) show the simulated joint DOS of IQD with the pore diameter of 50 nm, 60 nm, 70 nm, 80 nm, 90 nm, and at a fixed pitch of 100 nm respectively. For the 50 nm diameter, the DOS of first excited state exhibits the delta-like DOS, but the ones in the second and third excited states are overlapped, forming a single continuous band. As the diameter increases to 95 nm, the peak DOS of the first excited state increases from 4.29×10^{19} $cm^{-3}eV^{-1}$ to 1.65×10^{20} $cm^{-3}eV^{-1}$, and it is blue shifted by 3 nm. It is also important to note that the DOS of the third excited

state is separated from the second exited state, and starts to form in 965 nm from 70 nm diameter.

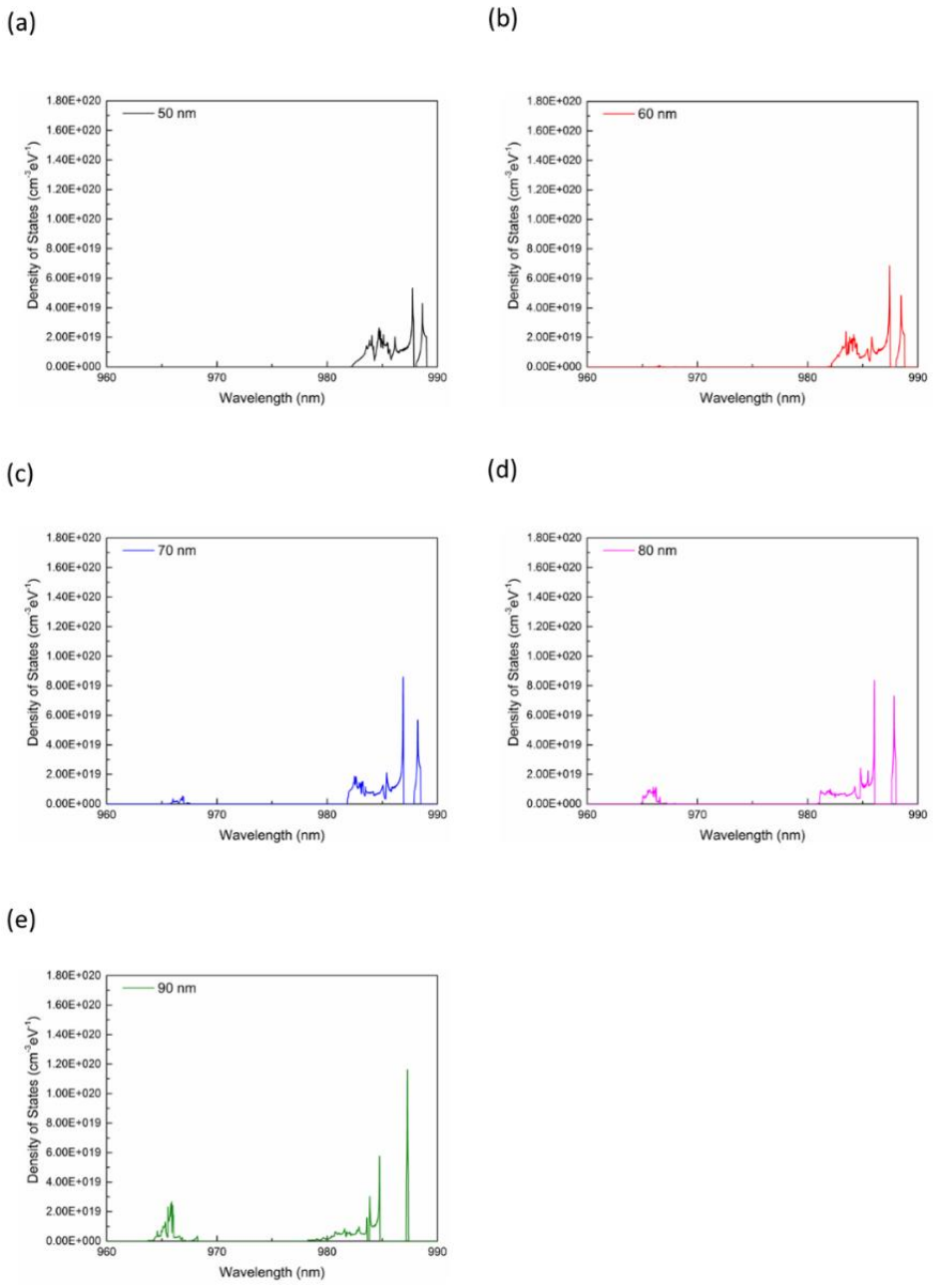

Figure 8.8: Simulated joint density of states of IQD with (a) 50 nm, (b) 60 nm, (c) 70 nm, (d) 80 nm, and (e) 90 nm diameters at fixed pitch of 100 nm.

The peak DOS of the third excited states increases to 2.662×10^{19} as the pore diameter increases to 90 nm, and the overlapped DOS in the second excited state decreases, forms the delta-like DOS.

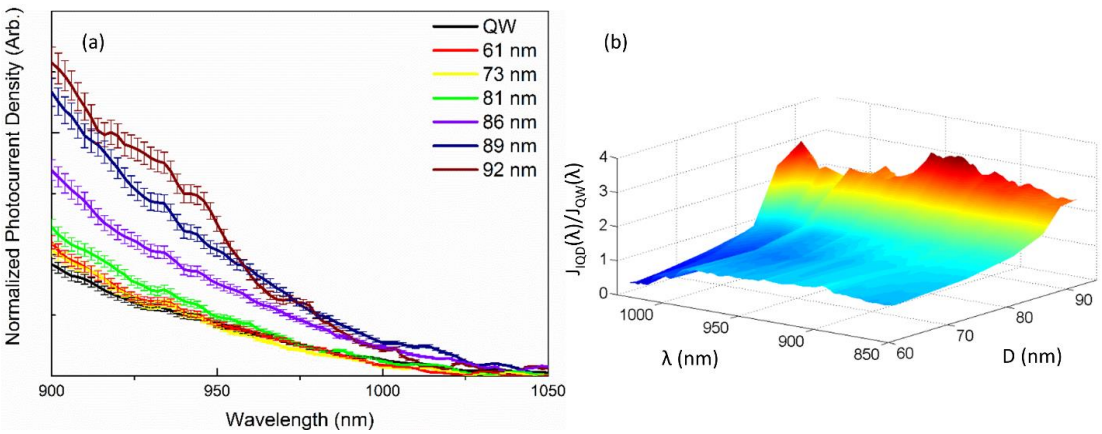

Figure 8.9: (a) Photocurrent density of IQD device with various diameters and 100 nm pitch, (b) $J_{IQD}(\lambda)/J_{QW}(\lambda)$ as function of the primary light source wavelength and the IQD pore diameter.

Figure 8.9 (a) shows the PCD of the QW and the IQD devices, J_{QW} and J_{IQD}, with pore diameters of 61 nm, 73 nm, 81 nm, 86 nm, 89 nm, and 92 nm. A pore diameter offset of ±5 nm was applied to the PCD spectra. The PCD of IQD devices with 61 nm and 73 nm pore diameters do not increase as compared to the QW device. As described in the previous paragraph, photocurrent generated from IBs in IQD with 61 nm and 73 nm pore diameters are minimum due to the insufficient lateral confinement. The PCD increase by 20% to 30% when the diameter of the pore increases to 81 nm. This indicates that additional photocurrent is generated from the IBs due to the stronger lateral confinement. The PCD continues to increase monotonically as the pore diameter increases to 92 nm.

Figure 8.9 (b) shows the PCD enhancement of IQD devices, J_{IQD}/J_{QW}, as a function of the wavelength of the primary light and IQD pore diameter. The enhancement of the IQD with a 61 nm pore diameter is less than 1 when the wavelength is longer than 1000 nm. This indicates that the number of the electrons generating the photocurrent is reduced as compare to the QW when the IQD pore diameter is small and lateral confinement is relatively weak. We believe that this is attributed to the increased non-radiative recombination via phonon scattering originated from perturbation to lattice structure of the InGaAs by the pores and the crystal defects produced in the

regrowth process acting as the scattering sites. The J_{IQD}/J_{QW} increases as the wavelength of the primary light source blue-shifts since the carriers being excited to the conduction IBs have higher kinetic energy and are more likely to be excited to the continuum, and as a result, the number of the electrons contributing to the photocurrent generation starts to dominate over that of the carriers being scattered by the IQD lattice.

The J_{IQD}/J_{QW} monotonically increases as pore diameter of IQD increases from 61 nm to 92 nm, and the enhancement is the highest at the wavelengths of 1010 nm and 940 nm. Two main factors contribute to such enhancement. The first one is the reshaping of the DOS of the IQD originated from the formation of the IB. The DOS of the IQD is concentrated within the quantized IBs while the DOS of a QW is more evenly distributed within the corresponding conduction or valance band. Therefore, within the spectral range determined by the transition between the valance IB and the conduction IB, the total number states available in the IQD is higher than that of the QW, which allows more electrons to be excited to generate photocurrent per unit volume of the active material. The second factor is the reduced intersubband scattering with increased IQD pore diameter. The in-plane periodic pores structure in the IQD introduces modification to the wave function of the states within the IB so that the wave function overlapping between conduction IBs gets reduced. This decreases the probability of an electron to be relaxed down to lower conduction IBs, in turn, increases the number of electrons in the conduction IB that can be excited to the continuum by the secondary photons. Such an effect was validated previously in the lower temperature PL, and an IQD laser experiment where enhanced radiative recombination in the excited states through the decreased intersubband scattering was observed with an increasing IQD pore diameter [25, 26].

8.2.3 Multi-Stacked InGaAs IQD Using III-V MacEtch

As described in the previous section, the single-layer IQD IB photodetector exhibits PCD higher than that of benchmark QW. However, it is critical that the photocurrent of the IQD is smaller than the one with QW due to the active layer volume reduction. The photocurrent increased by the concentrated delta-like DOS and the longer carrier relaxation time is still much smaller than the photocurrent reduced from the volume reduction. In this section, the multi-stacked InGaAs IQD (MIQD) fabrication using the III-V MacEtch is discussed as the possible solution to further enhance the photocurrent in the conventional IQD.

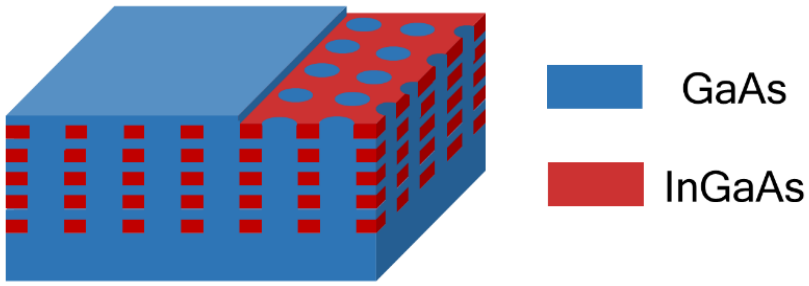

Figure 8.10: Schematic of multi-stacked MIQD.

Figure 8.10 shows the schematic of the multi-stacked InGaAs IQD. The structure consists of the stacked IQD with GaAs spacers in between. There are total of six variables that can be tuned that are composition of the InGaAs, thickness of the InGaAs, thickness of GaAs spacers, number of the IQD layers, pore diameter and pitch. The composition of the InGaAs will determine the band gap of the active region. By increasing the In composition, the band gap of the active region will be decreased. The thickness of the InGaAs will determine the energy of the excited states. The excited states energies will blue shift with decreasing thickness due to the stronger carrier confinement. The thickness of GaAs spacing will determine the interaction of the confined states between the IQD layers. As the thickness of the spacing decreases, excited states in one IQD layer

will be coupled to the ones in neighboring IQD layers, and this will allow the MIQD to exhibit the characteristics similar to the stacked QD. The number of the IQD layers will determine the total volume of the InGaAs active region. Diameter and pitch of the pores in MIQD will determine the excited state energy of the MIQD. Similar to the single-layer IQD, the stronger electron confinement will be achieved as the diameter increases with increasing pitch.

The main challenge of fabricating the MIQD structure will be the etching of the via array. By using the conventional dry etching, sidewalls of the via will become rough by ion induced damage. This will create the defects which can increase the nonradiative recombination. In addition, the sidewall scallops will produce the IQD with inconsistent diameters which may result the varied excited state energy levels, thus it will lose the advantage of coupling. The problem of the dry etching will be solved by using the III-V MacEtch. The GaAs and InGaAs MacEtch using Au mesh catalyst in an etching solution of HF, DI, and $KMnO_4$ is demonstrated in our group [40].

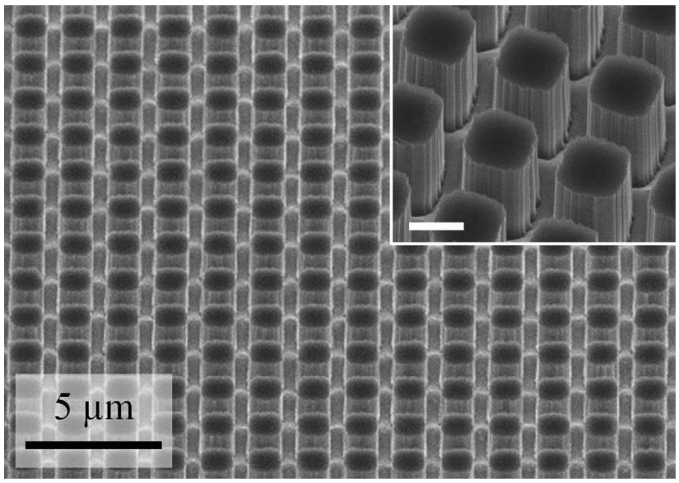

Figure 8.11: Tilted view SEM image of p-type GaAs MacEtched in 15 ml HF, 15 ml Di, and 0.025g $KMnO_4$ [40].

Figure 8.11 show the high aspect ratio GaAs micro pillars MacEtched in 15 ml HF, 15 ml DI, and 0.025 g $KMnO_4$. The detailed study of vertical etch rate in intrinsic, p-type and n-type

substrates as a function of temperature, HF to DI dilution ratio and $KMnO_4$ content are also reported.

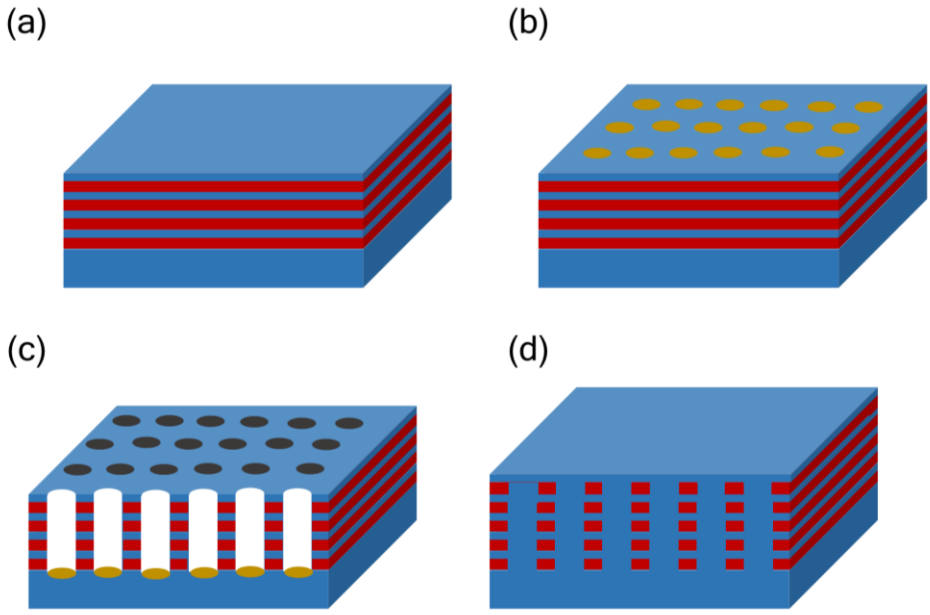

Figures 8.12: Schematics of MIQD fabrication process using III-V MacEtch.

Figure 8.12 shows the schematics of MIQD fabrication process using III-V MacEtch. First, the multi-QW layers are grown on the GaAs (100) substrate using MOCVD as shown in Figure 8.12 (a). It is important to note that the composition of the QWs, thickness of QWs, thickness of GaAs spacers and number of the QW need to be precisely controlled to prevent the QD formation by strain relaxation. The grown multi-QW layer is then characterized by XRD to determine the precise value of the composition of the InGaAs, and thickness of InGaAs and GaAs.

Figure 8.13 shows the simulated and measured XRD rocking curve of five layers of 3 nm $In_{0.13}Ga_{0.87}As$ QWs with 5 nm GaAs spacers. Next, the dot array pattern is exposed using e-beam lithography and the dot catalyst array is defined by Au film deposition and PMMA lift off as shown in Figure 8.12 (b).

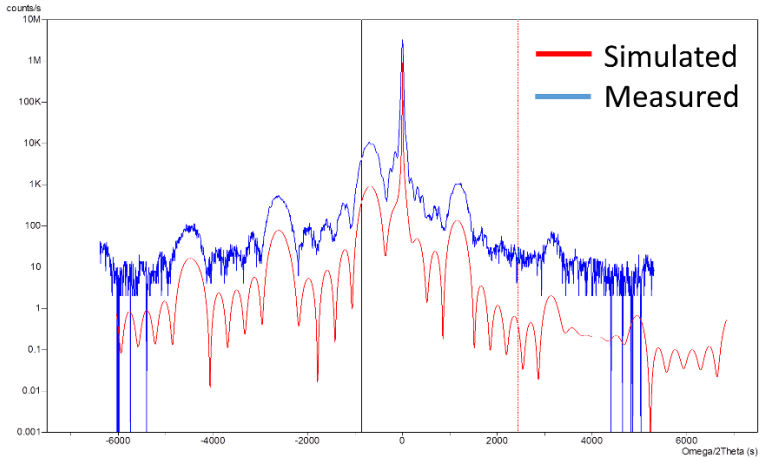

Figure 8.13: Simulated and measured XRD rocking curve of the 5x 3 nm $In_{0.13}Ga_{0.87}As$ and 7 nm GaAs spacers.

The catalyst array is then MacEtched in HF, Di, KMnO4 mixture to form the via array as shown in Figure 8.12 (c). The catalysts are then etched and the GaAs is regrown using MOCVD as shown in Figure 8.12 (d). The fabricated MIQD structure with varied parameters will be characterized by PL to measure emission wavelength, and by time resolved PL to measure the carrier lifetime. After the material characterization, MIQD intermediate band gap photodectector will be fabricated. The photocurrent of the MIQD with varied parameters will be characterized and compared with the one with QW and single IQD.

8.3 Graphene-Assisted Chemical Etching of GaAs Substrate

The graphene assisted Chemical Etching of Si substrate was previously reported by J. Kim et al. [21] in 2015. They fabricated the Si nanopillar array with 50 nm diameter and aspect ratio of 6:1 using the mesh patterned graphene by etching the sample in solution mixture of HF and H_2O_2 at temperature between 40 to 50 °C. This work showed that the graphene can be used as the MacEtch catalyst due to its high conductivity. In this section, the idea of using the graphene as the catalyst of the GaAs substrate is presented.

The monolayer graphene was transferred on the GaAs substrate. Then, PMMA was spin-coated at 2500 RPM for 60 s. Next, the discrete dot array of 500 nm diameter and 1 μm pitch was exposed using the e-beam lithography and developed with 1:3 MIBK:IPA for 2 min. The graphene on the exposed pattern was etched using the O_2 RIE. After the graphene mesh patterning, the remaining PMMA layer was dissolved in the PG-remover at 80 °C for 3 hours. The sample was MacEtched in the solution mixture of 10 ml HF, 10 ml DI and 0.2g $KMnO_4$ for 5 min.

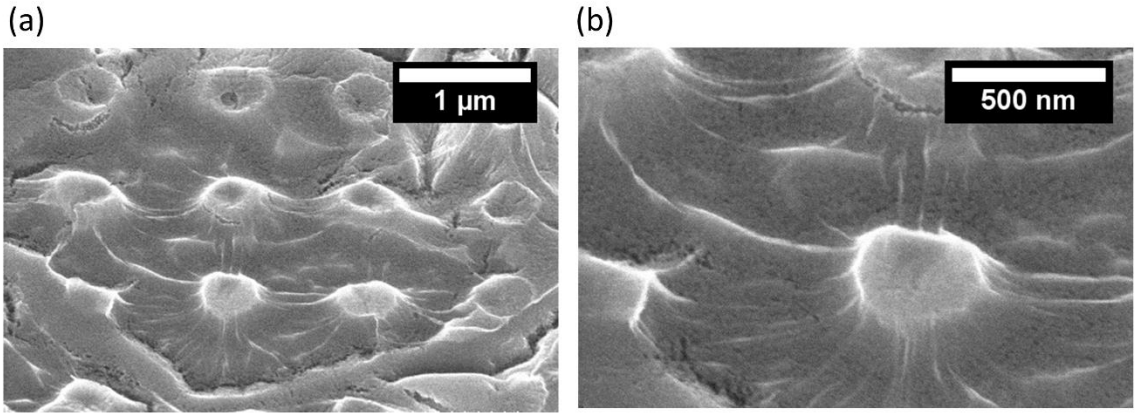

Figure 8.14: The (a) low- and (b) high-magnification 45 degree tilted SEM images of the mesh patterned graphene on GaAs substrate that was MacEtched in 10 ml HF, 10 ml DI, and 0.2g $KMnO_4$ for 5 min.

Figure 8.14 (a) and (b) show the 45 degree tilted cross-sectional SEM images of MacEtched GaAs substrate with graphene mesh catalyst. The edge of the graphene mesh shows the evidence of forward MacEtch. The GaAs under the graphene is etched to produce the tapered pillar-like structures. However, the etching uniformity across the sample is poor. This can be explained by non-uniform etch rate of GaAs under the graphene originated from (i) the grains and grain boundaries of graphene, (ii) Cu residue defects during the wet transfer process, and (iii) limited MT from the strong adhesion between graphene and GaAs substrate. The uniform etching could

be achieved if the crystalline graphene can be directly grown on GaAs substrate. The further etching study is need to enhance the etch rate and etching uniformity across the GaAs substrate.

REFERENCES

[1] X. Li, “Metal-assisted chemical etching for high aspect ratio nanostructures: A review of characteristics and applications in photovoltaics,” *Curr. Opin. Solid State Mater. Sci.*, vol. 16, no. 2, pp. 71–81, Apr. 2012.

[2] Z. Huang, N. Geyer, P. Werner, J. de Boor, and U. Gösele, “Metal-assisted chemical etching of silicon: A review,” *Adv. Mater.*, vol. 23, pp. 285–308, Sep. 2011.

[3] H. Hu, P. K. Mohseni, L. Pan, X. Li, S. Somnath, J. R. Felts, M. A. Shannon, and W. P. King, “Fabrication of arbitrarily shaped silicon and silicon oxide nanostructures using tip-based nanofabrication,” *J. Vac. Sci. Technol. B Microelectron. Nanom. Struct.*, vol. 31, no. 6, p. 06FJ01, 2013.

[4] K. Balasundaram, P. K. Mohseni, Y.-C. Shuai, D. Zhao, W. Zhou, and X. Li, "Photonic crystal membrane reflectors by magnetic field-guided metal-assisted chemical etching," *Appl. Phys. Lett.*, vol. 103, p. 214103, 2013.

[5] X. Li and P. W. Bohn, “Metal-assisted chemical etching in HF/H2O2 produces porous silicon,” *Appl. Phys. Lett.*, vol. 77, no. 16, pp. 2572–2574, 2000.

[6] S. Chattopadhyay, X. Li, and P. W. Bohn, "In-plane control of morphology and tunable photoluminescence in porous silicon produced by metal-assisted electroless chemical etching," *J. Appl. Phys.*, vol. 91, pp. 6134-6140, 2002.

[7] K. Peng, Y. Yan, S. Gao, and J. Zhu, "Dendrite-assisted growth of silicon nanowires in electroless metal deposition," *Adv. Funct. Mater.*, vol. 13, pp. 127-132, 2003.

[8] K. Peng, H. Fang, J. Hu, Y. Wu, J. Zhu, Y. Yan, *et al.*, "Metal-particle-induced, highly localized site-specific etching of Si and formation of single-crystalline Si nanowires in aqueous fluoride solution," *Chem. Eur. J.*, vol. 12, pp. 7942-7947, 2006.

[9] C. Chartier, S. Bastide, and C. Lévy-Clément, "Metal-assisted chemical etching of silicon in $HF–H_2O_2$," *Electrochim. Acta.*, vol. 53, pp. 5509-5516, July, 2008.

[10] X. H. Xia, C. M. A. Ashruf, P. J. French, and J. J. Kelly, "Galvanic cell formation in silicon/metal contacts: The effect on silicon surface morphology," *Chem. Mater.*, vol. 12, pp. 1671-1678, June, 2000.

[11] P. Lianto, S. Yu, J. Wu, C. V. Thompson, and W. K. Choi, "Vertical etching with isolated catalysts in metal-assisted chemical etching of silicon," *Nanoscale*, vol. 4, pp. 7532-7539, 2012.

[12] N. Geyer, B. Fuhrmann, Z. Huang, J. de Boor, H. S. Leipner, and P. Werner, "Model for the mass transport during metal-assisted chemical etching with contiguous metal films as catalysts," *J. Phys. Chem. C.*, vol. 116, pp. 13446-13451, June, 2012.

[13] A. I. Hochbaum, R. Chen, R. D. Delgado, W. Liang, E. C. Garnett, M. Najarian, *et al.*, "Enhanced thermoelectric performance of rough silicon nanowires," *Nature*, vol. 451, pp. 163-167, 2008.

[14] K. Q. Peng, J. J. Hu, Y. J. Yan, Y. Wu, H. Fang, Y. Xu, *et al.*, "Fabrication of single-crystalline silicon nanowires by scratching a silicon surface with catalytic metal particles," *Adv. Functi. Mater.*, vol. 16, pp. 387-394, 2006.

[15] W. Jevasuwan, K. Nakajima, Y. Sugimoto, and N. Fukata, "Metal-catalyzed electroless etching and nanoimprinting silicon nanowire-based solar cells: Silicon nanowire defect reduction and efficiency enhancement by two-step H 2 annealing," *Jpn. J. Appl. Phys.*, vol. 55, p. 065001, 2016.

[16] H. Hu, P. K. Mohseni, L. Pan, X. Li, S. Somnath, J. R. Felts, *et al.*, "Fabrication of arbitrarily shaped silicon and silicon oxide nanostructures using tip-based nanofabrication," *J. Vac. Sci. Technol. B*, vol. 31, p. 06FJ01, 2013.

[17] X. Zhang, J. K. Lin, S. Wickramanayaka, S. Zhang, R. Weerasekera, R. Dutta, *et al.*, "Heterogeneous 2.5D integration on through silicon interposer," *Appl. Phys. Rev.*, vol. 2, p. 021308, 2015.

[18] K. Balasundaram, J. S. Sadhu, J. C. Shin, B. Azeredo, D. Chanda, M. Malik, *et al.*, "Porosity control in metal-assisted chemical etching of degenerately doped silicon nanowires," *Nanotechnology*, vol. 23, p. 305304, 2012.

[19] H. Asoh, F. Arai, and S. Ono, "Effect of noble metal catalyst species on the morphology of macroporous silicon formed by metal-assisted chemical etching," *Electrochim. Acta*, vol. 54, pp. 5142-5148, 2009.

[20] J.-P. Lee, S. Choi, and S. Park, "Extremely superhydrophobic surfaces with micro- and nanostructures fabricated by copper catalytic etching," *Langmuir*, vol. 27, pp. 809-814, 2011.

[21] J. Kim, D. H. Lee, J. H. Kim, and S.-H. Choi, "Graphene-assisted chemical etching of silicon using anodic aluminum oxides as patterning templates," *ACS Appl. Mater. Interfaces*, vol. 7, pp. 24242-24246, 2015.

[22] D. Huigao, Z. Jianguo, Z. Yongzhe, X. Erqing, and H. Li, "Preparing patterned carbonaceous nanostructures directly by overexposure of PMMA using electron-beam lithography," *Nanotechnology*, vol. 20, p. 135306, 2009.

[23] W. Chern, K. Hsu, I. S. Chun, B. P. d. Azeredo, N. Ahmed, K.-H. Kim, *et al.*, "Nonlithographic patterning and metal-assisted chemical etching for manufacturing of tunable light-emitting silicon nanowire arrays," *Nano Lett.*, vol. 10, pp. 1582-1588, 2010.

[24] S.-W. Chang, V. P. Chuang, S. T. Boles, and C. V. Thompson, "Metal-catalyzed etching of vertically aligned polysilicon and amorphous silicon nanowire arrays by etching direction confinement," *Adv. Funct. Mater.,* vol. 20, pp. 4364-4370, 2010.

[25] I. Suni, M. Mäenpää, M. A. Nicolet, and M. Luomajärvi, "Thermal stability of hafnium and titanium nitride diffusion barriers in multilayer contacts to silicon," *Journal of The Electrochemical Society,* vol. 130, pp. 1215-1218, 1983.

[26] A. Sherman, "Growth and properties of LPCVD titanium nitride as a diffusion barrier for silicon device technology," *J. Electrochem. Soc.,* vol. 137, pp. 1892-1897, 1990.

[27] I. Suni, M. Blomberg, and J. Saarilahti, "Performance of titanium nitride diffusion barriers in aluminum–titanium metallization schemes for integrated circuits," *J. Vac. Sci. Technol. A,* vol. 3, pp. 2233-2236, 1985.

[28] C. Y. Ting, "TiN formed by evaporation as a diffusion barrier between Al and Si," *J. Vac. Sci. Technol.,* vol. 21, pp. 14-18, 1982.

[29] N. Kumar, J. T. McGinn, K. Pourrezaei, B. Lee, and E. C. Douglas, "Transmission electron microscopy studies of brown and golden titanium nitride thin films as diffusion barriers in very large scale integrated circuits," *J. Vac. Sci. Technol. A,* vol. 6, pp. 1602-1608, 1988.

[30] P. Walker and W. H. Tarn, *CRC Handbook of Metal Etchants*. CRC Press, 1990.

[31] L. P. B. Lima, J. A. Diniz, I. Doi, and J. Godoy Fo, "Titanium nitride as electrode for MOS technology and Schottky diode: Alternative extraction method of titanium nitride work function," *Microelectron. Eng.,* vol. 92, pp. 86-90, 2012.

[32] S. S. Ang, "Titanium nitride films with high oxygen concentration," *J. Electron. Mater.,* vol. 17, pp. 95-100, 1988.

[33] S. H. Kim, P. K. Mohseni, Y. Song, T. Ishihara, and X. Li, "Inverse metal-assisted chemical etching produces smooth high aspect ratio InP nanostructures," *Nano Lett.,* vol. 15, pp. 641-648, 2015.

[34] O. J. Hildreth and D. R. Schmidt, "Vapor phase metal-assisted chemical etching of silicon," *Adv. Funct. Mater.,* vol. 24, pp. 3827-3833, 2014.

[35] E. L. Cussler, *Diffusion: Mass Transfer in Fluid Systems*. Cambridge University Press, 2009.

[36] K.A. Dill and S. Bromberg, *Molecular Driving Forces: Statistical Thermodynamics in Chemistry and Biology, Macromolecular Chemistry and Physics*. Garland Science, 2002.

[37] C. Q. Lai, H. Cheng, W. K. Choi, and C. V. Thompson, "Mechanics of catalyst motion during metal assisted chemical etching of silicon," *J. Phys. Chem. C.*, vol. 117, pp. 20802-20809, 2013.

[38] F. Yamato, F. Hiroyuki, and T. Hiroshi, "Vapor hydrofluoric acid sacrificial release technique for micro electro mechanical systems using labware," *Jpn. J. Appl. Phys.*, vol. 42, p. 3690, 2003.

[39] M. DeJarld, J. C. Shin, W. Chern, D. Chanda, K. Balasundaram, J. A. Rogers, *et al.*, "Formation of high aspect ratio gaAs nanostructures with metal-assisted chemical etching," *Nano Lett.*, vol. 11, pp. 5259-5263, 2011.

[40] P. K. Mohseni, S. H. Kim, X. Zhao, K. Balasundaram, J. D. Kim, L. Pan, *et al.*, "GaAs pillar array-based light emitting diodes fabricated by metal-assisted chemical etching," *J. Appl. Phys.*, vol. 114, p. 064909, 2013.

[41] J. Kim and J. Oh, "Formation of GaP nanocones and micro-mesas by metal-assisted chemical etching," *Phys. Chem. Chem. Phys.*, vol. 18, pp. 3402-3408, 2016.

[42] V. B. Verma and J. J. Coleman, "A parametric analysis of the density of states and intraband energy gaps in an ordered nanopore array diode laser," *J. Appl. Phys.*, vol. 105, p. 043106, 2009.

[43] N. L. Dias, A. Garg, U. Reddy, J. D. Young, K. P. Bassett, X. Li, *et al.*, "Experimental verification of reduced intersubband scattering in ordered nanopore lattices," *Appl. Phys. Lett.*, vol. 98, p. 071109, 2011.

[44] A. Martí, E. Antolín, C. R. Stanley, C. D. Farmer, N. López, P. Díaz, *et al.*, "Production of photocurrent due to intermediate-to-conduction-band transitions: A demonstration of a key operating principle of the intermediate-band solar cell," *Phys. Rev. Lett.*, vol. 97, p. 247701, 2006.

APPENDIX A. EMPIRICAL VERTICAL ETCH RATE MODEL CODE

```
clear all;
close all;

%Pattern dimension
Dnm=100:100:900; %diameter in nm
Pnm=1000; %pitch in nm
D=Dnm.*0.001; %diameter in um
P=Pnm.*0.001; %pitch in um
S=(P-D); %spacing

%Solution condition
H2O2=0.13; %H2O2 in molar concentration
HF=0.56; %HF in molar concentration
% low=H2O2/(HF+H2O2)= H2O2 molar concentration ratio
low=0.065;

%parameters defined from the experimental data
a = -30.00356+451.66062*low-397.48018*low^2;
b = -86.55844+1099.10749*low-386.55952*low^2;
Z=(low-0.4105)/0.06787;
c=320.72127+97.97012*exp(-exp(-Z)-Z+1);

%vertical etch rate
Etch_Rate = b.*S-c.*S.^2+a;

%Etch rate < 0 is not valid
Etch_Rate(Etch_Rate <0) = 0;

%plots the Etch rate vs Diameter
plot(Etch_Rate, Dnm);
```